Cooling and exhumation in the footwall of the Dangardzong fault, Thakkhola graben, west central Nepal

by

Alex Brubacher

B.Sc. Hons., Memorial University of Newfoundland, 2016

A THESIS SUBMITTED IN PARTIAL FULFILLMENT OF
THE REQUIREMENTS FOR THE DEGREE OF

MASTER OF SCIENCE

in

The College of Graduate Studies

(Earth and Environmental Sciences)

THE UNIVERSITY OF BRITISH COLUMBIA

(Okanagan)

April 2018

The following individuals certify that they have read, and recommend to the College of Graduate Studies for acceptance, a thesis/dissertation entitled:

Cooling and exhumation in the footwall of the Dangardzong fault, Thakkhola graben, west central Nepal

submitted by Alex Brubacher in partial fulfilment of the requirements of the degree of Master of Science

Dr. Kyle Larson, I. K. Barber School of Arts & Sciences

Supervisor

Dr. John Greenough, I.K. Barber School of Arts & Sciences

Supervisory Committee Member

Dr. Yuan Chen, I.K. Barber School of Arts & Sciences

Supervisory Committee Member

Dr. Lori Kennedy, Faculty of Science, UBC Vancouver

University Examiner

Abstract

Late-stage E-W orogen-parallel extension is well documented in the Tibetan plateau, however, the nature and timing of extension related features remains unclear. In order to investigate the temporal development of the graben that accommodate this extension, $^{40}Ar/^{39}Ar$ and U-Th/He thermochronology were used to characterise the evolution of the Thakkhola graben in west-central Nepal, a major N-S striking, E-W extensional structure that cuts across the High Himalaya. The Mugu and Mustang granites occur in the footwall of the Dangardzong fault, which defines the western boundary of the graben. Monazite U-Th/Pb geochronology is used to constrain the minimum crystallization age of these granites to ∼22-20 Ma. $^{40}Ar/^{39}Ar$ geochronology of micas date the cooling of the granites through calculated Ar migration closure temperatures (580-344 °C) to ∼17 Ma. Zircon and apatite U-Th/He dating yield ages of ∼15-9 Ma and ∼12-4 Ma, respectively, corresponding to cooling of the granites through respective He migration closure temperatures of ∼220-140 °C and ∼116-44 °C. Microstructures in rocks collected in this region show that E-W extensional structures were contemporaneous with cooling through muscovite closure to Ar migration at ∼17 Ma, providing a minimum age of initiation of extension. Detailed low-temperature cooling paths, based on U-Th/He data extracted from the undeformed intrusive bodies, record inflections in cooling rates at ∼13-8 Ma and at ∼5 Ma. These two inflections mark deceleration of cooling in the footwall, which is interpreted to reflect a reduction in the spreading rate of the graben. The slowdowns are coeval with increased graben development across the Tibetan plateau and as such are interpreted to reflect strain being partitioned into these newly generated structures. This study adds to a growing body of evidence for a major kinematic shift in the Himalaya occurring around ∼13 Ma potentially linked with the flow of material eastward out of the Tibetan plateau.

Lay Summary

The Himalayan mountain chain is developing because of N-S convergence between India and Asia. Interestingly, the Tibetan plateau is characterized by graben that accomodate active E-W extension. The timing of mountain chain-parallel extension in an actively converging region is a key aspect of understanding the development of such features. The Thakkhola graben in Nepal, which is the result of E-W extension, is determined to have been active by ca. 17 Ma, based on microstructural analysis and radiometric dating carried out in this study. Furthermore, multiple different radiometric ages from the same rock in the Thakkhola graben define a major reduction in the rate of cooling at around 8-13 million years ago. This change in cooling rate is contemporaneous with the initiation of movement on several other E-W extensional structures in southern Tibet and a major shift in how the Himalayan system is evolving.

Table of Contents

List of Tables

List of Figures

Acknowledgements

I would like to thank my supervisor, Dr. Kyle Larson, first and foremost, for providing support and guidance through every stage of this project, from booking the flights to crossing the 'I's and dotting the 'T's. Dr. Larson has pushed me to work hard at becoming a better and more inquisitive geologist and scholar, while providing thoughtful insight and feedback when needed. I am also thankful for the support of the rest of my supervisory committee, Dr. John Greenough and Dr. Yuan Chen. I am indebted to Dr. William Matthews, Dr. Alfredo Camacho, and Dr. John Cottle, along with their laboratory assistants, who have helped me understand the laboratory methods used and made sure I obtained meaningful data. I am grateful for the field preparation and guidance of Pradap and Teke Tamang, and for Pasang, Kailash, Balbadur, and Nima Tamang for field logistics. I am also thankful for the field assistance of Iva Lihter, and the guidance and advice of rest of the Himalayan tectonics group at UBCO; Sudip, Mathieu, and Kumar. I am also extremely grateful for my family and friends, who have supported me through these 5.5 years of university, and who have been very understanding when I never reach for the bill. This project was funded, in part, by an NSERC Discovery grant awarded to Dr. Kyle larson, and by an NSERC Canada Graduate Scholarships-Masters grant, Graduate Entrance Scholarship, and University Graduate Fellowship awarded to myself.

Chapter 1

Introduction

The Himalayan mountain chain spans for ∼2500 km, crossing the borders of Pakistan, India, Nepal, China, and Bhutan (Fig. 1.1). It is one of the few currently active continental collision zones, and this, combined with its broad extent and excellent exposure, has resulted in it becoming the type locality of continental collisional boundaries (Hodges, 2000; Yin, 2006). Geologists have been studying the Himalaya since as early as the mid-19th century (Upreti, 1999) and despite political and topographic obstacles (Hodges, 2000), have continued to do so for more than a century as they seek to understand the inner workings of large, hot orogens.

1.1 Overview of the Himalaya

The Himalaya began to form ∼55 Myr ago with the collision of the Indian and Eurasian continents (DeCelles et al., 2001; Mascle et al., 2012; Rowley, 1996). Sediments deposited on the northern passive margin of the Indian plate were scraped off of the downgoing plate, deformed and metamorphosed, and are now exposed in the Himalaya (Bollinger et al., 2004; Cottle et al., 2015; DeCelles et al., 2001; Mascle et al., 2012; Myrow et al., 2003). Four major lithotectonic zones are recognized within the Himalayan belt, separated or bound by five major structural divisions (Fig. 1.2; Cottle et al., 2015; Le Fort, 1975), all of which are remarkably continuous along the length of the range (Kohn, 2014; Montomoli et al., 2013; Wu et al., 1998; Yin, 2006).

The Main Frontal thrust (MFT) is the youngest and southernmost of the major N-dipping structures in the Himalaya. It separates the Terai (lowlands) in its footwall from the Siwaliks (foothills) in its hanging wall (Hodges, 2000; Mascle et al., 2012; Yin, 2006). The Siwaliks (or Subhimalaya) is the southernmost lithotectonic zone within the Himalaya (Cottle et al., 2015; Hodges, 2000), consisting of Neogene to Quaternary unmetamorphosed molasse deposits, deformed into a south-verging fold and thrust belt (Cottle et al., 2015; Mascle et al., 2012; Hodges, 2000). The thickness of the unit varies from ∼2 km in the south to ∼10 km in the north (Hodges, 2000).

The Main Boundary thrust (MBT) separates the Siwaliks from the overthrust Lesser Himalayan sequence (LHS; Fig. 1.2; Mascle et al., 2012). The LHS consists of 8-10 km of phyllite, impure quartzite, marble, metabasalt, and orthogneiss, metamorphosed at lower greenschist to (locally) lower amphibolite facies (Hodges, 2000; Montomoli et al., 2013). The LHS can be further divided into upper and lower units, separated by a major unconformity (Hodges, 2000;

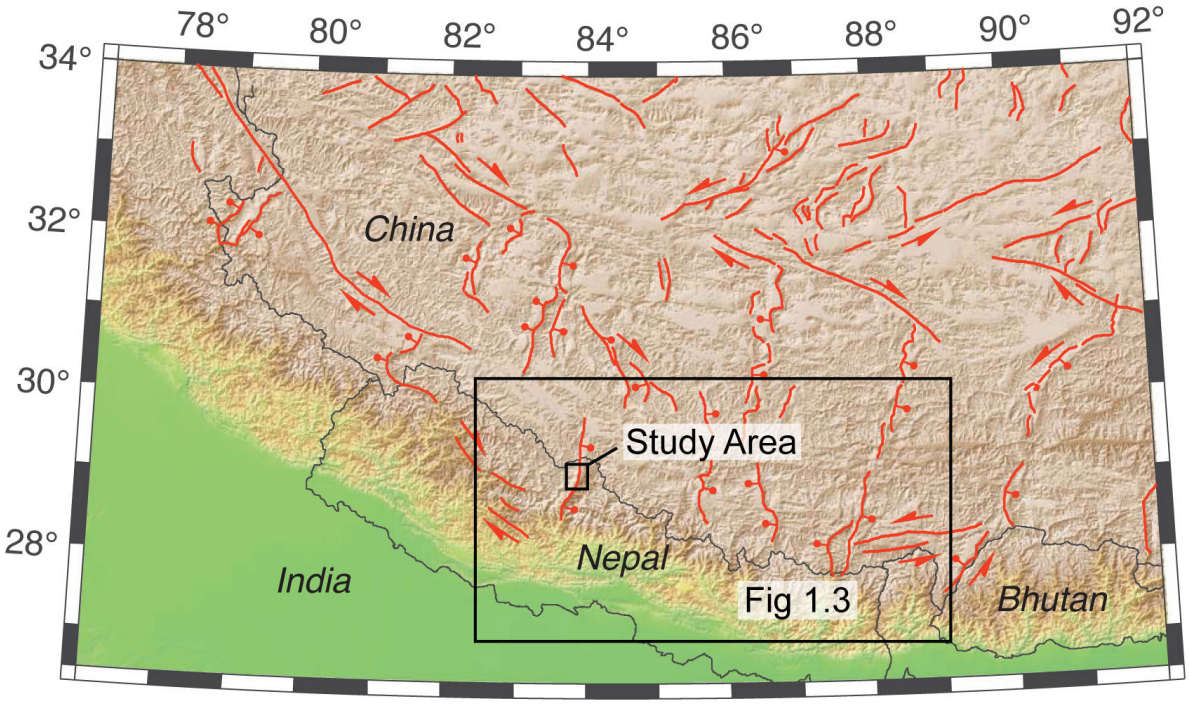

Figure 1.1: Map of south Asia, showing Himalayan topography and currently active E-W extension-related N-S trending normal faults, and associated strike-slip faults, from Styron et al. (2011). The location of the study area and figure 1.3 shown in black boxes.

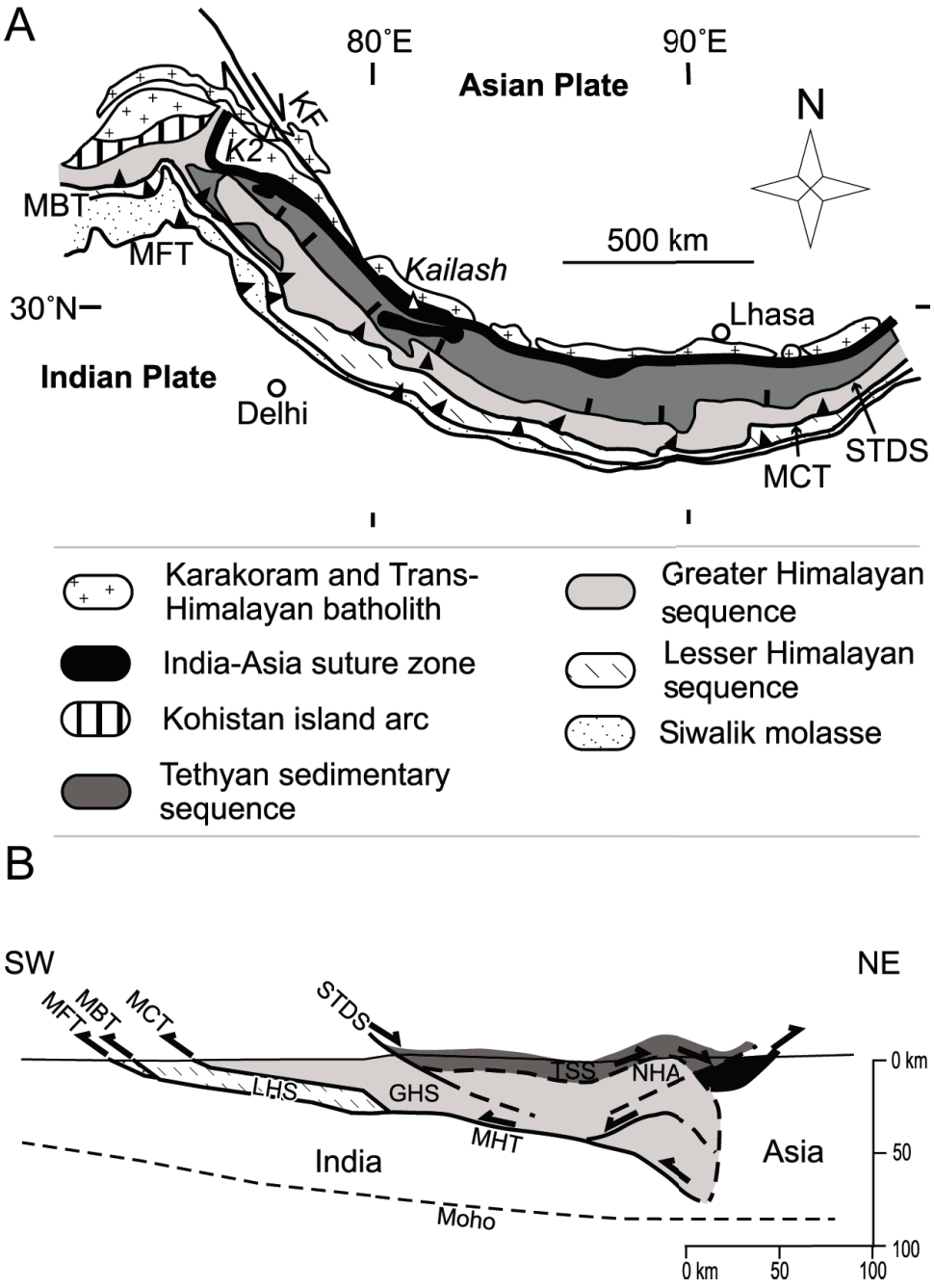

Figure 1.2: Major lithology and structures of the Himalaya, modified after Larson et al. (2010) and Hauck et al. (1998). A) Simplified geological map showing major lithotectonic units and faults. B) Simplified cross section of the Himalaya, indicating location of major faults at depth.

Upreti, 1999). The Lower LHS is Mesoproterozoic in age, while Upper LHS is Cambrian in age and locally unconformably overlain by Carboniferous-Permian strata (Hodges, 2000). The upper boundary of the LHS is marked by the Main Central thrust zone (MCT).

The MCT is a north dipping, thrust-sense ductile shear zone that, like the other major faults previously mentioned, can be mapped across the entire range (Fig. 1.2; Montomoli et al., 2013; Searle et al., 2008; Yin, 2006). There has been much controversy over how the structures is mapped in recent years (see Searle et al., 2008; Martin, 2017). Searle et al. (2008) defines the MCT as "the base of the large-scale zone of high strain and ductile deformation, commonly coinciding with the base of the zone of inverted metamorphic isograds, which places Tertiary metamorphic rocks of the Greater Himalayan sequence over unmetamorphosed or low-grade rocks of the Lesser Himalaya." (p. 532). This definition accounts for along-strike variations in the exact location of metamorphic gradients and lithological differences, which have been the foci of debate in the past (see Searle et al., 2008; Martin, 2017, for full discussion).

The Main Frontal thrust, Main Boundary thrust, and Main Central thrust are all believed to sole onto a N-dipping decollement surface beneath the Himalaya, commonly called the Main Himalayan thrust (MHT; Fig. 1.2; Mascle et al., 2012; Yin, 2006). Various geophysical surveys have identified the MHT at depth, which is believed to defined the location of the underthrusting Indian plate (Bollinger et al., 2004). Seismic data showing recent earthquake foci along this thrust suggest that the MHT is currently accommodating convergence (Bollinger et al., 2004).

The Greater Himalayan Sequence (GHS; Fig. 1.2) - also called the High Himalaya Crystallines, Higher Himalayan gneisses, Central Crystallines, or the Tibetan Slab - (Cottle et al., 2015; Hodges, 2000) lies structurally above the LHS and consists mainly of high-grade mica schist, paragneiss, calc-silicate, and migmatite (Hodges, 2000; Montomoli et al., 2013; Yin, 2006). Once believed to have represented the crystalline basement to the overlying Tethyan Sedimentary Sequence (TSS; Le Fort, 1975), more recent studies have shown that the GHS has a sedimentary protolith, and likely represents units deposited in the Indian passive margin stratigraphically above those that formed the LHS (Hodges, 2000; Searle et al., 2006). The GHS ranges in age from Neoproterozoic to Ordovician (DeCelles et al., 2001; Yin, 2006) and in thickness along strike from as little as 2 km in western Nepal, up to 50 km in NW India and Bhutan, with an average thickness of 20-30 km (Montomoli et al., 2013, 2015). Numerous large leucogranite plutons occur within the uppermost GHS, which are believed to be derived from partial melting of the GHS itself (Hodges, 2000; Searle et al., 2006; Wu et al., 1998).

The top of the GHS is marked by a network of low-angle normal-sense faults, called the South Tibetan detachment system (STDS; Fig. 1.2; Hodges, 2000; Kohn, 2014; Mascle et al., 2012; Yin, 2006). This boundary, which separates the unmetamorphosed to low-grade TSS above from the high metamorphic grade GHS below, often occurs at the crest of the Himalaya, such that many of the great peaks (e.g. Everest, Dhaulagiri, Cho Oyu) actually contain the structure. It has been suggested that the STDS may either sole onto the MHT at depth, or that

it shallows to the north, merging with the Great Counter thrust (Fig. 1.2; Burchfiel and Royden, 1985; Kohn, 2014; Yin, 2006). Movement on the STDS initiated in the Miocene (Hodges, 2000) and is widely viewed to be at least broadly contemporaneous with that on the MCT (Beaumont et al., 2004; Godin et al., 2001, 2006; Hodges et al., 1992; Jamieson et al., 2004; Kellett and Grujic, 2012; Vannay and Hodges, 1996).

The structurally highest lithotectonic zone in the Himalaya is the TSS (Fig. 1.2) - also known as the Tibetan Sedimentary Sequence, or Tethys Himalaya - (Hodges, 2000). It consists of largely unmetamorphosed clastic and carbonate sedimentary rocks that locally reach lower amphibolite facies (Hurtado, 2002; Montomoli et al., 2013; Yin, 2006). The protolith to this zone is often considered to be laterally equivalent to the GHS (Searle et al., 2006). Ages in the TSS range from Proterozoic to Eocene (Yin, 2006; Liu and Einsele, 1994), and based on detrital zircon and Nd isotope data, Searle et al. (2006, 2008) suggest that the entire LHS-GHS-TSS sequence corresponds to a semi-continuous series of sediments deposited on the northern passive margin of India prior to collision.

The E-W trending north Himalayan anticline crops out in structural windows through the TSS in southern Tibet and northern Nepal (Fig. 1.3). It is marked by a series of structural culminations cored by leucogranite and/or high-grade metamorphic rock of GHS affinity, typically surrounded by low grade metasediments (Hodges, 2000; Lee et al., 2000, 2006; Larson et al., 2010).

The Indus-Tsangpo suture zone (ITSZ; Figs. 1.2 and 1.3; also called India-Asia, Indus-Yarlung, or Yarlung-Tsangpo suture zone) marks the boundary between the Indian and Eurasian plates and is the northern boundary of the Himalaya (Hodges, 2000; Mascle et al., 2012). The suture zone is marked by flysch deposits and ophiolites related to the closure of the Tethys Ocean (Hodges, 2000; Montomoli et al., 2013).

1.2 Geological Setting

1.2.1 Thakkhola graben

The Tibetan Plateau is a high, mostly flat plateau with an average elevation of ∼5000 m (Hodges, 2000; Mascle et al., 2012). Relief within the plateau is dominated by late Miocene to Pliocene graben that accommodate E-W extension in the plateau (Fig. 1.1; e.g. Ratschbacher et al., 2011; Yin et al., 1999). The E-W extension generating these structures is thought to reflect a shift from S-directed to orogen parallel crustal movement, which has been documented not only in the upper crust, but also in the midcrust (Cottle et al., 2009), and in the lower crust (Clark and Royden, 2000). This shift in orogen-wide kinematics may be driven by a change in convergence rate and direction between India and Asia (e.g. Molnar and Stock, 2009). Some of these structures extend southward across the crest of the Himalaya, incising deep valleys and forming sedimentary basins. The Thakkhola graben, in the Mustang region of west-central

Nepal, is one such structure and is the focus of this study.

The present day geomorphology of the Mustang region is dominated by the Kali Gandaki river valley, which is one of the deepest valleys in the world, incised to an elevation of ∼2500 m between the peaks of Dhaulagiri (8167 m) in the west and Annapurna (8091 m) in the east. The upper reaches of the river run through the Thakkhola graben. The Thakkhola graben extends southward almost to the STDS (Fig. 1.3), while the northern edge of the graben, which is poorly defined in most geological maps, ends south of the Indus-Tsangpo suture zone (Hurtado et al., 2001; Hurtado, 2002). The eastern boundary of the graben is defined by a series of unnamed, steeply west-dipping normal faults, while the west side is defined by the N-NE striking, steeply east-dipping Dangardzong normal fault. It is believed to be the main graben-forming structure (Fig. 1.3; Colchen, 1999; Fort et al., 1982; Hurtado et al., 2001). Total E-W extension accommodated within the graben is estimated to be ∼30 km (Hurtado, 2002).

As mapped, the footwall of the Dangardzong fault includes low-grade to unmetamorphosed rocks of the TSS and two granitic bodies, the (Dolpo-) Mugu batholith, a large elongate NW-SE trending body, and the smaller Mustang granite to the north (Fig. 1.3; e.g. Hurtado, 2002; Le Fort and France-Lanord, 1994). The Mugu and Mustang granites have mineralogy and textures similar to other plutons that occur near the crest of the Himalaya, which are interpreted as being derived from partial melting of a sedimentary source rock (i.e., S-type granites; Le Fort et al., 1987; Deniel et al., 1987; Searle et al., 2009). Initial age data determined by monazite ID-TIMS, date the Mugu batholith as 20.8 ± 0.7 Ma, and the Mustang granite as 23.4 ± 0.2 Ma (Hurtado, 2002). These ages overlap with those from many other Himalayan leucogranites, including the nearby Manaslu pluton (23-19 Ma; Harrison et al., 1999), the Makalu pluton, in eastern Nepal (∼24-22 Ma; Schärer, 1984), and even those at the western end of the Himalaya in Zanskar, India (22-19 Ma; Noble and Searle, 1995).

The hanging wall block of the Dangardzong fault comprises five sedimentary formations, which show evidence of syn-kinematic deposition (Garzione et al., 2003). The oldest sedimentary unit within the graben is the Tetang formation, consisting of a 150 m thick succession of silty gravel and breccia, conglomerate, sandstone, and tuffaceous sediments (Fort et al., 1982). The deposition of this lowest unit has been dated at ∼11 to ∼9.6 Ma (Garzione et al., 2003). The Thakkhola formation overlies the Tetang formation, separated from it by a slight angular unconformity, and consists of a 700 m thick succession of red conglomerate, sandstone, limestone, and clay deposits (Fort et al., 1982; Hurtado et al., 2001). The Sammargaon and Marpha formations both lie disconformably atop the Thakkhola formation, and have been dated as upper Pliocene to upper Pleistocene (Hurtado et al., 2001). The Sammargaon formation consists of unsorted angular breccia, and only occurs in the western slopes of the graben, while the Marpha formation is made up of >200 m thick glaciolactustrine sediments (Hurtado et al., 2001). The uppermost sedimentary unit in the Thakkhola graben is the Kali Gandaki formation, consisting of terraced fluviatile and lacustrine deposits, limited to the sides of the Kali Gandaki river

(Fort et al., 1982; Hurtado et al., 2001). Hurtado et al. (2001) used the chronology of terrace formation to bracket the bulk of the Kali Gandaki sedimentation to between 17.2 and 7.5 ka. A series of ∼N-S trending syn-sedimentation normal faults cross cut the graben-fill sediments, providing evidence of continued E-W extension (Colchen, 1999; Hurtado et al., 2001).

The age of the Thakkhola graben is only loosely constrained. As mentioned previously, the earliest sediments dated in the valley are ∼11 Ma (Garzione et al., 2003), which give a potential minimum age. Approximately 40 km east of the graben, hydrothermal muscovite from a N-S trending brittle fracture, which was interpreted to represent the earliest deformation related to E-W extension in the Thakkhola graben, was dated as ∼14 Ma, extending the minimum age constraint for the inception of E-W extension in the region (Coleman and Hodges, 1995).

1.2.2 This Study

The majority of studies in the Himalaya have focused on the results of N-S compression, namely the development of the High Himalaya and the southward extrusion of the Himalayan metamorphic core. However, late-stage E-W extension across the region has resulted in numerous N-S trending graben and related strike-slip structures in Tibet, some of which cut across the High Himalaya (Fig. 1.1). The mechanisms and timing behind orogen-parallel (E-W) extension in an actively N-S converging orogen are poorly understood. This study uses detailed geochronologic data to characterize the timing of opening and rate of development of the N-S trending Thakkhola graben (Fig. 1.3).

During preliminary work in the Thakkhola graben Hurtado (2002) suggested that part of its cooling history was imparted by movement on the Dangardzong fault. This project seeks to characterize the plutons exposed in the footwall of the fault using petrology, U-Th/Pb geochronology, and single-grain $^{40}Ar/^{39}Ar$ and U-Th/He thermochronology, in an attempt to: 1) isolate any potential contributions of pre-Thakkhola graben cooling/exhumation from that associated with the opening of the structure, and 2) compare the detailed cooling history of the Thakhola with data from graben investigated across Tibet. These new data will help constrain the timing and rate of cooling in the footwall of the Dangarzong fault, which when paired with regional data, can be used to elucidate the kinematic importance of similar structures across the orogen.

Fieldwork in the Upper Mustang region of west-central Nepal was conducted in October 2016. Three field locations were visited over the course of a two week trek; Ghami (GH), Ghar Gompa (GG), and Dhannga Khola (DK; Fig. 1.3). Fieldwork was originally planned to comprise up to 8 days of jeep-assisted structural mapping and specimen collection along the western edge of the graben. Due to logistical setbacks, however, the entire trek was completed on foot, and hence only allowed for specimen collection with limited structural data collected in metamorphosed TSS rocks to be used in a separate study. Ten leucogranite specimens were collected for petrographic analysis and radiometric dating by methods as outlined in the following chapter. Four geochronologic systems with different closure temperatures are used to constrain detailed

cooling paths of the specimens; U-Th/Pb in monazite, $^{40}Ar/^{39}Ar$ in muscovite and biotite, and U-Th/He in both zircon and apatite. Note that specimens are referred to throughout as per Fig. 1.3, where the initial letters represent sampling location (GH = Ghami, GG = Ghar Ghompa, DK = Dhanggna Khola). Mineral abbreviations used throughout this thesis follow Whitney and Evans (2010).

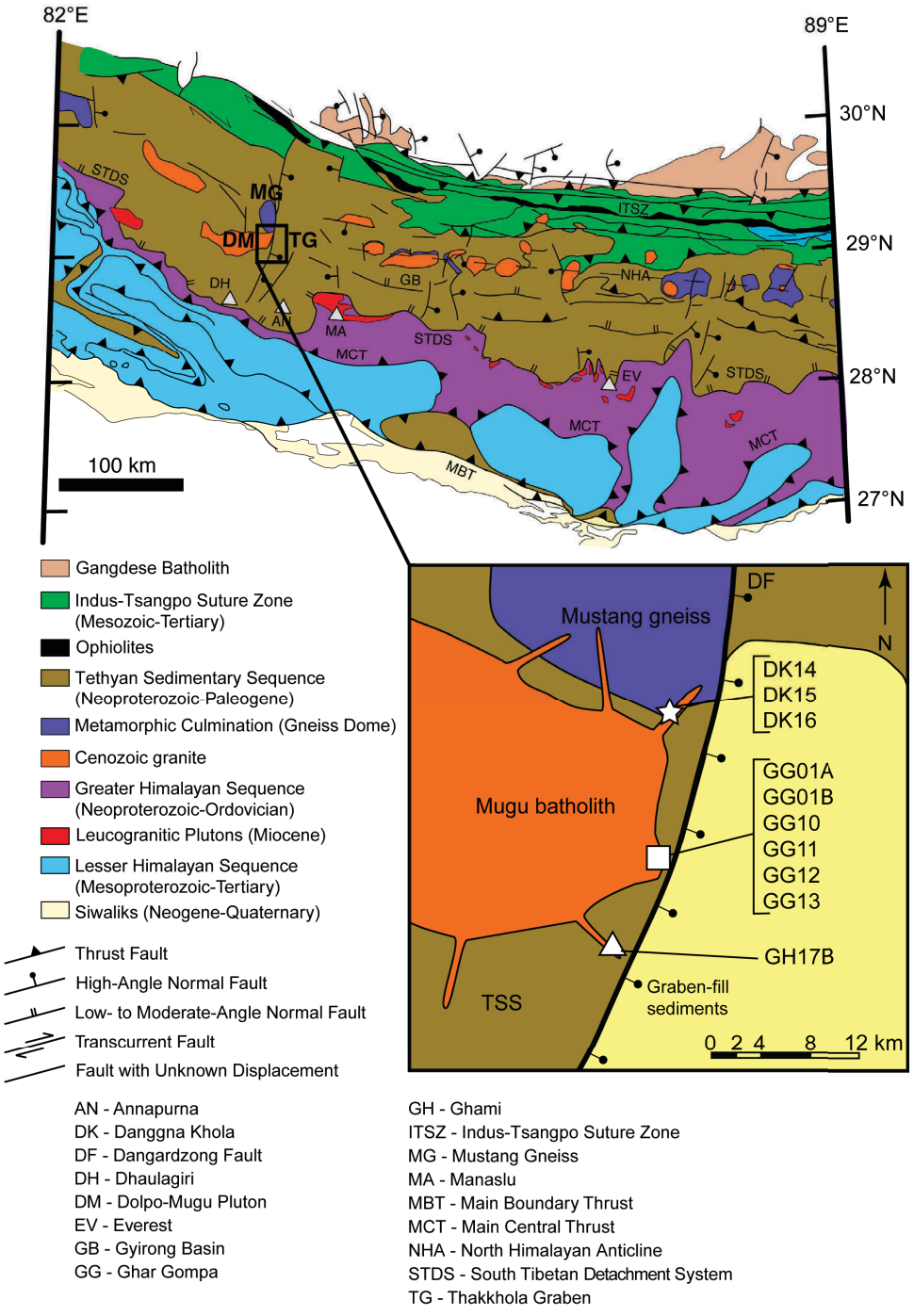

Figure 1.3: Geological map of the central Himalaya modified from Hodges (2000) and references therein. Inset: geology of the Upper Mustang region, based on Hurtado (2002), showing major lithologies and sampling locations from this study.

Chapter 2

Methods

2.1 Rock Classification

2.1.1 Petrography

Polished thin sections were cut from 7 specimens (GG01A, GG10, GG12, DK14, DK15, DK16, and GH17B; Appendix B-II) for petrographic observations and scanning electron microscope (SEM) analysis. Point-counting was conducted in each thin section under a petrographic microscope to estimate modal mineral abundances and classify the specimens under the International Union of Geological Sciences (IUGS) system for granitic rocks. Thin sections were further examined for the calculation of An% using energy dispersive spectrometry of backscattered electron images on the scanning electron microscope (SEM) in the Fipke Laboratory for Trace Element Research at the University of British Columbia, Okanagan. The remaining three specimens (GG01B, GG11, and GG13) were texturally and mineralogically similar to their neighbours in hand sample, and thus were only used for thermochronology.

2.2 Geochronology and Thermochronology

2.2.1 Geochronology overview

Geochronometers within minerals record the time when a radioactive clock began ticking. At high temperatures, which are specific to the decay system, the radioactive decay products used for dating are not retained within a mineral but instead are released to equilibrate with their surroundings (Dodson, 1973). The temperature below which all of the decay product is retained is that isotopic systems closure temperature (T_c), which varies depending on the structural and chemical properties of the mineral being dated, and more crystal-specific properties like crystal size and diffusion behaviour (e.g. Dodson, 1973; Harrison et al., 1985; Hames and Bowring, 1994; Kelley, 2002b). Since geochronometers have varying closure temperatures, they may record different thermal events. Higher temperature systems, such as the U-Th/Pb system, have closure temperatures close to or above the crystallization temperature of many igneous rocks and, therefore, are used to date the formation of igneous rocks from a cooling magma or lava (e.g. Harrison and Zeitler, 2005; Faure and Mensing, 2009). Other systems, such as the K/Ar system and its derivative, the $^{40}Ar/^{39}Ar$ system, have much lower closure temperatures

(∼300-400 °C for common micas), and will therefore record when a rock cooled below a relatively low temperature (Dodson, 1973). The practice of using this and other low-temperature geochronometers, such as fission-track dating or U-Th/He dating, is commonly referred to as thermochronology. These lower temperature systems are useful for determining cooling ages and rates, which are often interpreted with respect to timing and rate of exhumation (McDougall and Harrison, 1999).

This study employs the use of four geochronologic systems in order to develop a detailed cooling history (U-Th/Pb in Mnz, $^{40}Ar/^{39}Ar$ in Ms and Bt, U-Th/He in Ap and Zrn). These analytical methods are outlined in the following sections, including principles behind the $^{40}Ar/^{39}Ar$ and U-Th/He systems. For a review of the U-Th/Pb method see Faure and Mensing (2009) and references therein, and for a more formal review of the $^{40}Ar/^{39}Ar$ and U-Th/He methods, see McDougall and Harrison (1999), or Harrison and Zeitler (2005), respectively, and references therein.

2.2.2 U-Th/Pb Geochronology

The U-Th/Pb dating method is an intensively studied and widely used system for dating the crystallization, sedimentation, and metamorphism of rocks. Based on the radioactive decay of ^{238}U, ^{235}U, ^{234}U and ^{232}Th, it is a complex system involving several separate decay schemes (Faure and Mensing, 2009). Because the most commonly used mineral for U-Th/Pb dating, zircon, is highly resistant to weathering and is refractory during melting, often only relict/inherited grains are found in S-type granites, thus monazite (Mnz) is a better choice for dating the crystallization of such rocks (Parrish, 1990; Schärer et al., 1986). Monazite $^{208}Pb/^{232}Th$ dates are used in this study, partly due to the abundance of Th in monazite, and partly to avoid problems associated with monazite incorporating excess ^{230}Th during crystallization, leading to extraneous ^{206}Pb which would give an erroneously old $^{206}Pb/^{238}U$ age (Cottle et al., 2009; Parrish, 1990; Schärer, 1984).

The seven samples (GG01A, GG10, GG12, DK14, DK15, DK16, and GH17B) were analysed for Mnz U-Th/Pb geochronology at the University of California Santa Barbara (UCSB). Specimens were crushed and ground using standard mechanical methods, and heavy minerals separated using a Rogers Gold™ table, heavy liquids (Methyl iodide, MI, 3.35g/cm^3), and Frantz™ magnetic techniques. Separated monazite grains were mounted in epoxy, polished and analysed using laser ablation multi-collector inductively coupled plasma mass spectrometry (LA-MC-ICP-MS), which simultaneously collects U, Th, and Pb isotopic ratios. Additional procedures and instrument parameters are outlined in Appendix A-I.

2.2.3 $^{40}Ar/^{39}Ar$ Thermochronology

Principle

The $^{40}Ar/^{39}Ar$ dating method is a derivative of the K/Ar method, with the $^{40}Ar/^{39}Ar$ method quickly becoming popular after its initial description by Merrihue and Turner (1966). One main advantage of the $^{40}Ar/^{39}Ar$ over the K/Ar system is that it does not require separate measurement of K and Ar, but instead measures ^{39}Ar as a proxy for K from the same specimen being analyzed for radiogenic ^{40}Ar (McDougall and Harrison, 1999), which allows for more accurate information to be gathered from smaller samples.

The K/Ar and $^{40}Ar/^{39}Ar$ methods are based on the radioactive decay of the ^{40}K isotope. ^{40}K has an atomic abundance of 0.012% of naturally occurring K, and a half-life of 1250 Ma (McDougall and Harrison, 1999). It has a forked-decay scheme, with 89.5% of ^{40}K becoming ^{40}Ca by beta emission, and 10.4% becoming ^{40}Ar by either electron capture (10.3%) or positron emission (<1%; Gillot et al., 2006). Potassium-bearing rocks will produce ^{40}Ar, which is easily released out of the mineral at higher temperatures, but upon cooling to sufficiently low temperatures, becomes trapped within crystal lattices of K-bearing minerals (McDougall and Harrison, 1999). The amount of trapped ^{40}Ar and parent K can then be measured, and with knowledge of the decay rate and mineral-specific diffusion rates, can provide the date at which that specific mineral reached its closure temperature (Dodson, 1973; Kelley, 2002a).

In the $^{40}Ar/^{39}Ar$ method the specimen of interest is first irradiated in a nuclear reactor by fast-neutron bombardment. This changes a percentage of the ^{39}K to gaseous ^{39}Ar by the $^{39}K(n,p)^{39}Ar$ reaction, where n is the incident neutron, and p is the expelled proton (Merrihue and Turner, 1966). The amount of ^{39}Ar formed during this process depends on the neutron flux in the reactor. This can be determined by co-irradiating a specimen of known age with the unknown specimen, in close proximity and for a fixed amount of time, using the following equation (Mitchell, 1968):

$$^{39}Ar = {}^{39}K\Delta T \int \phi_\epsilon \sigma_\epsilon d\epsilon \tag{2.1}$$

Where ϵ = neutron energy
ΔT = duration of irradiation
ϕ_ϵ = neutron flux at energy ϵ
σ_ϵ = neutron capture cross-section at energy ϵ

Equation 2.1 can be more easily incorporated into decay equations by creating the dimensionless parameter J using equation 2.2 below (Mitchell, 1968):

$$J = \frac{e^{\lambda t_m} - 1}{(^{40}Ar^*/^{39}Ar)_m} \tag{2.2}$$

Where λ = total decay constant of ^{40}K
t_m = age of flux monitor
$(^{40}\mathrm{Ar}^*/^{39}\mathrm{Ar})_m$ = measured isotopic ratio of flux monitor

By incorporating this parameter into a general equation for the ^{40}K/^{39}Ar decay scheme we get:

$$t = \frac{1}{\lambda} \ln[1 + J(^{40}Ar^*/^{40}K)_S] \tag{2.3}$$

Where t = age of specimen
λ = total decay constant for ^{40}K
J = dimensionless irradiation parameter from eq. 2.2
$^{40}\mathrm{Ar}^*$ = amount of radiogenic ^{40}Ar in specimen
^{40}K = amount of ^{40}K in specimen, determined by measurement of ^{39}Ar produced from the unknown during irradiation (McDougall and Harrison, 1999).

Thus, it is possible to calculate an age from measuring only the ^{40}Ar/^{39}Ar ratio in a single mineral separate, avoiding problems associated with measuring K and Ar separately, such as inhomogeneous distribution in a specimen (Faure and Mensing, 2009).

The most common minerals used for ^{40}Ar/^{39}Ar dating are muscovite, biotite, K-feldspar, and hornblende. Muscovite and biotite have high K content at ∼8% and approximate closure temperatures of 400 and 350°C, respectively (Harrison and Zeitler, 2005). Muscovite tends to be less likely to incorporate excess Ar, and also breaks down less easily during heating, making it a more reliable chronometer (Harrison and Zeitler, 2005). K-feldspar has K contents up to ∼17% and a fairly low closure temperature (∼130°C), while hornblende has very low K content (∼0.3-1%) and a higher closure temperature (∼500°C; Harrison and Zeitler, 2005). Only muscovite and biotite were used in this study.

Corrections

There are a number of corrections required before a measured ^{40}Ar/^{39}Ar ratio can be used to calculate an age. Since Ar makes up ∼1% of earths atmosphere, it can readily diffuse into minerals during or after formation (Faure and Mensing, 2009). Thus, an atmospheric Ar correction (or air correction) is applied to account for non-radiogenic ^{40}Ar. Mass discrimination is monitored by measuring atmospheric ^{40}Ar/^{36}Ar every day, and comparing that measured ratio

to a standard of 295.5 (Steiger and Jager, 1977) to get a correction factor. Since all ^{36}Ar in the sample is assumed to be atmospheric, we can use the known isotopic ratios of Ar to determine a base level of atmospheric ^{40}Ar read by the machine, and subtract this amount from the total measured ^{40}Ar (Renne et al., 2009).

During the irradiation process, several other isotopes beside the desired ^{39}Ar are formed that may interfere with measurements, the most important of which are those formed from Ca isotopes via ^{42}Ca(n,α)^{39}Ar and ^{40}Ca($n,n\alpha$)^{36}Ar reactions, because they will interfere with ^{39}Ar readings and atmospheric corrections (Merrihue and Turner, 1966; Faure and Mensing, 2009). Naturally occurring ^{37}Ar is generally negligible, and so all measured values of this isotope are assumed to be a byproduct of the irradiation process (McDougall and Harrison, 1999). By measuring the ^{37}Ar in a monitor, the amounts of neutron-induced ^{39}Ar and ^{36}Ar can be determined by comparison with known isotopic ratios. Other reactions also occur during irradiation, but their effect is negligible and are not discussed here. For more detail on interfering isotopes, see Dalrymple and Lanphere (1971), who developed an expression to relate the measured ^{40}Ar/^{39}Ar ratio to all necessary corrections. Line-blanks are also measured before every analysis to determine the base reading of each Ar isotope. Since the mass spectrometer measures the current associated with each isotope, a simplified equation outlining all corrections can be written as follows:

$$I_{measured} = I_{Ar^*} + I_{atm\ Ar} + I_{neutron\ Ar} + I_{blank\ Ar} \tag{2.4}$$

Where Ar* = radiometric Ar value used for age calculation
I = current
Atm Ar = atmospheric Ar
Neutron Ar = neutron reaction induced Ar
Blank Ar = base Ar reading

Similar corrections are made for all other Ar isotopes.

^{40}Ar/^{39}Ar age interpretation

In the simplest case, if an igneous rock cools and crystallizes quickly and remains at low temperatures until the rock is sampled and analyzed, the age provided may represent the crystallization age of that rock (e.g. Kelley, 2002b; McDougall and Harrison, 1999). If the rock cools more slowly, the ^{40}Ar produced in the early stages of cooling will not accumulate in the crystal, and the date obtained will be younger than the crystallization age. Similarly, if the rock was heated after initial cooling (to approximately greenschist facies or higher conditions), some or all of the trapped ^{40}Ar may be released, effectively 'resetting' the radiometric clock (e.g. Dodson, 1973; McDougall and Harrison, 1999). If the resetting is complete, i.e. all accumulated ^{40}Ar was released, then the age obtained will be the age of cessation of that resetting thermal

event, but if the system is only partially reset, i.e. not all accumulated ^{40}Ar escapes the rock, then the age found will be intermediate between the initial crystallization age and that of the resetting thermal event (e.g. Kelley, 2002b; McDougall and Harrison, 1999). In such cases the age obtained may be of no use, as there is no definite way to tell what proportion of the measured ^{40}Ar was produced before the resetting event and what proportion was produced after. However, this problem can often be overcome by use of the step-heating technique (Lanphere and Dalrymple, 1976), the results of which are usually portrayed in an age spectrum plot (Fig. 2.1).

In this application, an aliquot or single-crystal is heated to incrementally higher temperatures using a furnace (multiple-crystal) or higher power using a laser (single- or multiple-crystal), measuring the ^{40}Ar/^{39}Ar ratio at each step (Lanphere and Dalrymple, 1976; McDougall and Harrison, 1999). Diffusion of Ar from crystal sites happens from rim locations first, with greater temperatures or greater time periods at elevated temperatures needed to release Ar from core locations (Harrison and Zeitler, 2005). Thus, it is assumed that upon step heating, the gas trapped in the outer portions of a crystal is released first at low temperature, and each subsequent higher temperature step releases gases from deeper lattice sites (Fig. 2.1; e.g. Harrison and Zeitler, 2005). By this method, meaningful dates may be gleaned from a partially reset crystal, where gas from partially reset rim portions of the crystal is released at low temperatures, giving one date, and subsequent heating steps release gas from inner portions of the crystal where resetting didn't occur, giving a minimum date of the last heating event, whether it was initial crystallization or later metamorphism (Harrison and Zeitler, 2005). If the step-heating method yields little variation in the age obtained from each step, this forms a 'plateau' in the age-spectrum diagram, and the corresponding date of that plateau is called a plateau age. A large plateau typically indicates a simple cooling history, involving little to no thermal disturbance after crystallization (e.g. McDougall and Harrison, 1999).

A common problem with ^{40}Ar/^{39}Ar dating, especially in Himalayan biotite, is the presence of 'extra' ^{40}Ar in the crystal after corrections are made for non-radiogenic ^{40}Ar. Extraneous ^{40}Ar can enter a crystal lattice due to high partial pressure of Ar in the environment, or by being included within a xenolith, fluid inclusion, or sometimes will remain after imperfect resetting from a thermal event (e.g. Kelley, 2002a). The presence of excess ^{40}Ar can cause the release spectrum to appear 'saddle shaped' (Fig. 2.2), with early and late steps releasing the extra ^{40}Ar from the rim or inclusions, thus giving an older, perhaps inaccurate age (Kelley, 2002a). In this ideal situation the excess Ar is easy to detect, and meaningful information may still be obtained from the specimen, either by reading the center plateau age as a minimum age, or by using an inverse isochron plot (e.g. McDougall and Harrison, 1999). However, excess Ar in biotite may also yield perfect plateaus at improbably old ages, and biotite that experienced Ar loss can show flat or convex upward spectra (McDougall and Harrison, 1999). Nevertheless biotite regularly provides meaningful dates as it is usually possible to determine the reliability

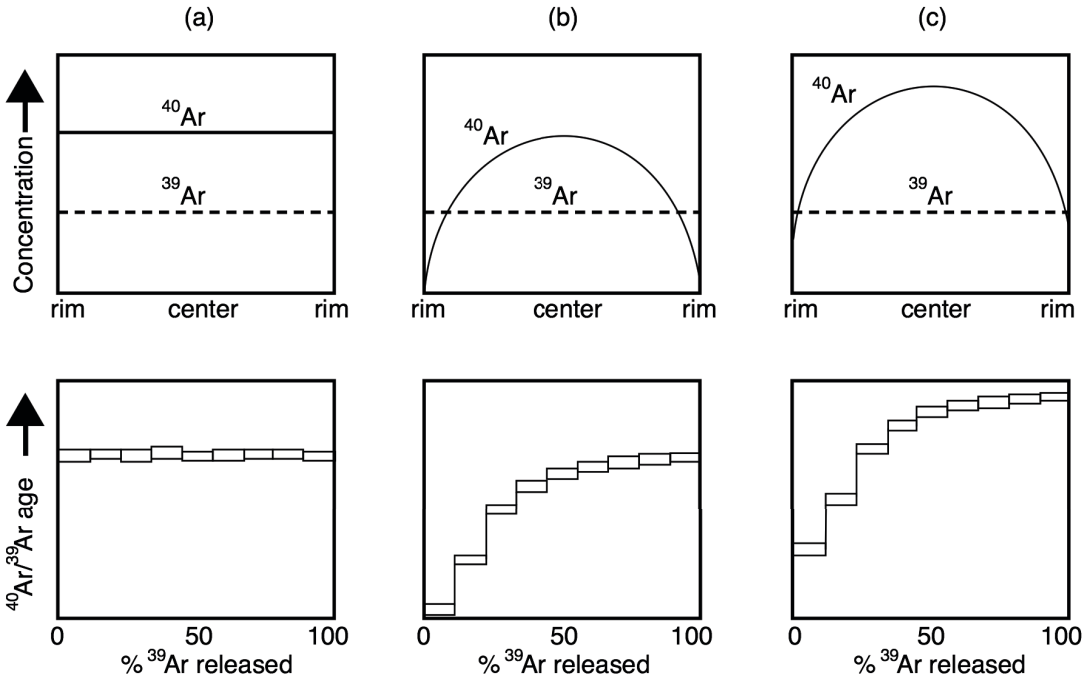

Figure 2.1: Idealized mineral $^{40}Ar/^{39}Ar$ concentration (top) and age spectra (bottom) for a) specimen that has not undergone subsequent heating since crystallization and shows a flat 'plateau', b) recent Ar loss, c) previous Ar loss with subsequent build up. Modified from Harrison and Zeitler (2005).

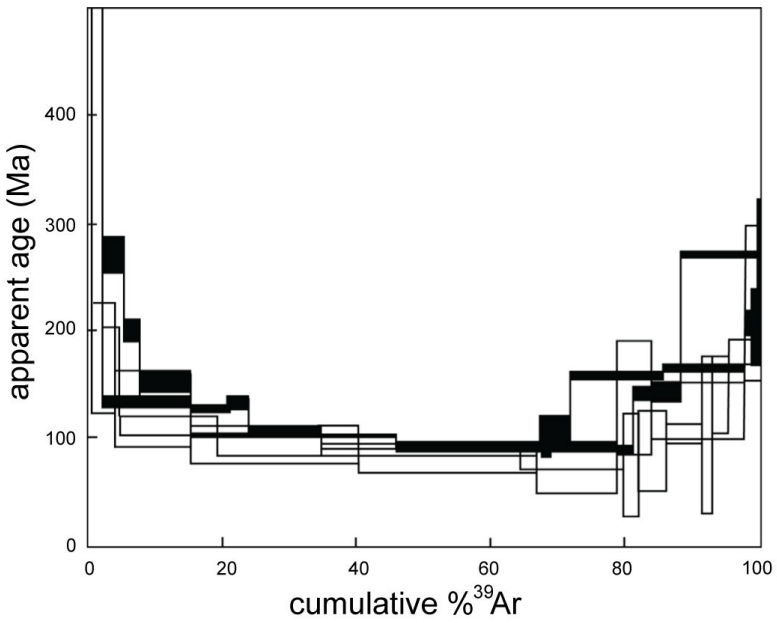

Figure 2.2: Typical 'saddle' shaped Ar release spectra diagram, showing excess Ar at first and last increments (right and left edges), and a small plateau in the middle. From (Kelley, 2002b).

of an $^{40}Ar/^{39}Ar$ date in biotite by interpreting it in conjunction with other dates from different systems such as $^{40}Ar/^{39}Ar$ muscovite dates (McDougall and Harrison, 1999).

Procedure

Before crushing, micas were scraped off and hand-picked from all specimens, except DK16, under a stereoscopic microscope using a scalpel and tweezers. The outcrop of Mustang Gneiss at the Dhanggna Khola station was badly weathered, and hence a specimen was retrieved from a float-block of the same material, assumed to be locally derived that was less badly weathered, however, cooling data obtained from a float block may not be representative of the cooling of the outcrop, so it was excluded from $^{40}Ar/^{39}Ar$ analysis. Scaled digital photographs were obtained to measure an average grain size for each specimen (Appendix B-II). Biotite and muscovite grains were then selected that had no visible inclusions or unusual colouration. Specimens were irradiated at the Oregon State University TRIGA reactor along with standards to determine the neutron fluence parameter, *J*. After a cool-down period, specimens were sent to the University of Manitoba for $^{40}Ar/^{39}Ar$ analysis. Crystals were step-heated using a CO_2 laser and the gas released measured in a multi-collector Thermo Fischer Scientific ARGUSVI mass spectrometer. Mass discrimination was monitored by online analysis of air pipettes for use in the atmospheric Ar correction, and corrections were applied for other irradiation-induced particles. Age calculation and age spectra diagrams were done on site using the MassSpec software (Deino, 2013). Closure temperatures were calculated separately for each crystal using equation 23 of Dodson (1973) and iterative determinations of cooling rate using Isoplot (Ludwig, 2003). Equipment, diffusion, and geometric parameters are outlined in Appendix A-II. $^{40}Ar/^{39}Ar$ isotopic data are detailed in Appendix C.

2.2.4 U-Th/He Thermochronology

Principle

Helium retained within minerals was first explored as a geologic dating method in the early 1900s (Zeitler et al., 1987, and references therein), and again several decades later by Hurley and Goodman (1941). These and similar early studies found that He ages obtained were much younger than U-Th/Pb ages from the same rock, a discrepancy which was attributed to incomplete He retention in the minerals being studied (Hurley and Goodman, 1941, 1943; Hurley, 1950). This method wasn't explored again until 1987, when it was recognized as a potential thermochronometer (Zeitler et al., 1987). It has since been developed into a useful low-temperature thermochronometer for several minerals including apatite (Ap), zircon (Zrn), and titanite (e.g. Farley et al., 1996). The method continues to evolve, with more accurate thermal modelling (Flowers et al., 2009; Ketcham et al., 2007, 2011; Shuster et al., 2006), and advances in technology such as the in-situ 'double-dating' (U-Th)/(He-Pb) method contributing

to a growing field of use (Reiners et al., 2002).

Helium is a decay product of the radioactive breakdown of U, Th, and to a lesser extent Sm. Uranium and Thorium-bearing minerals will retain daughter He within their crystal lattice after the mineral has cooled below its closure temperature (e.g. Dodson, 1973; Farley, 2000; Zeitler et al., 1987). The amount of He produced during decay can be calculated via the following formula (e.g. Faure and Mensing, 2009):

$$\begin{aligned} {}^4He_V = 22.41383 * [&0.0336 * U(e^{\lambda_{238}t} - 1) \\ &+0.00021173 * U(e^{\lambda_{235}t} - 1) \\ &+0.0258577 * Th(e^{\lambda_{232}t} - 1)] \end{aligned} \tag{2.5}$$

Where ${}^4He_V$ = volume of radiogenic ^{4}He at STP in µL/g
U, Th = concentrations of U and Th in µg/g
λ = respective radioactive decay constant
t = time

This equation is the basis for He dating. The volume of He, and concentrations of ^{238}U, ^{235}U, and ^{233}Th are measured from a crystal, then the equation is solved for the variable t to obtain an age.

The main advantage of this technique stems from the unique low closure temperature of He retention in apatite and zircon, approximately 70°C (Farley et al., 1996) and 200°C (Reiners et al., 2002) respectively, allowing geologists to examine very recent cooling histories. Helium also has advantages over other noble gas chronology such as ^{40}Ar/^{39}Ar dating in that He is far less abundant in the atmosphere, hence contamination from modern atmosphere during analysis is easier to avoid (Harrison and Zeitler, 2005). Since He is produced at a high rate from U and Th decay, it is useful for even very young samples, despite U and Th themselves generally appearing in low quantities within minerals (Harrison and Zeitler, 2005).

Helium is extracted from apatite and zircon either by in situ-methods, where He, U, and Th are all measured simultaneously from a single point on a crystal, or by whole-grain methods, where the crystal is heated by furnace or laser to extract the He and the grain is later digested in acid to obtain U and Th concentrations via isotope dilution mass spectrometry (e.g. Faure and Mensing, 2009; Harrison and Zeitler, 2005). After these volumes and abundances are determined, an initial date can be calculated, however, some corrections must be applied to improve its accuracy.

Corrections

Inclusions in apatite, if they are U or Th bearing, can contribute additional He to the crystal lattice. If the parent U or Th to this He is not accounted for - for example a zircon inclusion will not dissolve in nitric acid typically used during the isotope dilution process for apatite, so

U and Th inside will not be measured - then the He that was produced is called 'parentless' and any age measured will be older than the real age (e.g. Vermeesch et al., 2007). Vermeesch et al. (2007) explored the effects of U-bearing inclusions in apatite, and found that if a single inclusion is less than a few percent of the length, width, and height of the crystal, the parentless He it contributes to the lattice is probably negligible. The authors suggest a method to account for parentless He in samples with numerous small inclusions, or with inclusions larger than the suggested limit, whereby the entire grain is digested in hydrofluoric acid (HF) instead of a weaker acid which is the norm. Hydrofluoric acid will dissolve the apatite and the included zircon, and thus the otherwise parentless He will not skew the age (Vermeesch et al., 2007). This method may make it possible to date specimens with apatites that are otherwise unusable, however, the more aggressive acid technique is more time consuming and expensive, limiting its practical use. Inclusions in zircon tend to be even less of an issue, as the few minerals that commonly occur as inclusions within zircon contain little to no U, and the hot HF bath used to digest zircon will certainly dissolve any inclusion within - eliminating the possibility of parentless He.

Alpha particles (He) ejected from U and Th during decay travel some distance within a crystal lattice (∼20µm), and if that distance is greater than the distance from the source to the edge of the crystal, it may be ejected out of the lattice, thus any measured He is assumed to be less than what was produced (Farley et al., 1996). Farley et al. (1996) determined that the retentivity of alpha particles varies with parent nuclide and host mineral, and depends largely on crystal size and morphology. This He loss can be corrected for using an 'FT' or 'alpha ejection' factor ('FT' from Farley's original retentivity equation derivations). This correction can be applied easily using a computer program if the total U and Th concentrations, size, and morphology of the grain is known. The morphology information needed for apatite is simply whether the crystal analyzed had 0, 1, or 2 complete terminations. The authors also provide a minimum grain-size necessary for analyses, as any grain with 1 or more dimensions <60µm would result in an unacceptably large FT correction (Farley et al., 1996). FT corrections assume an even distribution of U and Th within the crystal, but if there is zoning the amount of alpha ejection from the edge of the crystal could be greater or lesser than in a homogeneous crystal, causing the FT correction to be less accurate (Meesters and Dunai, 2002).

Closure temperature and thermal modelling

Closure temperature for the ApHe system was first calculated to be ∼105 ± 30 °C by Zeitler et al. (1987). In the years following several authors conducted step-heating diffusion experiments and calculated closure temperatures varying from 68 °C to 130 °C (e.g. Farley, 2000; Lippolt et al., 1994; Wolf et al., 1996). The closure temperature concept, however, is a simplification of reality. In nature, the transition from temperatures above which no He is retained within a crystal lattice, to temperatures below which all He is retained within a

crystal lattice may not happen immediately (e.g. McDougall and Harrison, 1999). This window of temperatures over which a gradual shift from total loss to total retention occurs is referred to as the partial retention zone (PRZ; McDougall and Harrison, 1999). Recently, Shuster et al. (2006), and Flowers et al. (2009) examined the effect of radiation damage on the diffusion of He in apatite, and found that the presence of radiation damage tracks (both alpha-ejection and fission tracks) in slowly cooled samples will act as 'traps', and initially increase He retentivity until the tracks are so numerous as to create an open channel to the edge of the crystal, at which point retentivity decreases. The amount of time spent in the radiation damage PRZ (a range of T similar to that of the He PRZ) depends on cooling rate and will affect the formation and annealing of radiation damage (Flowers et al., 2009; Shuster et al., 2006). Using effective uranium (eU = U + 0.235∗Th), and parameters derived from fission track dating to model annealing behaviour, the authors determined an effective proxy for radiation damage and have outlined a dynamic T_c for ApHe, varying with total eU and cooling rate, ranging from 44 °C to 116 °C (Shuster et al., 2006). Furthermore, this model has been incorporated into the thermal modelling software HeFTy (Ketcham, 2005), where the software compares model ages based on eU and grain dimensions to measured ages in order to obtain cooling paths that are sensible given user-input thermal constraints (Flowers et al., 2009).

The closure temperature for the zircon U-Th/He (ZrnHe) system was originally determined to range from 200-220 °C, but the authors also recognized that the T_c can vary over the life of a crystal (Reiners et al., 2002). Wolfe and Stockli (2010) examined ZrnHe diffusion behaviour from a drill hole in Germany and determined that the system behaves similarly to laboratory experiments, however more recent studies (Guenthner et al., 2013) have shown a complex relationship between He diffusion kinetics and radiation damage within zircon, similar to that in apatite. Radiation damage in zircon initially decreases diffusivity (increases retention) within the crystal, until enough damage paths are formed that interconnected 'fast-pathways' form for He to escape the crystal, at which point diffusivity greatly increases (Guenthner et al., 2013). Instead of damage tracks creating 'traps' as is the case proposed for apatite by Shuster et al. (2006), Guenthner et al. (2013) have an alternative interpretation, where the radiation damage act as 'roadblocks' that block otherwise fast *c*-axis diffusion paths in zircon, forcing the He into slower diffusion paths. Thus, the tortuosity of He diffusion paths increases with radiation damage, until a level of interconnectedness allows fast He diffusion (Guenthner et al., 2013). From this model, the ZrnHe system has an effective T_c in the range of 140-220 °C (Guenthner et al., 2013). The authors also apply their diffusion model to the thermal modelling software HeFTy, using fission-track annealing and eU to approximate radiation damage in zircon, in order to determine geologically reasonable cooling paths (Guenthner et al., 2013).

Helium diffusion in apatite and zircon is most complex in slowly cooled samples that spend a long time in the He PRZ and/or radiation damage PRZ, and in samples with high eU (e.g. Flowers et al., 2009; Guenthner et al., 2013). The effect of radiation damage is probably negligi-

ble in young specimens that cooled quickly, and samples with low eU, but this will, nonetheless, be accounted for when modelling cooling paths using HeFTy.

Procedure

Specimens sent to UCSB (GG01A, GG10, GG12, DK14, DK15, and Gh17B) were crushed using a Fritsch jaw crusher and sieved to 355µm. The <355µm portion was triple-rinsed before being separated into heavy and light portions by hand gold-panning. The heavy portion was further separated using MI, to extract zircon. The MI 'lights' were further separated to better isolate apatite using bromoform (∼2.89 g/cm^3 density). Specimens were then run 3 times through a Frantz magnetic separator at 0.5, 1.0, and 1.5 amps, with a 15° sideways tilt and a 5° backwards tilt. Specimens GG01B, GG11, and GG13 underwent a similar process at the University of Calgary. They were crushed using a Braun Chipmunk jaw crusher and a BICO pulverizer (disk grinder) before being run through a water table to separate into light, intermediate, and heavy portions. The water table 'heavies' were further separated using the same bromoform/MI process as above, before magnetic separation in the Frantz instrument.

Typically apatite should appear in the non-magnetic portion of the separates, however in this case this was only true for DK14. For the other specimens, apatite was mostly in the 1.0 and 1.5 amp magnetic portions. This is not believed to be caused by the Frantz, but rather a result of the nature of the crystals. One possibility is that they were not completely physically separated from neighbouring magnetic crystals, and hence were 'pulled' into the wrong track of the Frantz. Unusual composition is also a possibility; geochemical data is not available for individual apatite grains.

Separates containing apatite and zircon were hand-picked in petri dishes under a stereoscope. Desirable crystals had few to no inclusions, smooth and unchipped surfaces, two complete terminations, and every dimension >60µm. Not all of these requirements could always be met for these samples, instead these factors were considered together to choose the best crystals. All crystals with one or more dimension <60µm were excluded, as this produces an alpha-ejection correction that is unacceptably large (Farley et al., 1996), as discussed previously. Apatite crystals with large and/or numerous inclusions were excluded, however, since small inclusions (even those containing U or Th) tend to have a negligible effect on obtaining accurate dates in (Vermeesch et al., 2007), some crystals with small inclusions were used if they had other desirable qualities. Inclusion-free crystals with 0-1 terminations were, however, chosen over those with inclusions and 2 terminations, as this imperfection can be corrected for in alpha ejection calculations, whereas an inclusion with unknown composition cannot be corrected for without completely dissolving all crystals in HF (Vermeesch et al., 2007), an impractical practice for most apatite studies. Inclusion-free zircons are also preferred over those containing inclusions, however, this is mainly so the volume calculations are accurate and the diffusion behaves as expected, opposed to the possibility of parentless He as is the case with apatite.

Five specimens (GG01A, GG10, GG12, DK14, and Gh17B) contained apatite suitable for analysis, and 4 specimens (GG01B, GG11, DK14, and Gh17B) contained usable zircons. Annotated digital photographs of the selected grains are in Appendix B-III and B-IV. Retrieving suitable crystals from the heavy mineral separates was challenging because they contained low numbers of apatite and zircon, and the majority were of poor quality. Crystals commonly contained multiple inclusions, were badly broken, or too small. However, it was possible to retrieve a total of 29 suitable apatites from the 5 specimens, with relatively few, very small inclusions, and minimal surface irregularities or chips (Appendix B-IV). Similarly, a total of 18 suitable zircons across the 4 specimens were picked for analysis, using the same criteria as for apatite.

Once suitable crystals were selected, they were measured and photographed, then placed by hand into small Nb tubes. Niobium tubes are used instead of the traditional Pt tubes to avoid interference during isotope dilution mass spectrometry. Ar added in the nebulizing process contributes an atomic mass of 40, which, when added to Pt (atomic mass 195), can interfere with readings of ^{235}U. Since Nb has an atomic mass of only 92, this interference is avoided. The capsules were crimped perpendicularly on each end to create an air pocket inside to avoid damage to the crystal during transport. Three 'hot blanks' (empty Nb packets), and 4 Durango apatite shards (for Ap) or Fish Canyon Tuff zircon (for Zrn) were placed in Nb packets to be used as monitors to measure any drift in base He readings during heating.

Packets were then loaded into an ASI Alphachron He system at the University of Calgary, which uses a Prisma-Plus quadrupole mass spectrometer for He readings. After calibrating the machine to the packet locations and pumping down the vacuum, a sequence was set with hot blanks, standards, and line blanks (readings of ^{3}He straight from tank) dispersed among the samples to calculate drift during the analysis. Packets containing apatite were heated by the laser for 5 minutes each, at 9 amps, after which a re-extraction was done to ensure all the He was released. Zircon packets were heated by the laser for 15 minutes each, at 12 amps, plus a re-extraction.

After He extraction was complete, apatite packets were loaded into vials and dissolved for 4 hours in nitric acid along with a U-Th spike, a U-Th stock solution, and water. Ten stock-solution-only and 9 Sm-spike-vials were run interspersed with the packets to later calculate drift due to evaporation. Since the Sm solution is based on concentration, it drifts over time as water evaporates from the solution. The U-Th spikes on the other hand are based on the ratio of U and Th in the solution, so as water evaporates the ratio remains constant even if the concentration changes. The interspersed vials are analyzed using an Agilent 7700x quadrupole mass spectrometer. Data reduction for apatite was done with a series of spreadsheets, and an FT correction factor calculated based on total U and Th present in the crystal and its size and shape using a freely distributed alpha ejection program written by Gautheron et al. (2011). After degassing, zircon crystals were sent to the University of Colorado, Boulder, for digestion and isotope dilution. Zircon packets were placed in Savillex vials, to which a ^{235}U/^{230}Th spike

and 200 µL HF were added. The vials were heated at 220 °C for 72 hours, and after cooling, uncapped and dried on a hot plate. A second round of dissolution in HCl was then done to remove fluorine salts created during the first digestion. 200 µL of HCl were added to the vials, which were then baked at 200 °C for 24 hours before again cooling and drying. After a third round of dissolution in 200 µL of HNO_3:HF mixture in an oven at 90 °C for 4 hours, samples, along with standards and blanks, were diluted with deionized water and analyzed by the Thermo Element 2 magnetic sector mass spectrometer (ICP-MS) at the Colorado University Institute for Arctic Alpine Research. Data reduction and age calculations for zircon were done in custom spreadsheets based on the methods of Ketcham et al. (2011).

Cooling Paths

Several geo-thermochronometers from the same locality can be used to determine the cooling path of a package of rocks. If closure temperatures are known for each mineral system dated, and plotted against ages, a simple linear regression between points would outline a basic cooling path. However, computer modelling may be used to quickly compute many more plausible paths, hence apatite and zircon thermochronologic data were entered into the thermal modelling software HeFTy (Ketcham, 2005), along with temperature-time constraints from U-Th/Pb and $^{40}Ar/^{39}Ar$ dating. The reverse-modelling function of the program was used, where HeFTy tested ten thousand random cooling paths, calculating a model age for the entered grains (based on dimensions and eU), and comparing that to measured crystal ages to find a best-fit path that matches all ages. For apatite grains, the radiation damage accumulation and annealing model parameters of Flowers et al. (2009) were used, and for zircon, the parameters of Guenthner et al. (2013).

The HeFTy program requires specific U and Th abundances, as well as an effective radii and the uncorrected age from a single crystal of apatite and/or zircon. One cooling diagram was created for each field site, using the zircon or apatite crystal that yielded a corrected U-Th/He age closest to that of the preferred mean age from the same location. The other, manually entered, age constraints used in modelling were the U-Th/Pb and $^{40}Ar/^{39}Ar$ ages from the same specimen where available, and from a neighbouring specimen otherwise. Cooling rates are determined graphically from the completed cooling path diagrams. The steepest and shallowest positive lines that can be fit between two constraints without exiting the envelope that surrounds all good paths are the maximum and minimum cooling rates for that time interval, respectively (see section 3.3).

Chapter 3

Results

3.1 Petrology

Petrology Results

Field sampling locations are shown in Fig. 3.1. Field relationships at each site are highlighted in Figures 3.2, 3.3, and 3.4 and are detailed below. Point-counting of minerals in thin-sections (Figs. 3.5 and 3.6) was used to classify the specimens using the International Union of Geological Sciences (IUGS) ternary diagram (Fig. 3.7). In this scheme, plagioclase with anorthite percent <5% is qualified as an alkali feldspar, hence scanning electron microscope analysis of plagioclase was used to determine how much plagioclase should be classified as alkali feldspar. Grain-sizes mentioned in the following descriptions are as per Winter (2010), and mineral abbreviations are after Whitney and Evans (2010).

The outcrop at Ghami (Fig. 3.1) exposes ∼1 m wide undeformed Mugu leucogranite dikes and dikelets that cross-cut the foliation of the host TSS (Fig. 3.2). Specimen GH17B is a sample of one of the dikes. It is a medium-grained Qz + Kfs + Pl + Bt granite with 12.5% of its plagioclase in the An_{0-5} range (see QAP diagram Fig. 3.7). Feldspar in thin section is characterized by local development of perthitic texture (Fig. 3.5).

Specimen collection at Ghar Ghompa was more extensive, with 6 specimens sampled from Mugu batholith material (Fig. 3.1). Specimens GG10, GG11, and GG12 were sampled from outcrops of the contact between the main body of the Mugu batholith and the TSS (Fig. 3.3). Specimens GG01A, GG01B, and GG13 are also assumed to be from the main body of the Mugu batholith, however, their contact with the TSS was not observed. Specimen GG01A is a medium-grained Qz + Kfs + Pl + Ms + Bt granite (Fig. 3.7) in which feldspar exhibits perthitic texture locally and minor sericitic alteration in the plagioclase. 40% of plagioclase from specimen GG01A has a composition of An_{0-5}. GG10 is a fine-grained equigranular alkali-feldspar granite (Fig. 3.7) that contains Qz + Kfs + Pl + Ms + Tur ± Grt with 100% of the plagioclase in the An_{0-5} range. GG12 is a fine- to medium-grained Qz + Kfs + Pl + Ms + Tur granite (Fig. 3.7) with minor perthitic texture in the feldspar and minor sericitic alteration in the plagioclase (Fig. 3.5). None of the plagioclase in GG12 is within the An_{0-5} range. No thin sections were made from specimens GG01B, GG11, and GG13, but from hand sample they are all identified as medium-grained granites *senso lato*, consisting of Qz + Kfs + Pl + Ms + Tur ± Ms ± Grt. The TSS at Ghar Ghompa is locally metamorphosed to staurolite grade, and

appears to quickly decrease in grade with distance away from the granites.

Both Mugu batholith and Mustang gneiss material crop out in the Dhanggna Khola area (Figure 3.1); TSS material was not present. At this location, badly weathered leucocratic orthogneiss (DK16) is cross-cut by a vertical ∼1+ m wide coarse-grained, undeformed granite dike, which in turn is cut by two near-horizontal, narrower (∼15 cm wide) undeformed fine-grained leucogranite dikes (DK15; Fig. 3.4). DK15 is a fine-grained granite containing Qz + Kfs + Pl + Ms + Tur and minor perthitic texture in some feldspar, with none of the plagioclase falling in the An_{0-5} range. DK16 is a fine- to medium-grained porphyritic Qz + Kfs + Pl + Bt + Ms granitic orthogneiss (Fig. 3.7), with large Kfs porphyroclasts, and minor sericitic alteration seen in the plagioclase (Fig. 3.6). This specimen contains no plagioclase that falls in the An_{0-5} range. Specimen DK16 is the only one collected in this study that exhibits deformation, which is manifested in thin section in the form of sutured quartz grains with weak subgrain boundaries and aligned biotite flakes (Fig. 3.6). Specimen DK14 is a medium-grained to pegmatitic Qz + Kfs + Pl + Ms + Tur alkali-feldspar granite (Fig. 3.7), with 100% of the plagioclase falling in the An_{0-5} range. This specimen is inequigranular and contains large Ms books and perthitic Kfs that exhibits minor sericitic alteration (Fig. 3.6).

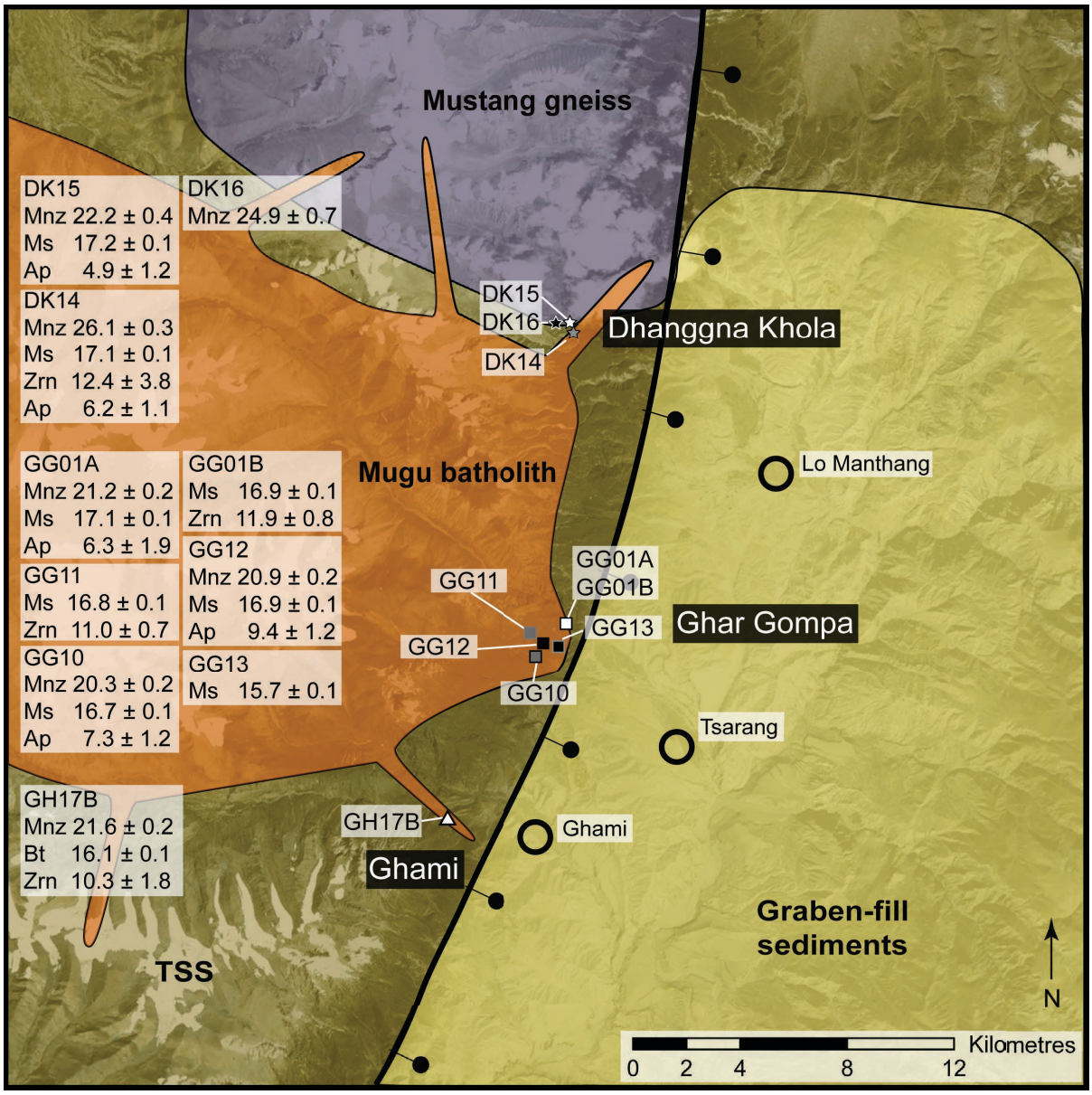

Figure 3.1: Sampling locations and respective U-Th/Pb (Mnz - minimum crystallization age), $^{40}Ar/^{39}Ar$ (Ms & Bt - pleateau age), and U-Th/He (Ap & Zr - central ages) dates (in Ma) for each location. Details about different types of ages are discussed in section 3.2. Symbol shapes represent sampling location: triangle for Ghami, squares for Ghar Ghompa, and stars for Dhanggna Khola. Symbol colouring is unique to each specimen and consistent throughout this document.

Figure 3.2: Outcrop at the Ghami location, showing leucogranitic Mugu dikes cross-cutting the bedding of the TSS.

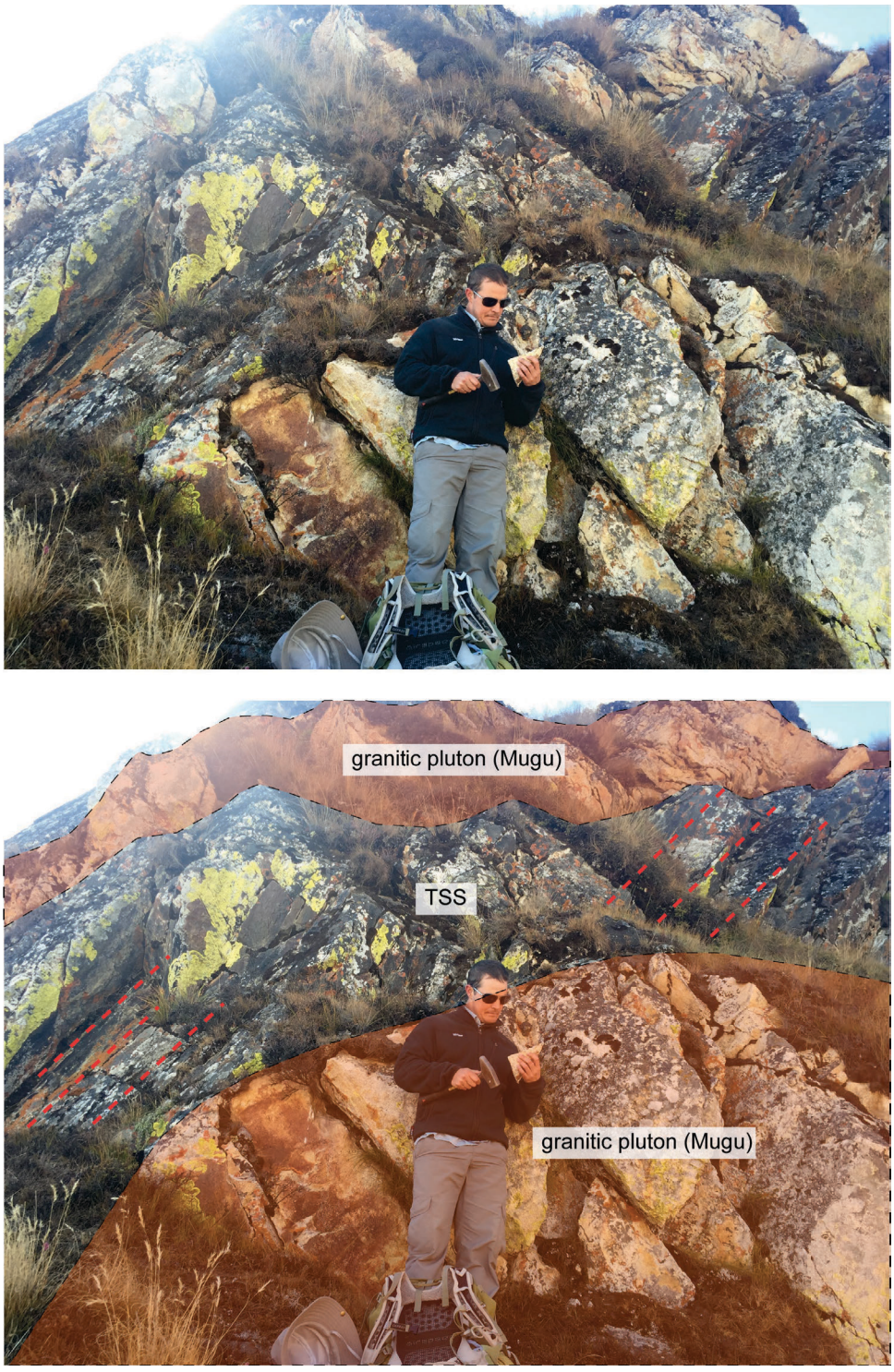

Figure 3.3: Outcrop at the Ghar Ghompa location showing intrusive contact between the fine-grained granitic Mugu batholith and unmetamorphosed TSS. Red dashed lines outline the trace of bedding in the TSS.

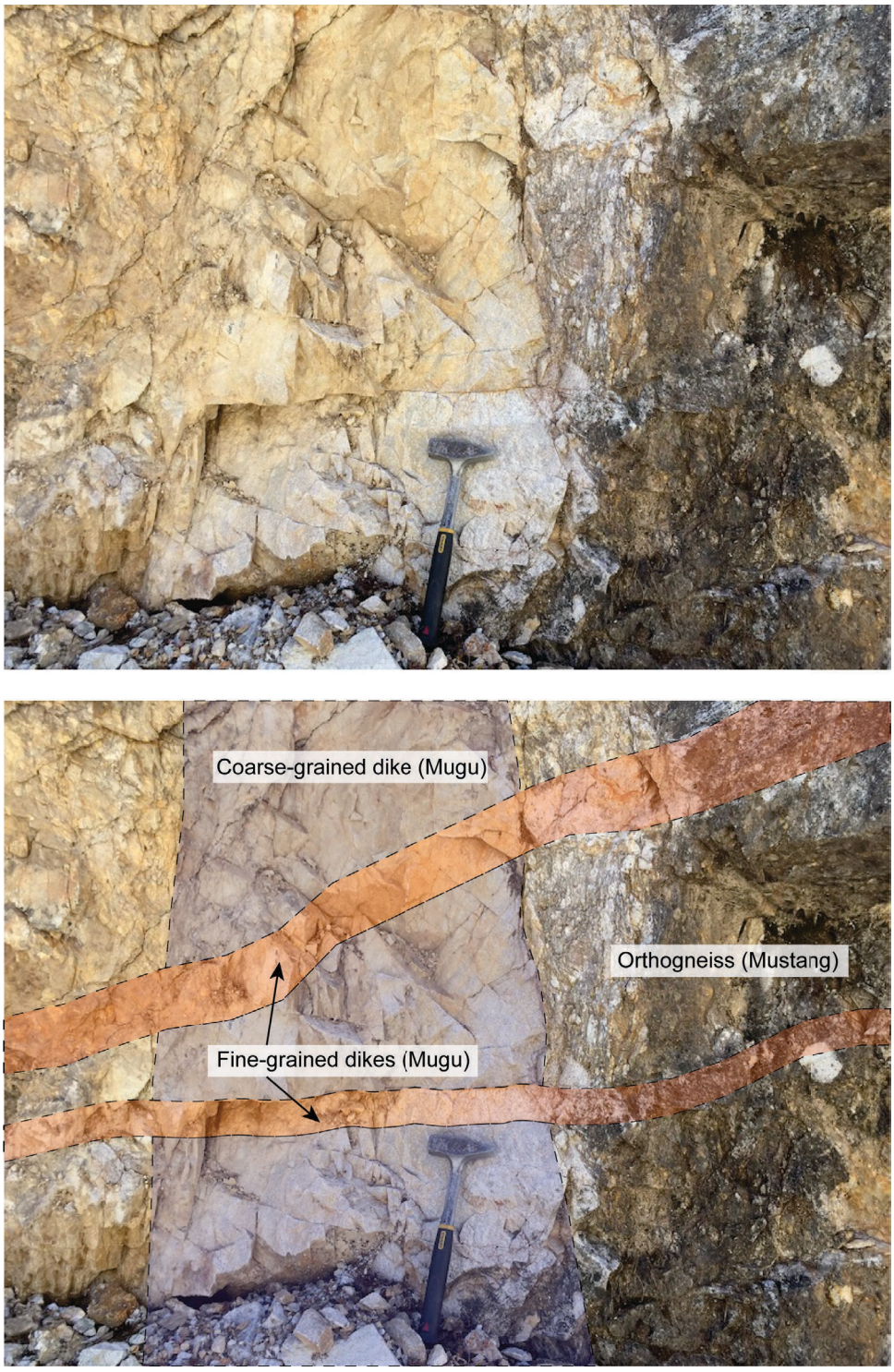

Figure 3.4: Outcrop at the Dhanggna Khola location, showing two fine-grained leucogranite dikes horizontally cross-cutting both a larger coarse-grained granite vertical dike, and badly weathered granitic orthogneiss. Hammer is approximately 30 cm long.

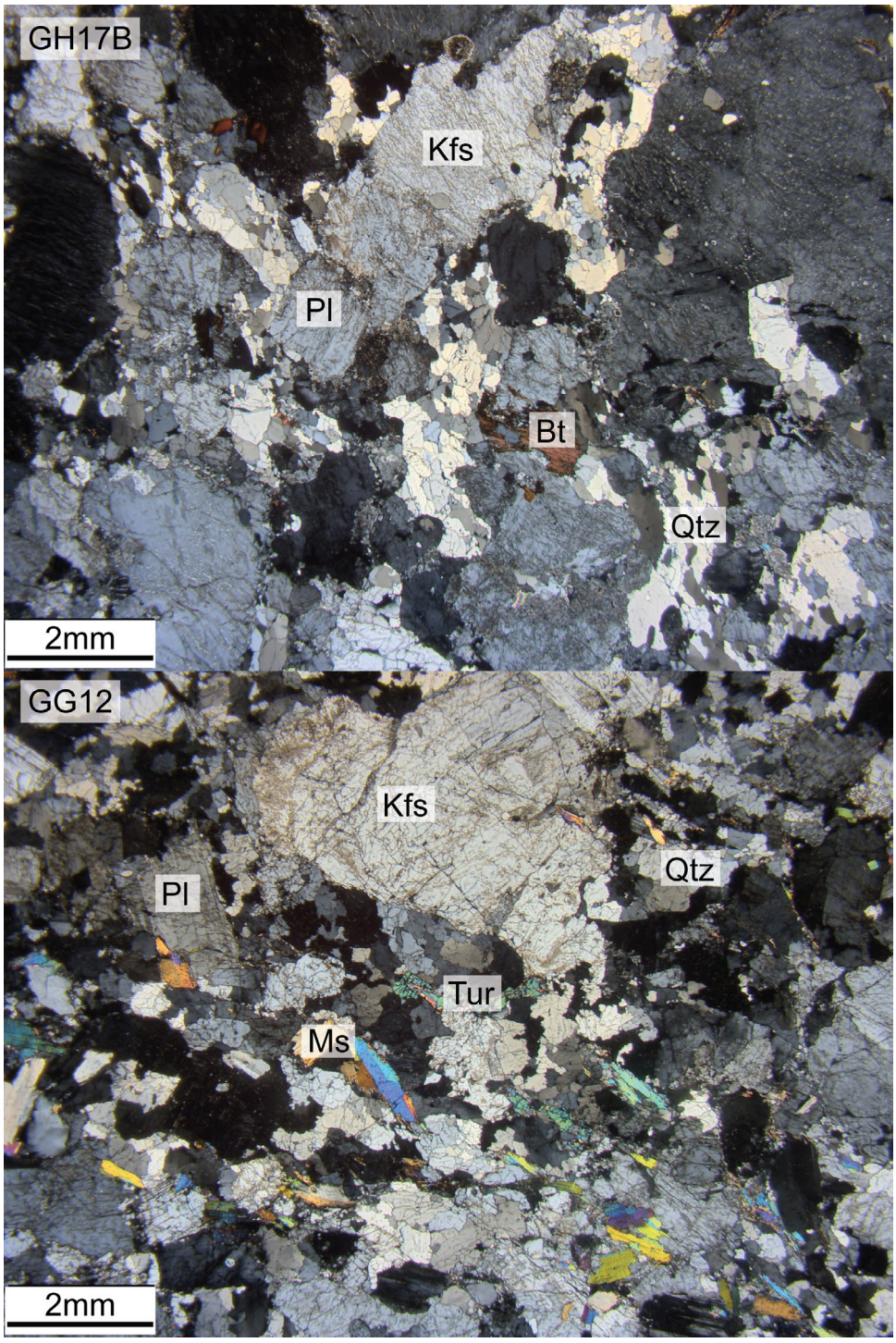

Figure 3.5: Representative digital photographs of thin-sections from the Ghami and Ghar Ghompa sites. Mugu dike specimen GH17B (top) and Mugu specimen GG12 (bottom) in cross-polarized light, exhibiting typical mineralogy and textures seen in the granites.

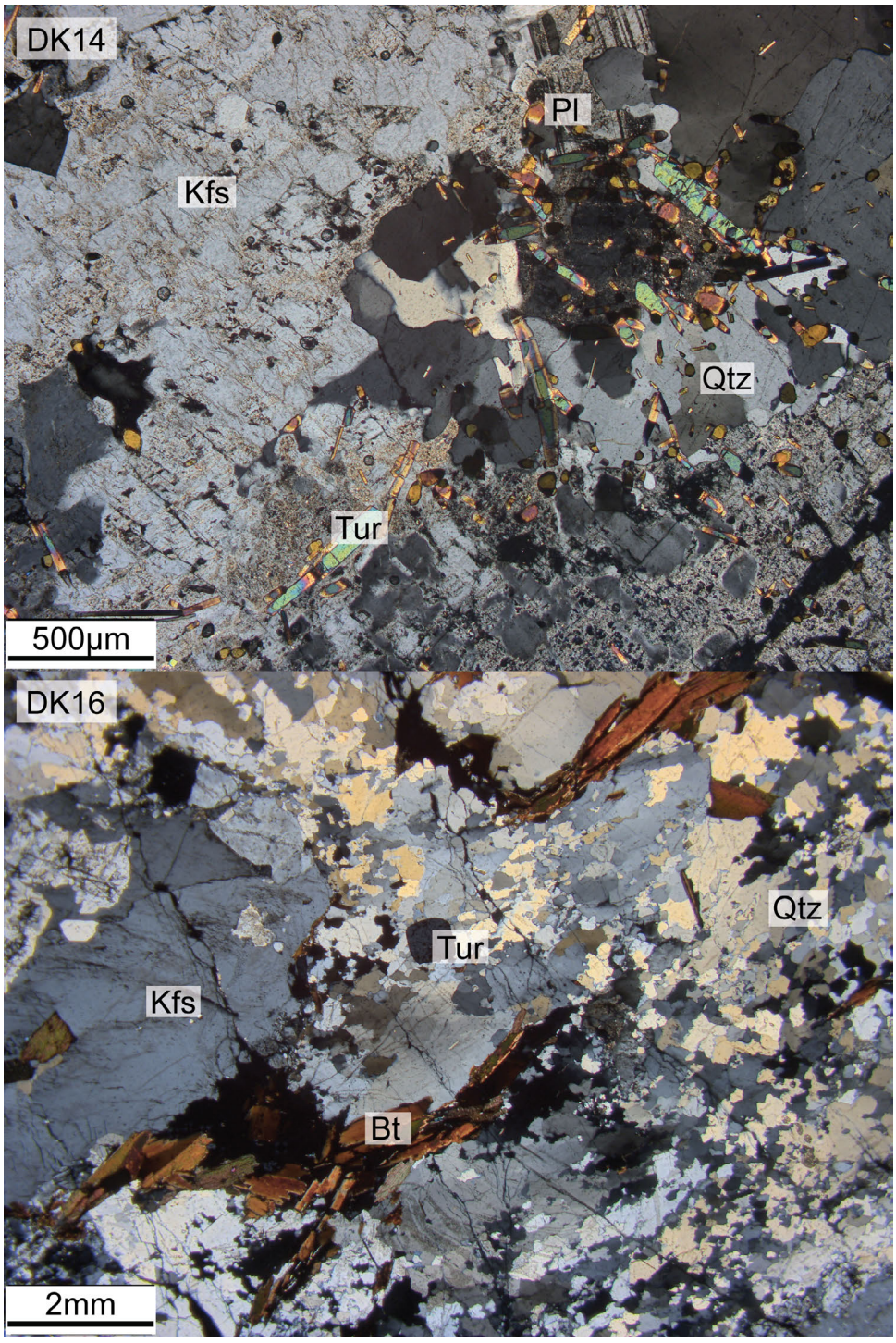

Figure 3.6: Representative digital photographs of thin-sections from the Dhanggna Khola area. Mustang granite specimen DK14 (top) in crossed-polars, showing perthitic K-feldspar megacryst and abundant tourmaline. Mustang gneiss specimen DK16 (bottom) in crossed-polars, exhibiting sutured quartz grain boundaries and weakly aligned biotite.

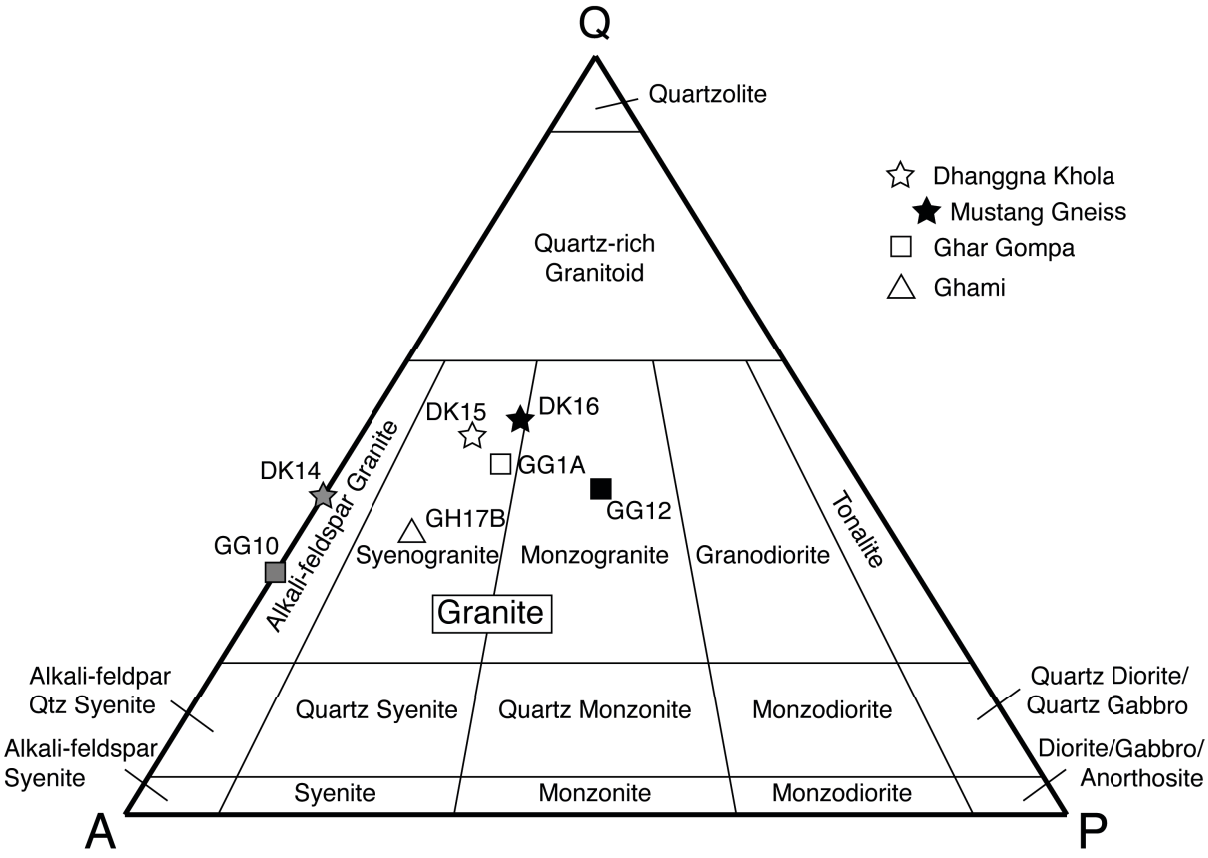

Figure 3.7: IUGS QAP diagram. Compositions determined by thin-section point-counting technique.

Petrology Interpretations

The TSS is locally metamorphosed to staurolite-grade at Ghar Ghompa, which appears to be due to contact metamorphism, as the grade shows a relationship with proximity to the Mugu batholith. No other evidence of TSS metamorphism was observed in this study, contrary to the observations of Hurtado (2002), who, in the same area, identified a unit classified as a black fine-grained gneiss.

Eight of the ten specimens collected are from Mugu batholith material (Fig. 3.1). These specimens are all fine- to medium-grained undeformed granites or alkali feldspar granites (Fig. 3.7), consisting of Qz + Fsp ± Ms ± Bt ± Tur. The remaining specimens (DK14 & DK16), are interpreted as belonging to a separate granitic body, commonly called the Mustang granite, which is observed in the field to have both orthogneiss and granite components.

The Mugu batholith is an undeformed granite broadly consistent with other Oligocene-Miocene Himalayan plutonic rocks, interpreted as S-type granites (Deniel et al., 1987; Le Fort et al., 1987; Searle et al., 2009). In contrast to previous work, which interpreted it to be a deformed Himalayan leucogranite, the Mustang intrusion as investigated in this study is considered a pervasively deformed orthogneiss. An undeformed, cross-cutting pegmatitic granite sampled from within the Mustang orthogneiss (specimen DK14) could represent a late-stage melt related to the metamorphism of the body. A more detailed structural and geochemical study focusing on the Mustang gneiss is needed in order to properly investigate the relationship between the orthogneiss, the pegmatitic granite, and their respective contacts with the surrounding TSS, which as of yet, has not been observed.

3.2 Geochronology

Three geochronologic systems were used to date the crystallization and cooling of the Mugu batholith and Mustang gneiss; U-Th/Pb in monazite, $^{40}Ar/^{39}Ar$ in muscovite and biotite, and U-Th/He in zircon and apatite. All ages are plotted with their respective sampling locations in Fig. 3.1, and are detailed in the following sections.

3.2.1 U-Th/Pb in Monazite

U-Th/Pb Geochronology Results

$^{208}Pb/^{232}Th$ monazite ages are shown in weighted mean diagrams below (Figs. 3.8, 3.9, and 3.10). Box heights are 2σ. Plots and ages were generated using the program Isoplot (Ludwig, 2003). The $^{208}Pb/^{232}Th$ system is preferred as monazite commonly contain weight% Th and it avoids potential complications of unsupported ^{206}Pb derived from the decay of ^{230}Th (Schärer, 1984).

Forty monazite crystals from specimen GH17B were dated (Fig 3.1) yielding a narrow range of ages from 21.1 ± 0.8 Ma to 25.0 ± 1.1 Ma (Fig. 3.8).

Three specimens were dated from the Ghar Gompa location (GG01A, GG10, and GG12; Figs. 3.1 and 3.9). The 40 monazite grains dated from GG01A yield a range of ages from 20.7 ± 0.8 Ma to 85.4 ± 8.5 Ma, while specimen GG10 yielded a range of monazite ages from 18.9 ± 1.1 Ma to 46.1 ± 6.0 Ma, over the same number of grains. 40 monazite grains from specimen GG12 were also analyzed, with ages ranging from 18.1 ± 0.9 Ma to 78.4 ± 18.3 Ma.

Three more specimens were dated from the Dhanggna Khola location (Fig. 3.1). Specimen DK16, a sample of the Mustang orthogneiss, and yields a wide range of ages from 24.3 ± 1.6 Ma to 535.1 ± 35.0 Ma over 39 grains analyzed (Fig. 3.10). DK14 is a medium-grained to pegmatitic dyke. It yields a wide range of ages over the 40 monazite grains analyzed, from 23.7 ± 0.9 Ma to 488.8 ± 18.2 Ma. Finally, monazite from specimen DK15, a Mugu-affinity dike that cross-cuts the foliation of the Mustang orthogneiss, yields a range of monazite ages from 21.3 ± 0.9 Ma to 38.7 ± 2.0 Ma over the 40 grains dated.

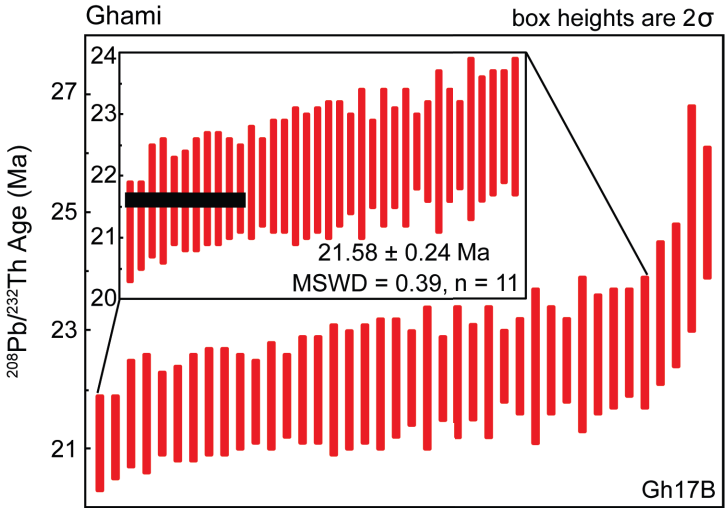

Figure 3.8: Weighted mean diagram of U-Th/Pb monazite dates from Ghami. Interpreted minimum crystallization age in inset, uncertainty indicated by width of black box.

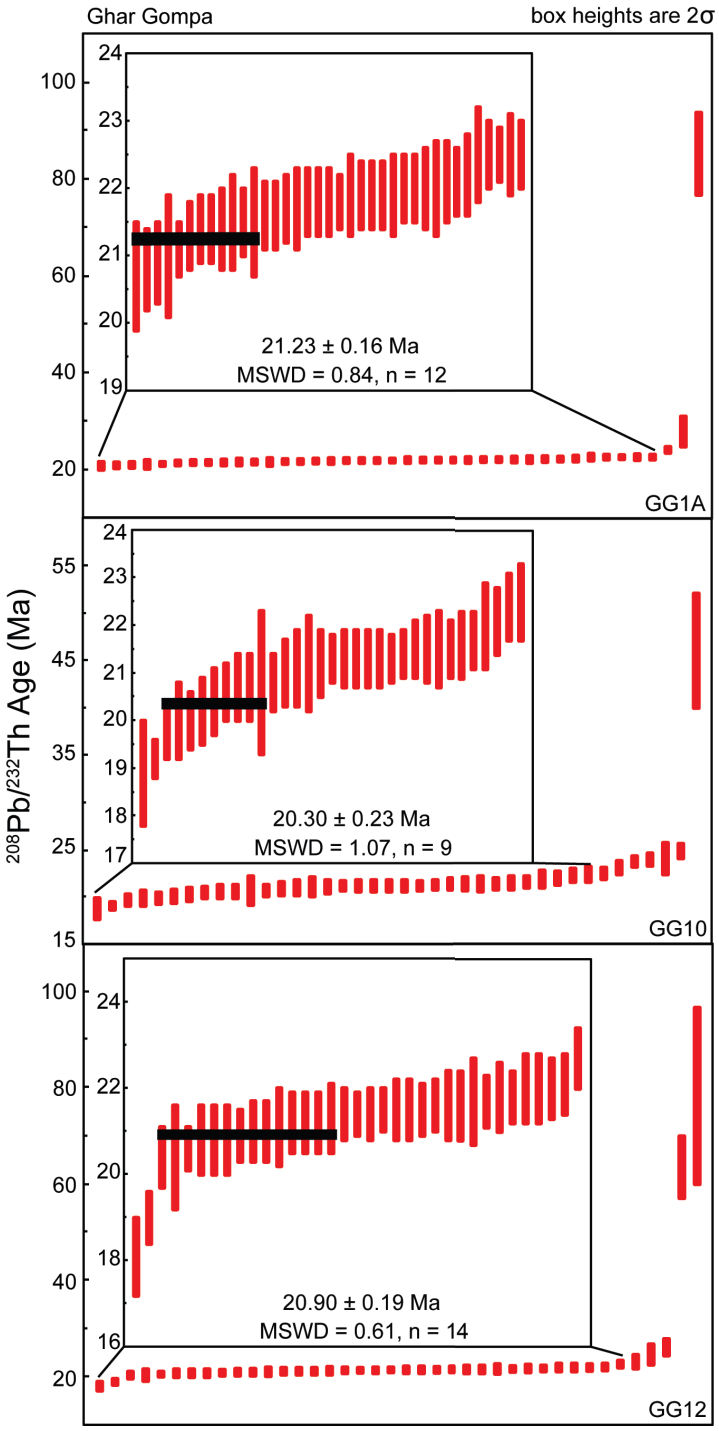

Figure 3.9: Weighted mean diagram of U-Th/Pb monazite dates from Ghar Ghompa. Interpreted minimum crystallization age in inset, uncertainty indicated by width of black box.

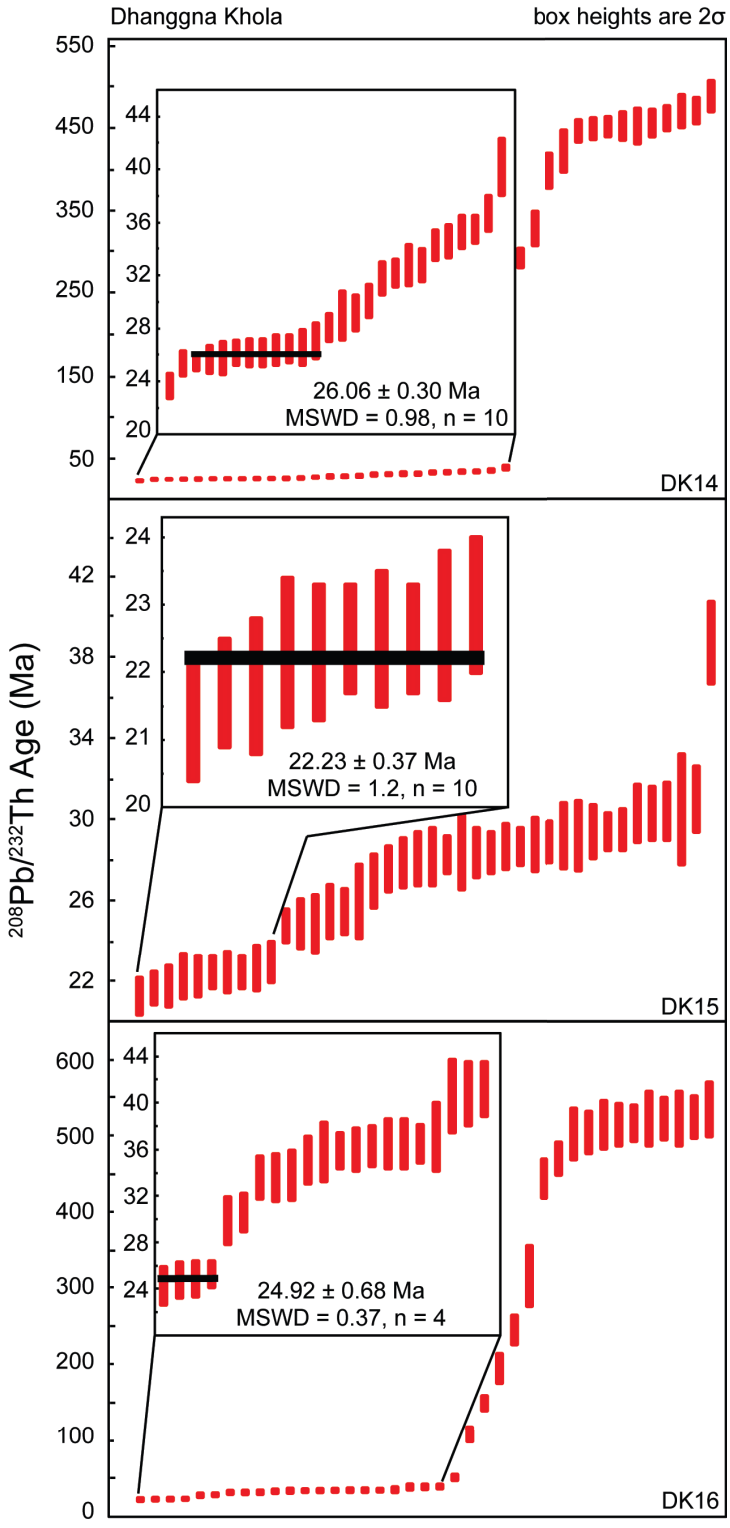

Figure 3.10: Weighted mean diagram of U-Th/Pb monazite dates from Dhanggna Khola. Interpreted minimum crystallization age in inset, uncertainty indicated by width of black box.

U-Th/Pb Geochronology Interpretations

Following Lederer et al. (2013), and Larson et al. (2017), minimum crystallization ages are interpreted as the weighted mean age of the youngest subjectively significant monazite age population subset for a specific specimen (Fig. 3.8 - 3.10). Following this procedure, the Mugu granite specimen from Ghami (GH17B), yields an interpreted minimum crystallization age of 21.58 ± 0.24 Ma, (MSWD = 0.39; Fig. 3.8).

Three specimens of the Mugu granite from the Ghar Ghompa area were dated (Fig. 3.1). Specimen GG01A has an interpreted minimum crystallization age of 21.23 ± 0.16 Ma, (MSWD = 0.84), GG10 an age of 20.30 ± 0.23 Ma (MSWD = 1.07), and GG12 an age of 20.90 ± 0.19 Ma (MSWD = 0.61). Together, these specimens yield a combined weighted mean minimum crystallization age of 20.40 ± 0.22 Ma. (Fig. 3.9).

At the Dhanggna Khola site, specimen DK14, a medium-grained to pegmatitic granite thought to be of Mustang affinity, yields a minimum crystallization age of 26.06 ± 0.30 Ma (MSWD = 1.2). Specimen DK15, from the fine-grained Mugu-affinity dike that cross-cuts the foliation of the Mustang orthogneiss, yields an age of 22.23 ± 0.37 Ma (MSWD = 0.98). Specimen DK16, collected from the orthogneiss itself, yields a minimum age of 24.92 ± 0.68 Ma (MSWD = 0.37), which is interpreted to reflect recent metamorphism. Specimens DK14 and DK16 both contain a significant older population, ranging from ∼350 to ∼500 Ma.

Monazite U-Th/Pb geochronology from all Mugu and Mustang granite specimens yield late Oligocene- early Miocene age populations, which are interpreted as crystallization ages in the granite specimens and as a metamorphic age in the gneiss specimen (Figs. 3.8 - 3.10). The older populations reported in both DK14 and DK16 from the Dhanggna Khola site (Fig. 3.10) may provide further information on these specimens. The oldest population, which ranges from 445 ± 25 Ma to 535 ± 35 Ma in specimen DK16 is interpreted to represent xenocrystic material that records the age of the igneous protolith. A similar range of ages in DK14, from 447 ± 13 Ma to 489 ± 18 Ma, is likely inherited from DK16 as a product of partial melting during metamorphism. Intermediate ages, between 109 ± 9 and 445 ± 25 Ma in specimens DK16 and DK14 may reflect partial lead-loss from the xenocrystic grains and/or sampling of multiple domains. The younger of the pre-crystallization populations, ranging from 30 ± 2 Ma to 53 ± 3 Ma and appearing in both specimens DK16 and DK14, might represent the earliest stages of Himalayan metamorphism during initial underplating and burial of the underriding Indian plate, as other authors have dated an early stage of metamorphism across in the Annapurna-Dhaulagiri region at this time. Larson and Cottle (2015) interpreted structural deformation in the Annapurna region to be coeval with metamorphism in the GHS, occurring as early as ∼48 Ma, dated by $^{232}Th/^{208}Pb$ in monazite.

The undeformed Mugu granite dike (DK15) provides the final crystallization age for the Dhanggna Khola site. Therefore, the age of this specimen was used as the upper temperature-time constraint in the cooling paths created for this site.

3.2.2 $^{40}Ar/^{39}Ar$ Thermochronology in Mica

$^{40}Ar/^{39}Ar$ Thermochronology Results

$^{40}Ar/^{39}Ar$ step-heating results are presented in Figs. 3.11 - 3.13. Calculated $^{40}Ar/^{39}Ar$ ages and closure temperatures are reported in Table 3.1. All specimens analysed returned relatively flat age spectra that define a narrow range of dates from 15.7 ± 0.1 Ma to 17.2 ± 0.1 Ma, averaging 88.0% ^{39}Ar released. $^{40}Ar/^{39}Ar$ isotopic data are detailed in Appendix C.

Table 3.1: $^{40}Ar/^{39}Ar$ plateau ages and corresponding closure temperatures.

Location	Specimen	Mineral	Plateau Age (Ma)	± 2σ	Tc (°C)	± 2σ	% ^{39}Ar released	MSWD
Ghami	GH17B	Bt	16.1	0.2	364	20	100.0	1.30
Ghar Ghompa	GG01A	Ms	17.1	0.2	507	39	81.0	0.15
	GG01B	Ms	16.9	0.2	477	46	96.2	1.30
	GG10	Ms	16.7	0.2	473	32	100.0	0.96
	GG11	Ms	16.8	0.2	487	32	97.5	0.67
	GG12	Ms	16.9	0.2	498	34	71.2	1.30
	GG13	Ms	15.7	0.2	480	38	98.3	1.12
Dhanggna Khola	DK14	Ms	17.1	0.2	535	45	59.4	0.93
	DK15	Ms	17.2	0.2	475	30	88.1	1.15

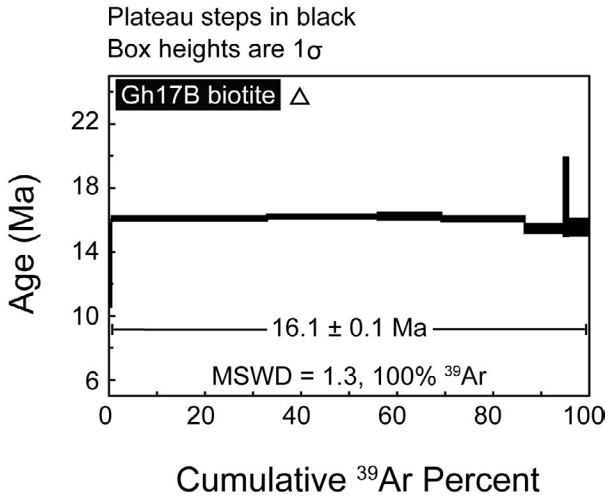

Figure 3.11: $^{40}Ar/^{39}Ar$ age spectra diagram for Ghami location. Symbol corresponds to location on Fig. 3.1.

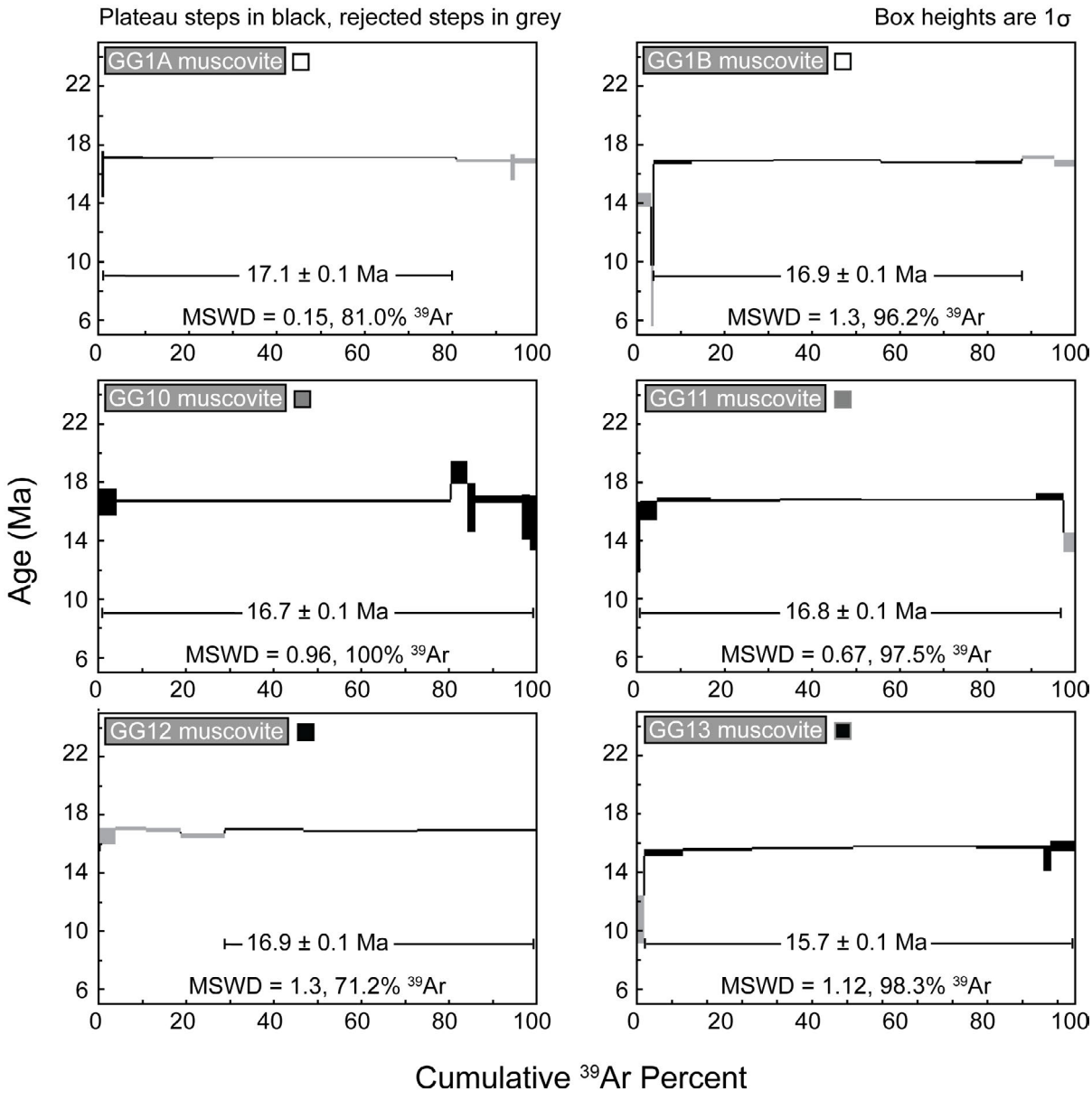

Figure 3.12: $^{40}Ar/^{39}Ar$ age spectra diagrams for Ghar Gompa site. Symbols correspond to locations on Fig. 3.1.

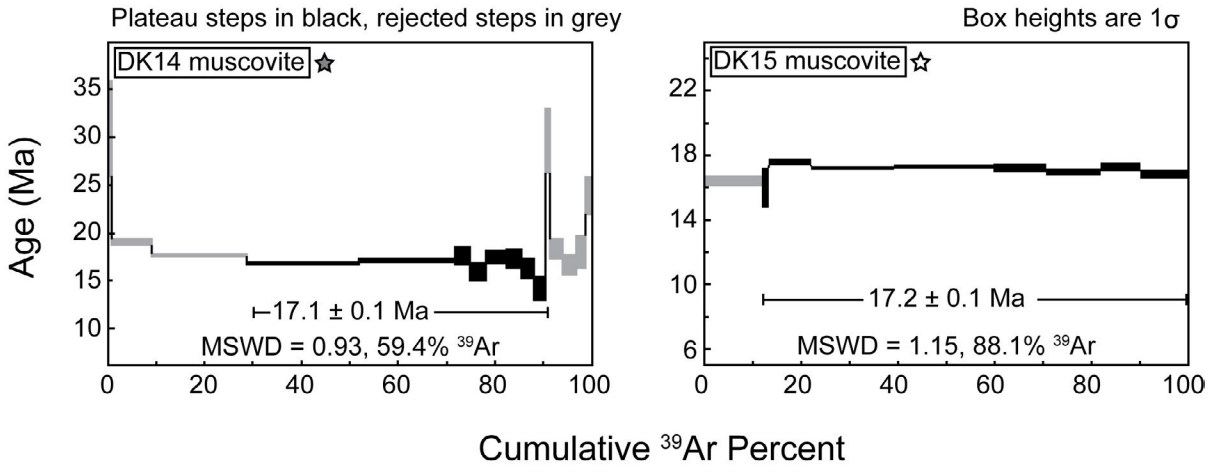

Figure 3.13: $^{40}Ar/^{39}Ar$ age spectra diagrams for Dhanggna Khola site. Symbols correspond to locations on Fig. 3.1.

^{40}Ar/^{39}Ar Thermochronology Interpretations

Since ^{40}Ar/^{39}Ar ages are consistently younger than the corresponding U-Th/Pb monazite ages, they are all interpreted as cooling ages. In each specimen, the well-defined plateau and the apparent simplicity of the cooling history precluded any need for analysis of isochron diagrams. Although the 'saddle'-shape in specimen DK14 likely indicates the presence of excess Ar at grain margins (Lanphere and Dalrymple, 1976), the good agreement in age with the other specimens from the region indicates the middle portion of the spectra yields a meaningful age.

3.2.3 U-Th/He Thermochronology in Zircon and Apatite

Zircon and Apatite U-Th/He Thermochronology Results

Calculated ages, U and Th content, effective U, and effective radii for individual zircon and apatite grains are summarized in Table 3.2. Complete elemental data for zircon and apatite U-Th/He analysis is available in Appendix C. Photographs and grain measurements of all zircon and apatite grains selected for analyses are available in Appendix B-IV and B-V.

Table 3.2: U-Th/He age, U and Th concentrations, eU, and effective radii (eR) for individual zircon and apatite grains.

Location	Specimen ID	Age (Ma)	±	Total U (ppm)	±	Total Th (ppm)	±	eU (ppm)	eR (μm)
				Zircon					
Ghami	17B-1	11.65	0.72	3591.86	32.81	93.32	8.11	3613.79	49.75
	17B-3	9.65	0.63	3164.88	44.81	90.85	0.68	3186.24	59.84
	17B-4	**10.77**	**0.64**	**2651.62**	**40.74**	**90.58**	**2.92**	**2672.90**	**43.03**
	17B-5	9.59	0.61	3444.89	34.33	141.90	2.71	3478.24	56.39
Ghar Ghompa	O1B-1	11.92	0.77	339.03	11.88	69.10	1.37	355.26	45.55
	11_3	**10.97**	**0.70**	**4336.08**	**98.61**	**77.94**	**1.81**	**4354.40**	**50.16**
Dhanggna Khola	14-2	10.65	0.67	308.07	5.74	57.72	1.66	321.63	49.20
	14-3	10.34	0.68	418.26	5.37	58.72	0.79	432.06	64.10
	14-4	14.54	0.88	1230.32	17.39	77.47	1.57	1248.52	46.02
	14-5	**13.08**	**0.84**	**829.41**	**7.38**	**96.82**	**0.71**	**852.16**	**57.08**
	14-6	14.33	0.90	704.17	6.56	73.09	2.46	721.35	53.62
				Apatite					
Ghar Ghompa	1A_1	6.10	0.10	57.76	1.28	1.99	0.04	58.22	70.95
	1A_2	5.05	0.08	148.60	3.28	17.93	0.30	152.81	67.75
	1A_3	7.32	0.13	98.99	2.19	4.55	0.08	100.06	73.22
	1A_4	7.76	0.14	89.69	1.98	3.92	0.07	90.61	89.55
	1A_5	5.59	0.09	97.55	2.15	6.78	0.12	99.14	66.67
	1A-6	6.33	0.10	120.04	2.65	4.18	0.08	121.02	61.30
	10-1	**7.35**	**0.13**	**57.93**	**1.34**	**8.91**	**0.17**	**60.03**	**42.43**
	10-2	8.78	0.16	40.38	1.02	6.43	0.33	41.89	47.78
	12_1	11.48	0.18	75.37	1.67	5.56	0.11	76.68	50.40
	12_3	9.78	0.14	136.12	3.02	6.67	0.13	137.69	40.00
	12_4	10.78	0.16	72.50	1.61	5.96	0.13	73.90	43.94
	12_5	8.73	0.14	94.19	2.10	6.00	0.11	95.60	51.73
	12-7	11.00	0.16	107.03	2.46	11.47	0.20	109.73	37.81
	12-8	8.19	0.14	89.64	2.08	7.70	0.20	91.45	37.07
	12-9	7.38	0.13	71.98	1.67	4.50	0.10	73.04	52.32
Dhanggna Khola	14_1	6.86	0.12	14.31	0.35	14.60	0.64	17.74	39.51
	14_2	7.01	0.12	11.97	0.27	13.22	0.26	15.07	39.93
	14_3	5.46	0.08	16.20	0.37	22.59	0.40	21.51	51.90
	14_4	7.47	0.11	10.24	0.23	10.21	0.35	12.64	48.72
	14_5	6.26	0.10	10.91	0.25	8.62	0.16	12.93	45.62
	14_6	4.80	0.06	13.55	0.30	18.98	0.33	18.01	54.67
	15-1	7.12	0.11	65.19	1.54	25.76	0.48	71.25	36.37
	15-2	**4.84**	**0.09**	**65.77**	**1.52**	**29.17**	**0.45**	**72.63**	**44.84**
	15-3	4.44	0.07	142.50	3.28	90.75	1.40	163.83	45.26
	15-4	5.23	0.12	44.38	1.03	21.39	0.36	49.40	42.26
	15-5	3.46	0.05	151.40	3.51	50.59	0.77	163.28	45.56

Zircon U-Th/He Thermochronology Interpretations

Since all U-Th/He ages are younger than their corresponding $^{40}Ar/^{39}Ar$ ages, they are considered valid cooling ages. Zircon and apatite U-Th/He thermochronologic analyses yield overdispersed cooling ages, therefore, to aid in interpretation, grain data have been plotted using both isochron (Vermeesch, 2008) and logratio plots (Vermeesch, 2010). Where available, the central age (bold text in Figs. 3.14 - 3.18) is the preferred age for such overdispersed data. In general, the central age method will provide greater confidence in any geological interpretation based on the data, as it is a more accurate representation of the true age than is an arithmetic mean (Vermeesch, 2008). An exception to this is the zircon cooling data from the Ghami location, where only 2 crystals yield successful analyses, and the preferred age is thus the geometric mean. Ellipse colouring in the logratio plots (Figs. 3.14 - 3.18) indicates the effective uranium (eU = U + 0.235∗Th in ppm) concentration in each crystal, allowing for a qualitative check for possible age bias due to alpha-ejection track concentrations (Shuster et al., 2006). The isochron diagrams show a 'pooled age' (red line, Figs. 3.14 - 3.18) of all successful crystals from that location (Vermeesch, 2008).

Zircons GH17-2, GH17-6, and GG14-1 were lost during the isotope dilution process. In addition, zircons GG01B-3, GG11-1 and GG11-2 released negligible He, and thus gave no meaningful results. These three grains yielded a reasonable amount of U and Th during chemistry and, therefore, the problem must solely lie with He data collection. The most likely cause of this failure is an error in the sequence in which the laser fired, resulting in the laser reheating an already degassed crystal, or moving to a hot-blank instead of a new packet location. The remaining successful zircons were numerous enough to obtain meaningful age data from each location.

Four successful zircon crystals from the Mugu granite dike (GH17B) at the Ghami site define a central age of 10.31 ± 1.78 Ma, and an isochron age of 18.3 ± 1.2 Ma (Fig. 3.14). The y-intercept of the 'pooled age' line (Vermeesch, 2008) on the isochron diagram of -139 ± 21 is far from the expected value of 0, which indicates that the age obtained by the isochron method is unreliable. The central age from the logratio plot is the preferred age for this location and is more reasonable given the 16.1 ± 0.1 Ma muscovite $^{40}Ar/^{39}Ar$ age from the same specimen. The random arrangement of eU concentration in Fig. 3.14 indicates no age bias for the Ghami zircon specimens.

Two zircons picked from Ghar Ghompa Mugu granite (grains GG01B-1 and GG11-3) yielded successful and reasonable U-Th/He ages. Ages from the logratio and isochron plots are in agreement within error (Fig. 3.15), at 11.27 ± 0.32 and 10.81 ± 0.27 Ma, respectively. The isochron age may be reliable, as indicated by the y-intercept value of 2.0 ± 0.9, however, this method is strongly affected by the low number of data. As there are only two crystals, The Helioplot program cannot calculate a central age on the logratio plot, so instead a geometric mean is used as the preferred zircon U-Th/He age at this location. The lack of data from this

location also precludes any useful interpretation of age bias in the logratio plot based on eU concentrations. Zircon GG01B-2 yields an anomalously old U-Th/He age of 43.57 ± 3.58 Ma before alpha-ejection correction, and is thus discarded as it indicates a cooling age greater than the crystallization age from the same specimen.

Five zircons from from the Dhanggna Khola pegmatitic Mustang granite (specimen DK14) were analyzed. The central age (12.39 ± 3.76 Ma) and isochron age (16.31 ± 0.21 Ma) marginally overlap within uncertainty, however, the isochron age is interpreted as less reliable due to the low y-intercept value of -11.8 ± 0.7, thus the central age is again the preferred age for this location (Fig. 3.16). Ellipse colouring indicates no clear age bias based on eU concentration.

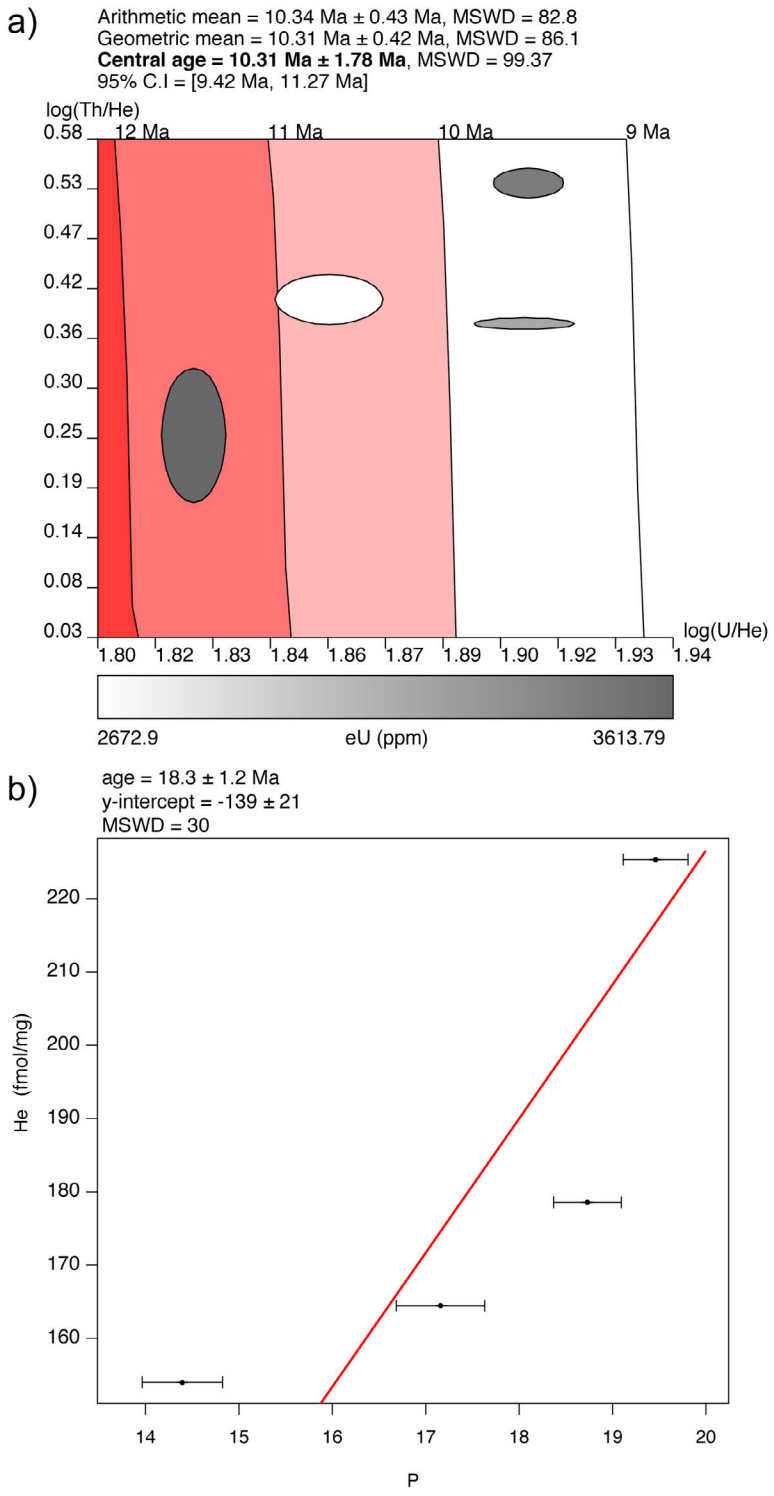

Figure 3.14: Zircon U-Th/He dates from Ghami site. A) Logratio plot. Ellipses indicate individual ages and associated errors. Ellipse colouring indicates eU content. Preferred age in bold type. B) Isochron diagram. Y axis P value is a function of U and Th concentration (Vermeesch, 2008).

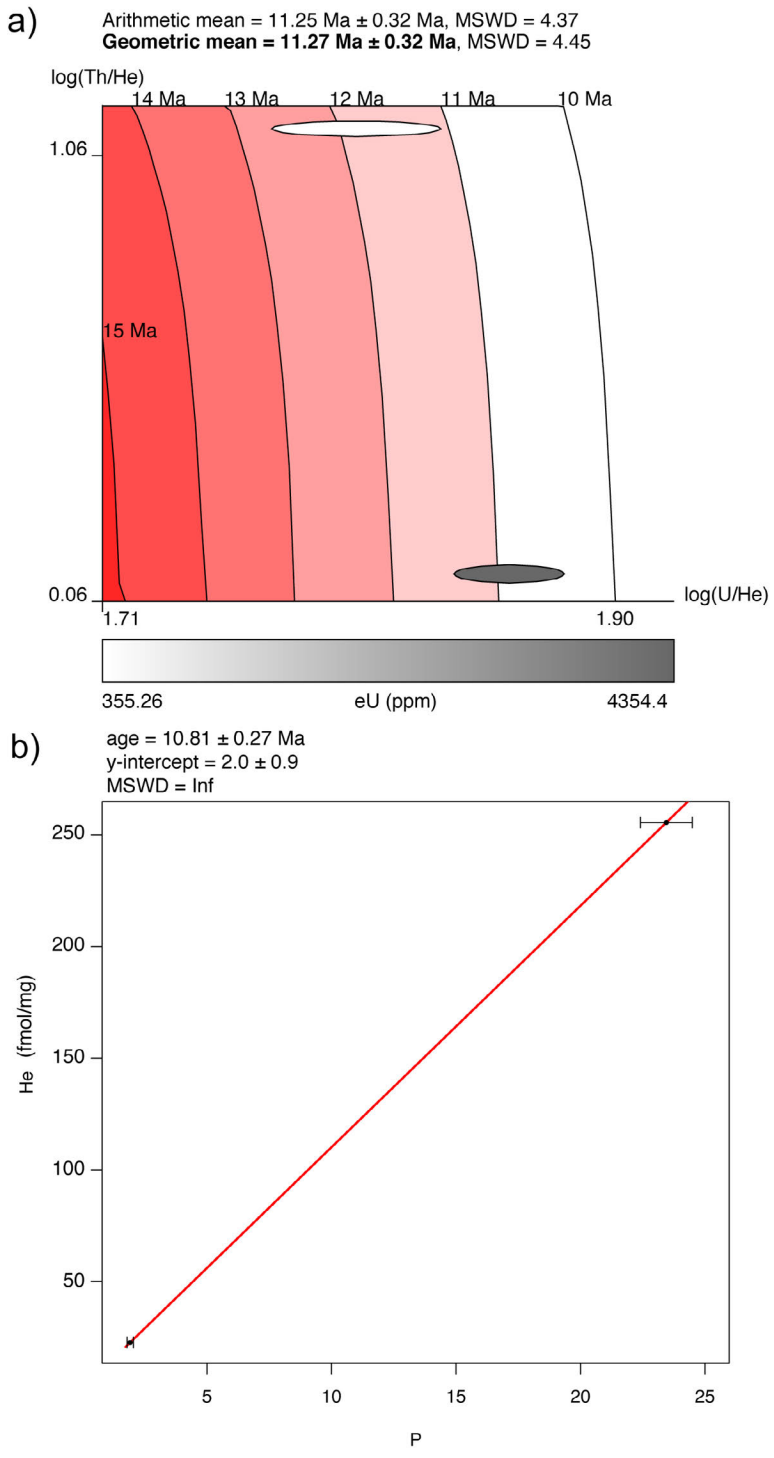

Figure 3.15: Zircon U-Th/He dates from Ghar Gompa site. A) Logratio plot. Ellipses indicate individual ages and associated errors.Ellipse colouring indicates eU content. Preferred age in bold type. B) Isochron diagram. Y axis P value is a function of U and Th concentration (Vermeesch, 2008).

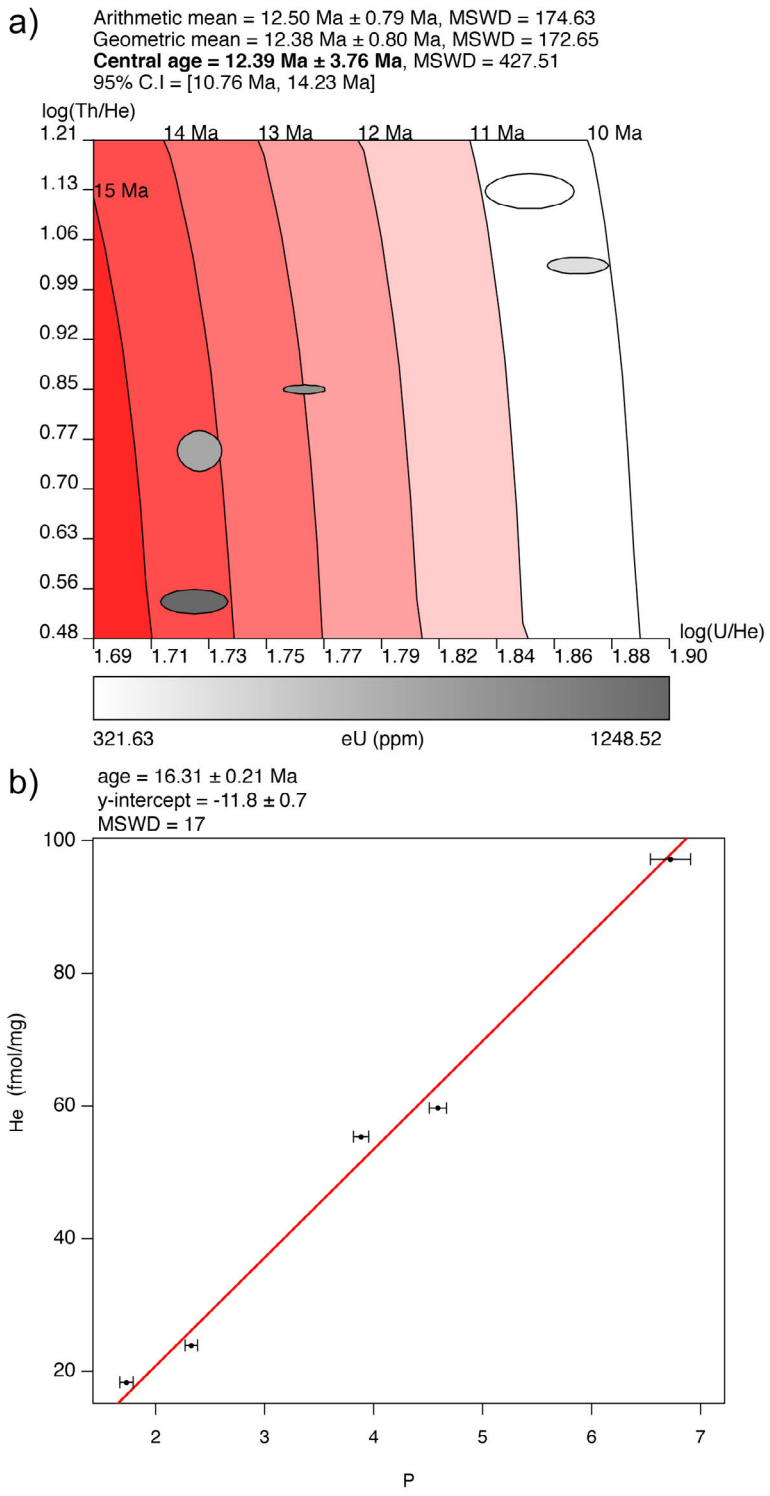

Figure 3.16: Zircon U-Th/He dates from Dhanggna Khola site. A) Logratio plot. Ellipses indicate individual ages and associated errors. Ellipse colouring indicates eU content. Preferred age in bold type. B) Isochron diagram. Y axis P value is a function of U and Th concentration (Vermeesch, 2008).

Apatite U-Th/He Thermochronology Interpretations

The specimen of the dike (GH17B) collected from the Ghami site contained no useable apatite crystals.

Apatites GG12-2 and GG12-6, retrieved from the Ghar Ghompa specimen GG12, released negligible He, leading to a geologically meaningless 0 Ma age. Apatite GG12-2 also yielded low U and Th concentrations, 2 or more orders of magnitude lower than crystals that gave geologically reasonable ages, indicating perhaps that this was a non-U-bearing mineral picked by mistake. The lack of complete terminations and otherwise poorly defined crystal shape of GG12-2 are consistent with that interpretation (Appendix B-IV). Apatite GG12-6, however, contained U and Th concentrations in a similar range to the successful crystals. This latter situation would be consistent with a crystal that fell out of the Nb packet, preventing from proper degassing, but that remained in the vial so was still dissolved during digestions. A more likely possibility is that an error was made when preparing the laser sequence, and instead of visiting the desired crystal site, the laser instead re-fired on an already degassed packet, or a hot blank, and hence returned no He. The 15 analyses that yield reasonable ages from all granite specimens containing useable apatites from the Ghar Ghompa site (specimens GG01A, GG10, and GG12) are combined into logratio and isochron diagrams (Fig. 3.17). The central age (7.84 ± 1.25 Ma) and the isochron age (11.91 ± 0.26 Ma) do not overlap within uncertainty, and due to the non-zero y-intercept value of -1.53 ± 0.11 and the loose grouping of ages around the pooled age line in the isochron diagram, the central age is the preferred apatite U-Th/He age for this location. Ellipse colouring reveals no age bias based on eU content of the crystals analyzed.

Eleven successful apatite ages were obtained from granite specimens DK14 and DK15 from the Dhanggna Khola site. They yield overlapping central and isochron ages at 5.63 ± 0.78 and 5.04 ± 0.06 Ma, respectively. Despite the very good fit on the isochron diagram (y-intercept 0.10 ± 0.01), the central age is again taken as the preferred age at this location due to the more conservative error calculated by this method (Fig 3.18). There is no apparent correlation between eU and age at this location. Apatite DK15-6 yields an anomalously old U-Th/He age of 25.9 ± 0.58 Ma before alpha-ejection corrections. This age is discarded because it is unreasonable to expect an apatite cooling age greater than the crystallization age from the same specimen.

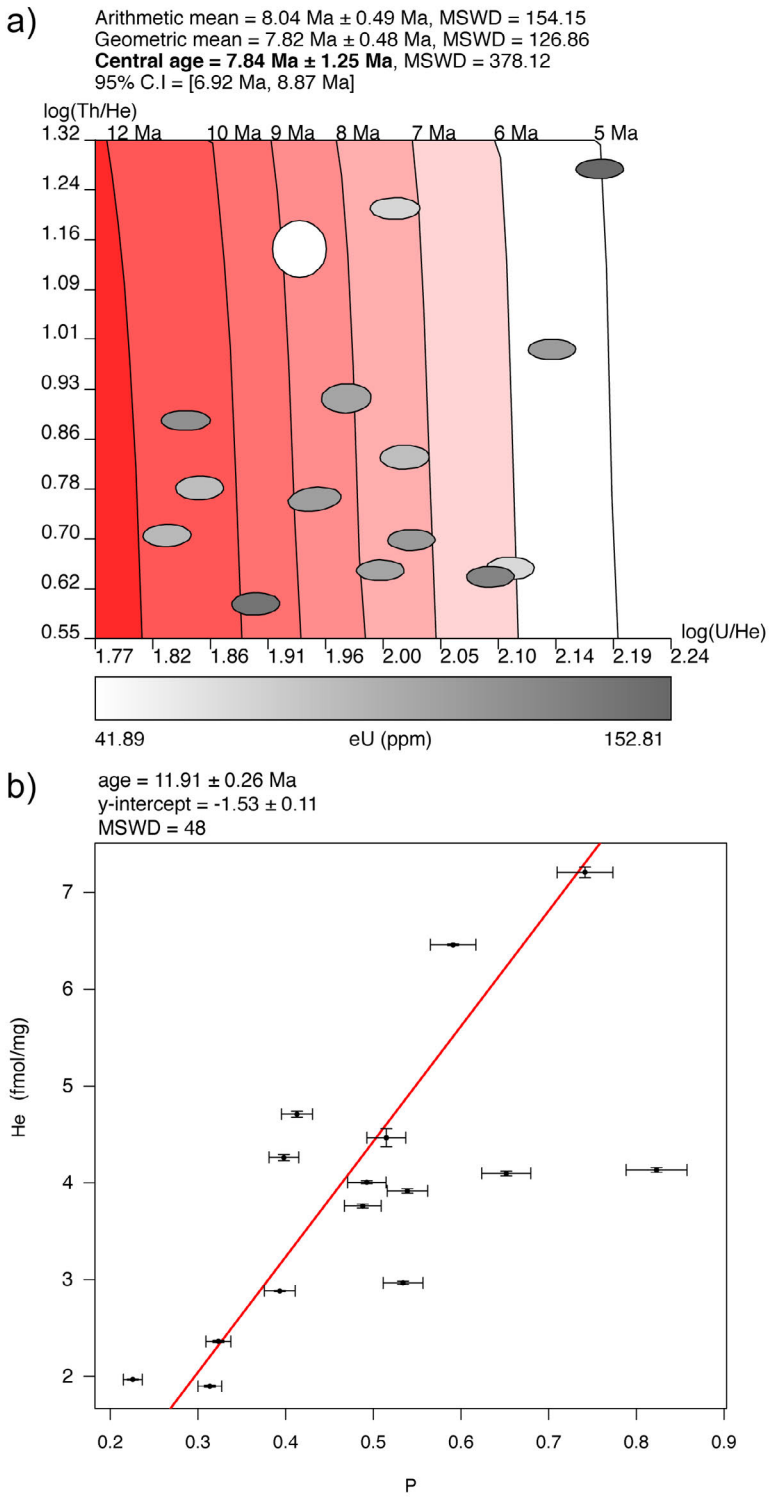

Figure 3.17: Apatite U-Th/He dates from Ghar Gompa site. A) Logratio plot. Ellipses indicate individual ages and associated errors. Ellipse colouring indicates eU content. Preferred age in bold type. B) Isochron diagram. Y-axis P value is a function of U and Th concentration (Vermeesch, 2008).

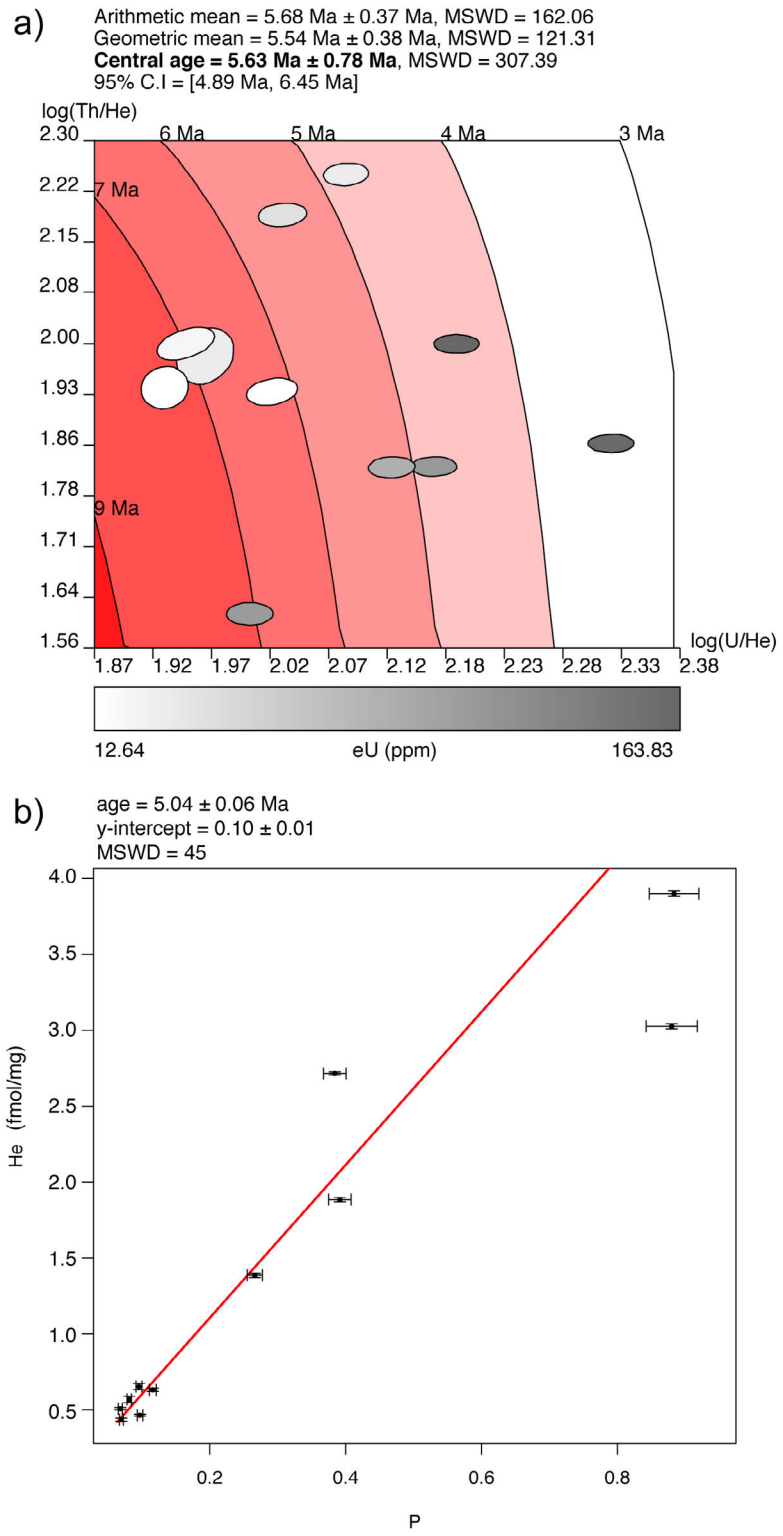

Figure 3.18: Apatite U-Th/He dates from Dhanggna Khola site. A) Logratio plot. Ellipses indicate individual ages and associated errors. Ellipse colouring indicates eU concentration. Preferred age in bold type. B) Isochron diagram. Y-axis P value is a function of U and Th concentration (Vermeesch, 2008).

3.2.4 Summary of Geochronologic Constraints

A summary of radiometric ages is presented in Figure 3.19. This diagram includes all apatite, zircon, muscovite, and biotite cooling ages from this study, as well as the subset of monazite ages that were selected to represent the minimum crystallization age for each Mugu batholith-related specimen. As the Mustang orthogneiss and granite specimens (DK16 and DK14, respectively) are significantly older than the cross cutting Mugu dike at the Dhanggna Khola location (DK15), their monazite ages are not considered representative of the final crystallization in that area and hence are not included in the figure.

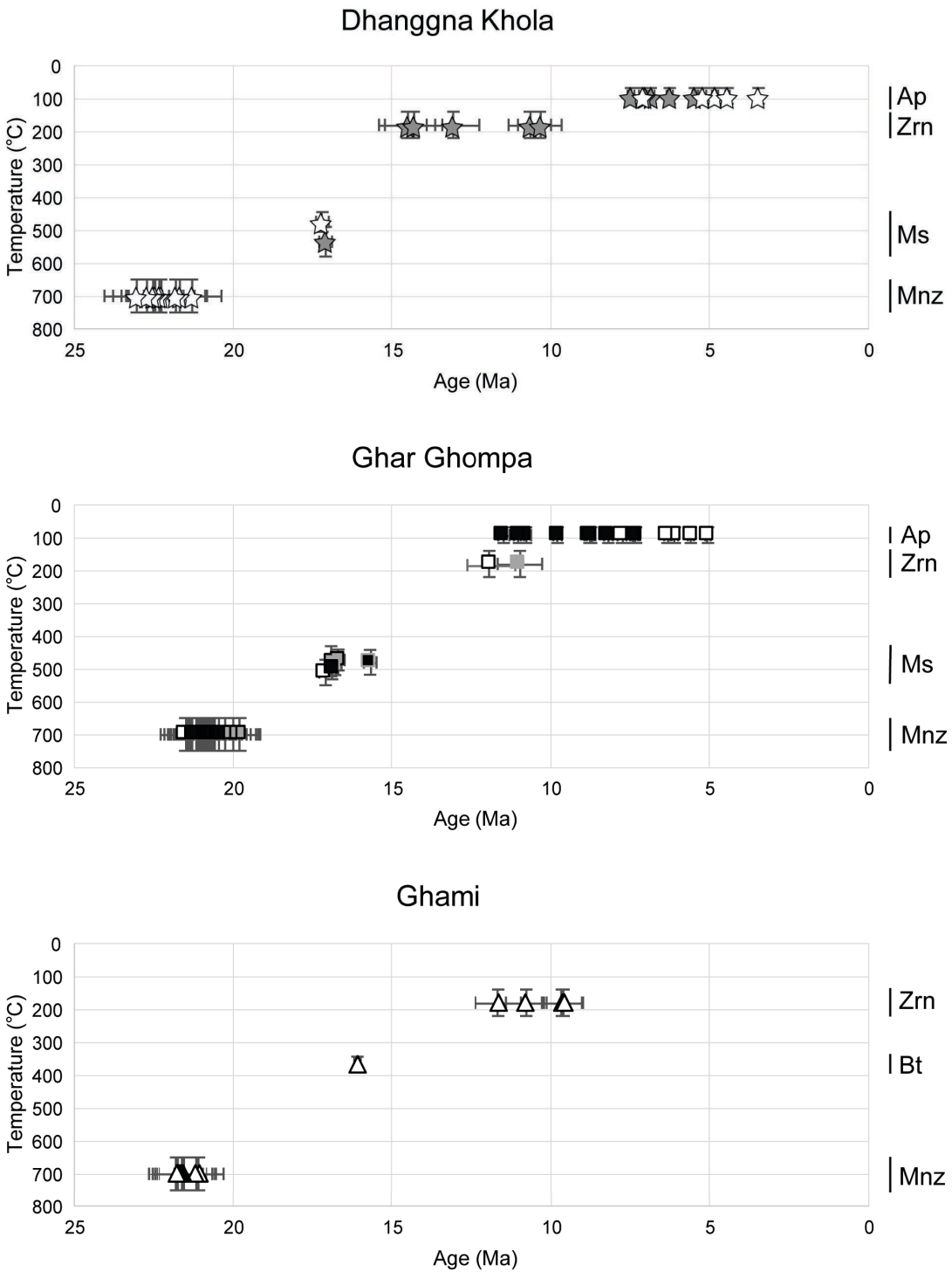

Figure 3.19: Age summary diagram. Symbols and colours correspond to sampling locations (Fig. 3.1). Mineral systems indicated by bars on right axis. Only monazite analyses used for minimum crystallization age determination shown. All other mineral specimens plotted. Error bars are 2σ.

3.3 Cooling Paths

Three cooling path diagrams (Fig. 3.20 - 3.22) were created using the thermal modelling software HeFTy (Ketcham, 2005), one for each location previously detailed. These models are used to interpret the combined thermochronology data presented in the previous sections.

Temperatures used for the thermal constraints include 700 ± 50 °C for U-Th/Pb ages, based on typical crystallization temperatures for Himalayan leucogranites (Copeland et al., 1990; Ayres and Harris, 1997; Visonà and Lombardo, 2002) and calculated closure temperatures for the mica used in a particular model (Table 3.1). HeFTy requires grain-specific U-Th/He input data for zircon and apatite in order to calculate cooling paths that are compatible with alpha ejection and radiation damage modelling (Shuster et al., 2006; Flowers et al., 2009; Guenthner et al., 2013). These factors are based on grain size and eU, hence individual grains were selected to represent each location. The zircon and apatite grains that had an U-Th/He age closest to the central age from their respective sites were chosen to represent each location. These grains are bolded in Table 3.2. The lowest temperature thermal constraint used in HeFTy was estimated at 10 ± 10 °C based on multiple modern-day yearly averages for the Upper Mustang region. Cooling rates are estimated between the weighted mean path inflection points on the cooling path diagrams, by averaging the highest and lowest straight-line slopes that are entirely within the 'good' (pink) path envelope between the two constraint boxes.

The cooling path from Ghami (Fig. 3.20) was created using the crystallization age for this location (Fig. 3.8), the biotite $^{40}Ar/^{39}Ar$ age and associated closure temperature from specimen GG17B (Table 3.1), and zircon data from grain GH17B-4 (Table 3.2), as its individual age was closest to the central age for the specimen. This location has no apatite data, which is the main contributor to the wide range of 'good' and 'acceptable' paths found during modelling. At this location there is a steady decrease in cooling rate with time, most notable in the slope changes of the weighted mean path (bold blue line). The cooling rate from 22 Ma to 16 Ma is 61.3 ± 10.0 °C/Ma, decreasing to an indistinguishably lower rate of 37.5 ± 18.2 °C/Ma from 16 Ma to 10 Ma, and again to a distinctly lower rate of 15.7 ± 1.1 °C/Ma from 10 Ma to present.

The cooling path for Ghar Ghompa (Fig. 3.21) was created using the crystallization age of specimen GG10 (Fig. 3.9), the muscovite $^{40}Ar/^{39}Ar$ age and associated closure temperature of specimen GG11, the zircon data from grain GG11-3, and apatite data from grain GG10-1. The initial cooling rate at this location is 61 ± 18 °C/Ma from 20 Ma to 17 Ma, which changes to an indistinguishably lower rate of 51.1 ± 9.6 °C/Ma from 17 Ma to 9 Ma. This rate further decreases after the zircon U-Th/He constraint to 22.3 ± 13.0 °C/Ma from 9 to 6.5 Ma, and again to 4.4 ± 4.4 °C/Ma from 6.5 Ma to present.

The cooling path for Dhanggna Khola (Fig. 3.22) was created using the minimum crystallization age for that location (DK15; Fig. 3.10), the muscovite $^{40}Ar/^{39}Ar$ age and associated closure temperature of specimen GG15, the zircon data from grain GG14-5, and apatite data

from grain GG15-2 (Table 3.2). The initial cooling rate at this location is 45 ± 11 °C/Ma from 22 Ma to 17 Ma, increasing indistinguishably within error to 74.9 ± 19.6 °C/Ma from 17 Ma to 12 Ma, then decreasing to 13.0 ± 4.4 °C/Ma from 12 Ma to 7 Ma, and decreasing again to an indistinguishable rate of 6.7 ± 0.8 °C/Ma from 7 Ma to present.

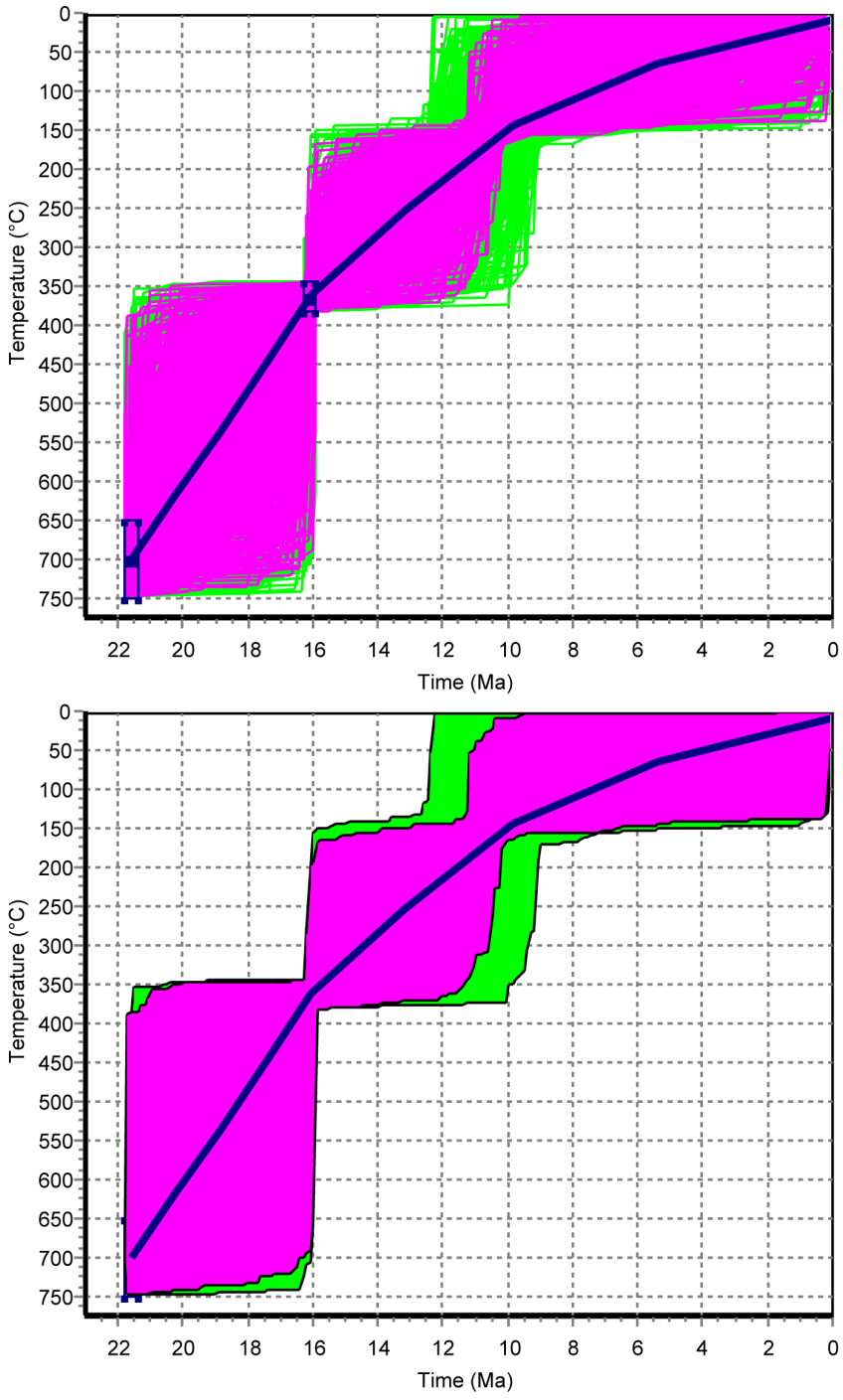

Figure 3.20: HeFTy-derived cooling paths of specimens from Ghami site. Bold line is weighted mean path. (Upper) Pink paths are considered 'good', green 'acceptable'. (Lower) Envelopes surrounding all 'good' and 'acceptable' paths.

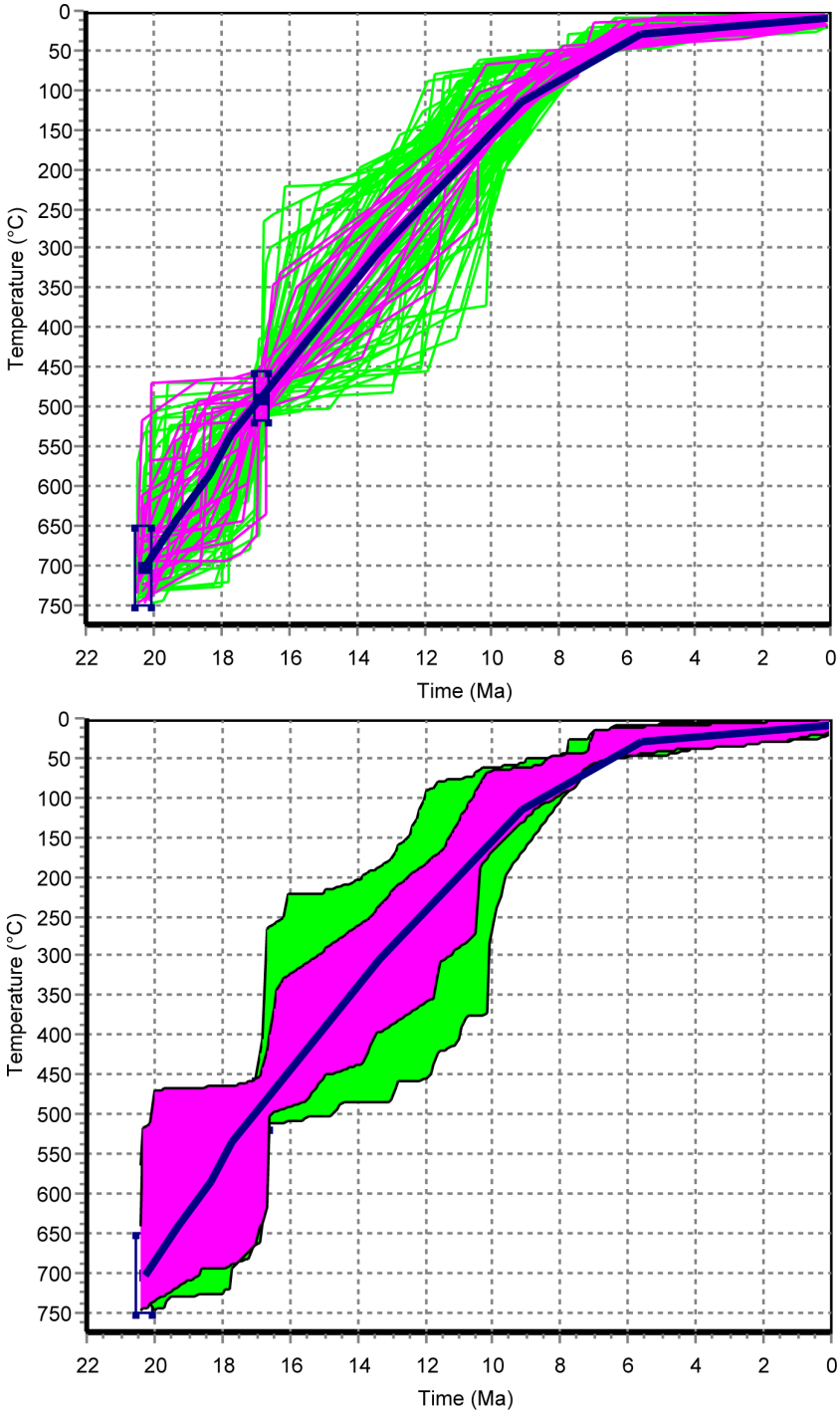

Figure 3.21: HeFTy-derived cooling paths of specimens from Ghar Ghompa site. Bold line is weighted mean path. (Upper) Pink paths are considered 'good', green 'acceptable'. (Lower) Envelopes surrounding all 'good' and 'acceptable' paths.

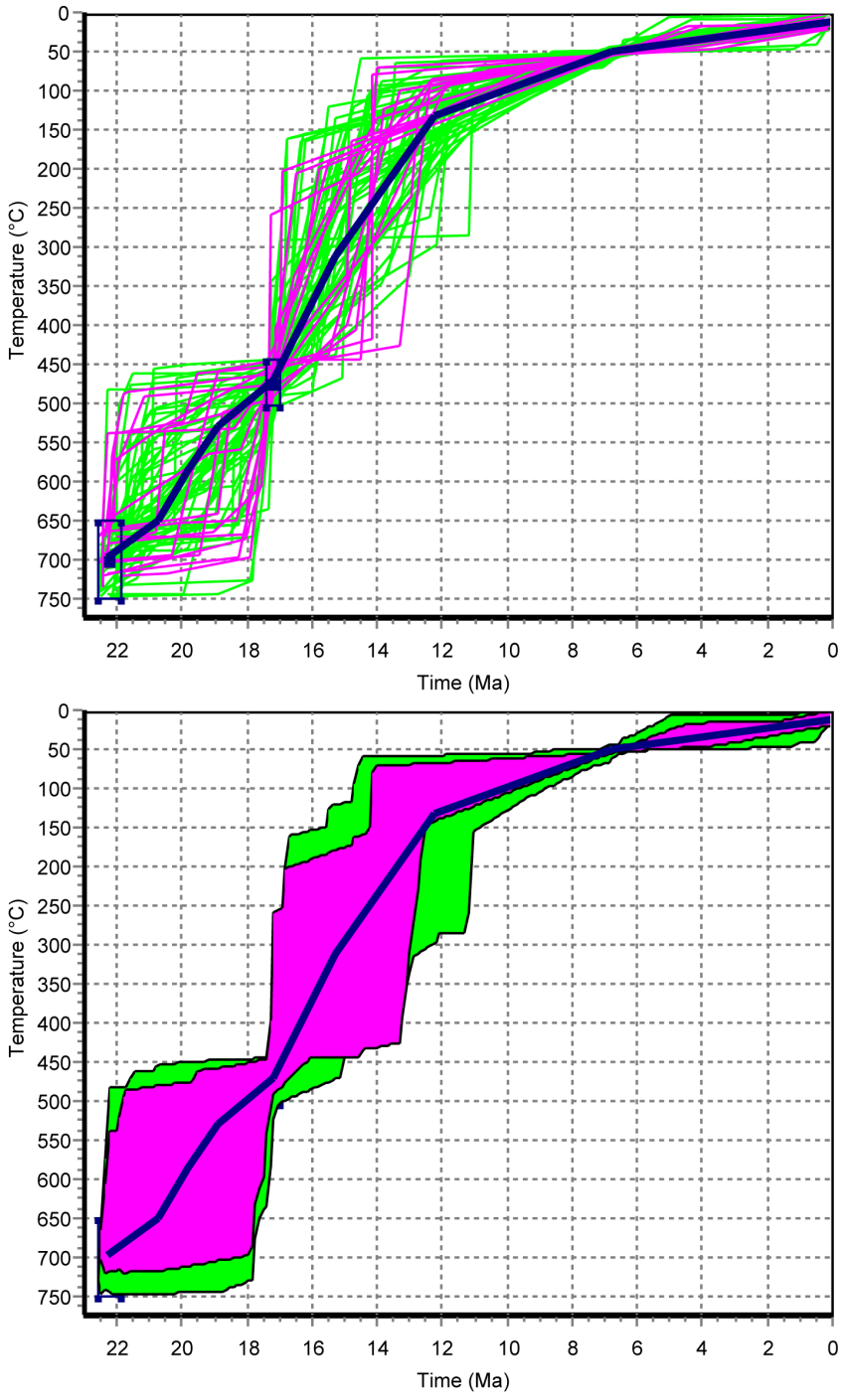

Figure 3.22: HeFTy-derived cooling paths of specimens from Dhanggna Khola site. Bold line is weighted mean path. (Upper) Pink paths are considered 'good', green 'acceptable'. (Lower) Envelopes surrounding all 'good' and 'acceptable' paths.

Chapter 4

Discussion and Conclusions

4.1 E-W extension in the Thakkhola graben

The initiation of brittle E-W extension related to the Thakkhola graben was previously estimated to be ∼14 Ma (Coleman and Hodges, 1995), based on dating of hydrothermal muscovite in a ∼N-S striking, vertical brittle structure, ∼40 km east of the Dangardzong fault. Garzione et al. (2000) later dated the Tetang formation of the Thakkhola graben using magnetic polarity measurements and sedimentation rates, and determined that the oldest sediments in the graben were between ∼11 and ∼9.6 Ma.

Preliminary microstructural data from the metamorphosed TSS at the margin of the Mugu batholith in the Ghar Ghompa area (Fig. 3.1) shows ductile, top-to-the-east sense shear (Larson et al., Prep). Moreover, quartz c-axis-derived deformation temperatures from the same rocks overlap muscovite closure temperatures calculated in this thesis (Larson et al., Prep), including that of specimen GG10 (473 ± 32 °C; Table. 3.1), which is spatially the closest granite specimen to the metamorphic specimens used for quartz fabric analysis. These data indicate that ductile E-W extension in the region was ongoing by at least 16.7 ± 0.2 Ma.

Other regions of the Himalaya and Tibet also record the initiation of E-W extension in the early Miocene. Cooper et al. (2015) document that E-W extension in the Yadong Cross structure (YCS) was ongoing by ∼14 Ma (Fig. 4.1a), Mitsuishi et al. (2012) interpreted ductile E-W extension to have initiated with granite emplacement at ∼19 Ma in the Kung Co area of southern Tibet, and Murphy and Copeland (2005) provided evidence of E-W extension contemporaneos with N-S shortening in the Gurla Mandhata, and date movement on structures that accommodate the E-W component to ≤15 Ma (Fig. 4.1a). Moreover, in NW India, Thiede et al. (2006) interpret rapid exhumation of the Leo-Pagril dome beginning at ca. 16 Ma to reflect the initiation of E-W extension. While some have argued against these previous estimates of a mid-Miocene age of E-W extension in the Himalaya and Tibet, due to the ambiguous relationship between N-S striking dikes and veins that have been dated, which may also be caused by N-S compression (e.g. Mahéo et al., 2007), the new data from this work explicitly dates E-W extension in the Thakkhola region to a minimum of 16.7 ± 0.2 Ma.

In addition to providing information on the initiation of the Thakkhola graben, this study also presents the first low temperature (zircon and apatite U-Th/He) cooling constraints from the Upper Mustang region. These new data, along with the $^{40}Ar/^{39}Ar$ and U-Th/Pb ages

presented, facilitate the computation of complete cooling paths previously only possible between higher temperature ($^{40}Ar/^{39}Ar$ and U-Th/Pb) constraints (e.g. Hurtado, 2002; Vannay and Hodges, 1996). The cooling paths developed can be used as a proxy to investigate the exhumation of the region if cooling is assumed to be driven by exhumation.

Since movement on the STDS in the Annapurna/Mustang region had ceased by ∼22 Ma (Godin et al., 2001), cooling rates determined in this study are inferred to relate directly to exhumation driven by E-W extension. The cooling rates calculated at the three locations in this study (Ghami, Ghar Ghompa, Dhanggna Khola; Fig. 3.1) are steady from ∼22 to ∼13 Ma, which is demonstrated by the indistinguishable slopes in the monazite-to-mica (55 ± 7 °C/Ma average) and mica-to-zircon (58 ± 9 °C/Ma average) sections of the cooling paths (Figs. 3.20 - 3.22, 4.1a). A distinct change in cooling rates at all three field locations between ∼13 and ∼8 Ma (16 ± 1 °C/Ma average) marks a slowing in the cooling rate and likely related E-W extension at that time (Figs. 3.20 - 3.22, 4.1b). This slower cooling rate could be linked to 1) the initiation of brittle extension within the Thakkhola graben, or 2) the initiation of extensional structures elsewhere in the Himalaya and the Tibetan plateau that accommodate E-W extension, partitioning deformation away from Thakkhola region at this time.

The age of the oldest sediments found in the Thakkhola graben are between ∼11 and ∼9.6 Ma (Garzione et al., 2003). If these sediments are truly the first deposited in the graben, there is a possibility that brittle E-W extension in the region only began at this time. However, the rapid cooling rates from ∼22 Ma to ∼13 Ma (Figs. 3.20 - 3.22) suggest tectonic exhumation was already active at this time, and although the oldest exposed sediments preserved are from ∼11 Ma, they may not be the oldest sediments generated during graben formation.

The second possibility is that the change in cooling rate in the Thakkhola graben is due to initiation of E-W extension structures elsewhere in the Himalaya and Tibetan plateau. The initiation of graben structures in southern Tibet is shown in Figure 4.1 and summarized in Table 4.1. Eleven studies document the regional initiation of ductile and brittle E-W extensional structures at ∼13-8 Ma (Table 4.1) at 8 different locations (Fig. 4.1b). Another 4 studies document a second period of extension in brittle structures from the same locations at ∼6-4 Ma (Table. 4.1; Fig. 4.1c). The development of extensional graben in the plateau increases through time with some evidence for progressive south-to-north development (Fig. 4.1).

Previous authors have recognized a multi-stage history for the development of E-W extension in Tibet. Kali et al. (2010) recognize a period of ductile E-W extension in the Ama Drime region at ∼12 Ma, and a later initiation of related brittle extension in the same area at ∼6-4 Ma (Table 4.1). Northwest of the Kung Co rift, in the Tangra Yum Co rift (Fig. 4.1b), Dewane et al. (2006) outline two periods of E-W extension based on cooling path inflections at ∼13 Ma and ∼6 Ma. Ratschbacher et al. (2011) provide a summary of rifting in southern Tibet and show that early ductile E-W extensional structures consistently initiate at ∼13-8 Ma, coincident with a decrease in the cooling rate of the Thakkhola graben, while a second population of brittle E-W structures

initiate around ∼4-5 Ma, the same time as the second inflection point in the Thakkhola cooling curves (Figs. 3.20 - 3.22).

There is, thus, regional evidence that the inflection points in the cooling history of the Dangardzong footwall in this study (∼13-8 Ma and ∼5 Ma; Figs. 3.20 - 3.22) are related to the progressive initiation of E-W extension elsewhere in the Himalaya and Tibetan plateau. Although it is not possible to uniquely identify the source of the shift of cooling rate in the Thakkhola graben from the data presented herein, the inflection points at ∼13-8 Ma and ∼5 Ma (Figs. 3.20 - 3.22) add to a growing body of evidence consistent with a major shift in orogen-wide kinematics took place at this time (e.g. Cottle et al., 2009; Leloup et al., 2010; Zhang and Guo, 2007).

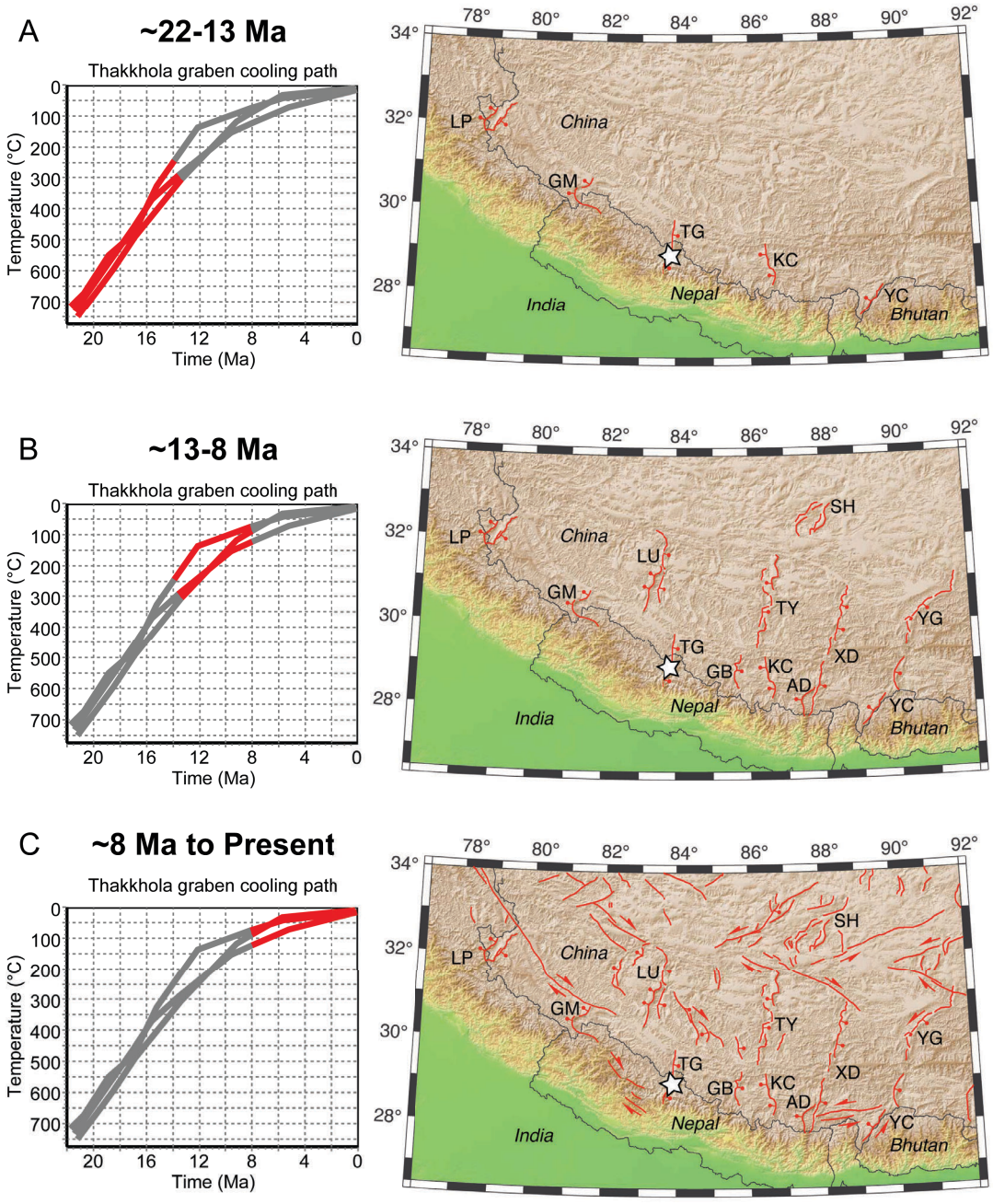

Figure 4.1: Cooling paths (this study) and E-W extensional structures (modified from Styron et al., 2011). Study area is indicated by the star. Left: weighted mean cooling paths for the three field locations from this study, with time period of interest highlighted in red. Right: map of the Himalaya and Tibetan plateau indicating E-W extensional structures active in different time periods (red lines). Abbreviations: AD - Ama Drime massif, GB - Gyirong basin, GM - Gurla Mandhata dome, LP - Leo Pagril dome, LU - Lunggar rift, SH - Shuang Hu graben, TG - Thakkhola graben, TY - Tangra-Yumco rift, XD - Xainza-Dinggye rift, YC - Yadong Cross structure, YG - Yadong-Gulu rift.

Table 4.1: Location and age of various N-S trending brittle and ductile structures in the Himalaya and Tibetan plateau.

Location (Fig. 8)	Age (Ma)	Structure	Rheology	Reference
YC	< 14	Lingshi normal fault	brittle	Cooper et al., 2015
YG	≤ 11.5	Yadong graben	ductile	Ratschbacher et al., 2011
YG	8 ± 1	Nyainqentanghla shear zone	ductile	Harrison et al., 1995
XD	ca. 8-13	Dinggye normal fault	brittle	Zhang and Guo, 2007
AD	≥ 11	Dinggye normal fault	brittle	Leloup et al., 2010
AD	12 ± 1	Dinggye and Kharta shear zones	ductile	Kali et al., 2010
AD	12 ± 1	Nyönno Ri detachment	ductile	Langille et al., 2010
KC	ca. 12-13	Kung Co rift	brittle	Lee et al., 2011
TY	ca. 13	Tangra-Yumco rift	n/a	Dewane et al., 2006
GB	≥ 11	Gyirong basin	brittle	Xu et al., 2012
SH	≥ 13.5	Shuang Hu graben	brittle	Blisniuk et al., 2001
LU	ca. 8	Lunggar Rift	brittle	Styron et al., 2013
YG	ca. 5	Ringbung graben	brittle	Ratschbacher et al., 2011
YG	ca. 5	Nyainqentanghla shear zone	brittle	Harrison et al., 1995
YG	ca. 5-7	Gulu rift	brittle	Stockli et al., 2002
AD	ca. 6-4	Dinggye normal fault	brittle	Kali et al., 2010
TY	ca. 6	Tangra-Yumco rift	brittle	Dewane et al., 2006

4.2 Potential sources of kinematic shift

While there is considerable variation in the timing of movement on the STDS along the Himalaya (e.g. Cottle et al., 2007) at most locations in the western Himalaya movement had ceased by at least 19 Ma (Liu et al., 2017). The STDS in the Annapurna-Dhaulagiri Himalaya, a region which extends over the southern extent of the Thakkhola graben, has been studied in detail and is believed to have ceased by ∼22 Ma (Godin et al., 2001). Locations in the eastern Himalaya show a much younger cessation of movement on the STDS, perhaps as young as ∼11-13 Ma at Wagye La and Khula Kangri (Edwards and Harrison, 1997; Kellett et al., 2009; Wu et al., 1998). While the cessation of movement on the STDS in the Mustang region (Annapurna-Dhaulagiri) predates an approximately linear cooling rate between the monazite U-Th/Pb and zircon U-Th/He constraints (this study, Figs. 3.20 - 3.22), the end of STDS movement farther east in the Himalaya is contemporaneous with the inflection point on the same cooling curves between ∼13 and ∼8 Ma (Edwards and Harrison, 1997; Kellett et al., 2009; Wu et al., 1998), and with the initiation of numerous E-W extensional structures throughout the Himalaya and the Tibetan plateau discussed above.

Several authors have recognized a major kinematic shift in the Himalaya during middle Miocene, however, the cause of this shift is unknown. There is a transition in S-directed thrusting at this time, moving from the MCT farther into the farland and the MBT (e.g. Meigs et al., 1995), which is believed to be linked to increased intensity of the Asian monsoon (Sun and Wang, 2005) and Himalayan erosion (Clift et al., 2008). In addition, Cottle et al. (2009) suggest activity on the faults bounding the Ama Drime massif in the middle Miocene reflect a shift from S-directed to orogen parallel mid-crustal flow. That is compatible with data from Zhang et al. (2004) who document present-day eastward 'escape' of crustal material in eastern Tibet via global positioning system data, the initiation of which has been dated to ∼15-10 Ma (Kirby et al., 2002). Some authors further interpret the current eastward movement of surface material to reflect partial coupling with an eastward flowing lower-crust (Clark and Royden, 2000; Royden et al., 1997). Finally, Leloup et al. (2010) suggest a link between cessation of movement on the STDS, the transition of thrusting from the MCT to the MBT, the initiation of E-W dominated extension, and a change in convergence direction and rate between India and Asia. Large scale tectonic movements such as a change in convergence rate or direction could trigger a multitude of complex kinematic adjustments within an orogen. While the exact cause and effect relationships of the above phenomena are unknown, the temporal similarity between them are suggestive of a genetic link. Further work is required to parse exactly what the dominant driving forces may be.

4.3 Conclusions

This study presents the first low-temperature (U-Th/He) constraints for the Thakkhola graben, and together with $^{40}Ar/^{39}Ar$ dating of muscovite and biotite, and U-Th/Pb dating of monazite, outline a detailed cooling history in the footwall of the Dangardzong fault. Cooling rates in the footwall show rapid cooling from ∼22 Ma to ∼13 Ma, and two inflection points indicating a decrease in cooling rate at ∼13-8 Ma and again at ∼5 Ma (Figs. 3.20 - 3.22). These inflection points are interpreted to correspond to decreases in E-W extension-driven exhumation in the Thakkhola graben at these times, which may be related to the initiation of E-W extensional structures elsewhere in the orogen that partition strain away from the graben (Fig. 4.1). The development of such structures coincides with significant changes in the regional kinematics of the orogen.

4.4 Future Work

1) This study has revealed that the plutonic body in the Upper Mustang region, commonly referred to as the Mustang granite, is in fact a granitic orthogneiss with a Paleozoic protolith and a Himalayan metamorphic and anatectic overprint. Further field-based research is needed in order to investigate the contact between the orthogneiss and the surrounding TSS. This contact may be structural and represent an exposure of the STDS similar to that in culminations along the North Himalayan anticline.

2) Understanding of the relationship between the thermal evolution of rocks in the uppermost Himalaya and E-W extensional structures in the Tibetan plateau may benefit from further detailed thermochronologic studies, based on rocks from E-W extensional zones in both the plateau and the Himalaya. Many of the studies mentioned in previous sections that attempt to date the onset of E-W extension use only one chronometer. By applying multiple chronometers, as done in this study, the evolution of cooling rates across Tibet may be better constrained. These data are necessary to better resolve the regional process(es) responsible for the development of E-W extensional structures and the transition from N-S dominant kinematics.

3) Hurtado (2002), using LANSAT imagery of the Upper Mustang, interpreted two portions of the Mustang granite, one on the western side of the graben (visited in this study), and one on the eastern side. Field work in the northeast Thakkhola graben is required in order to investigate the nature of this second pluton, and its relationship to the Mustang gneiss and granite as observed in this study. If it can be demonstrated that this was originally a singular body that was bisected during graben initiation (Hurtado, 2002), then this could be used to precisely constrain the amount of E-W separation experienced in the graben and contribute to estimates of total E-W extension experienced in the Tibetan plateau, which is as of yet unknown.

4) Apatite U-Th/He data are missing from the Ghami location of this study, and zircon

U-Th/He data from the Ghar Ghompa location is sparse. Replacing the missing data would increase confidence in cooling ages and improve the accuracy of cooling paths from these locations. A return visit to the Ghami and Ghar Ghompa locations to sample the TSS surrounding the granite may yield the missing apatite and zircon.

Bibliography

Ayres, M. and Harris, N. B. W. (1997). REE fractionation and Nd-isotope disequilibrium during crustal anatexis: constraints from Himalayan leucogranites. *Chemical Geology*, 139(1-4):249–269. → pages 57

Beaumont, C., Jamieson, R. A., Nguyen, M. H., and Medvedev, S. (2004). Crustal channel flows: 1. Numerical models with applications to the tectonics of the Himalayan-Tibetan orogen. *Journal of Geophysical Research B: Solid Earth*, 109(6):1–29. → pages 5

Best, M. G., Christiansen, E. H., Deino, A. L., Grommé, C. S., and Tingey, D. G. (1995). Correlation and emplacement of a large, zoned, discontinuously exposed ash flow sheet: The 40 Ar/ 39 Ar chronology, paleomagnetism, and petrology of the Pahranagat Formation, Nevada. *Journal of Geophysical Research: Solid Earth*, 100(B12):24593–24609. → pages 82

Bollinger, L., Avouac, J. P., Beyssac, O., Catlos, E. J., Harrison, T. M., Grove, M., Goffé, B., and Sapkota, S. (2004). Thermal structure and exhumation history of the Lesser Himalaya in central Nepal. *Tectonics*, 23(5):1–19. → pages 1, 4

Burchfiel, B. C. and Royden, L. H. (1985). North-south extension within the convergent Himalayan region. *Geology*, 13(10):679–682. → pages 5

Clark, M. K. and Royden, L. H. (2000). Topographic ooze: Building the eastern margin of Tibet by lower crustal flow. *Geology*, 28(8):703–706. → pages 5, 67

Clift, P. D., Hodges, K. V., Heslop, D., Hannigan, R., Van Long, H., and Calves, G. (2008). Correlation of Himalayan exhumation rates and Asian monsoon intensity. *Nature Geoscience*, 1(12):875–880. → pages 67

Colchen, M. (1999). The Thakkhola-Mustang graben in Nepal and the late Cenozoic extension in the Higher Himalayas. *Journal of Asian Earth Sciences*, 17(5-6):683–702. → pages 6, 7

Coleman, M. and Hodges, K. (1995). Evidence for Tibetan Plateau Uplift before 14-Myr Ago from a New Minimum Age for East-West Extension. *Nature*, 374(6517):49–52. → pages 7, 62

Cooper, F. J., Hodges, K. V., Parrish, R. R., Roberts, N. M., and Horstwood, M. S. (2015). Synchronous N-S and E-W extension at the Tibet-to-Himalaya transition in NW Bhutan. *Tectonics*, 34(7):1375–1395. → pages 62

Copeland, P., Mark Harrison, T., and Le Fort, P. (1990). Age and cooling history of the Manaslu granite: implications for Himalayan tectonics. *Journal of Volcanology and Geothermal Research*, 44(1-2):33–50. → pages 57

Cottle, J. M., Jessup, M. J., Newell, D. L., Horstwood, M. S. A., Noble, S. R., Parrish, R. R., Waters, D. J., and Searle, M. P. (2009). Geochronology of granulitized eclogite from the Ama Drime Massif: Implications for the tectonic evolution of the South Tibetan Himalaya. *Tectonics*, 28(1). → pages 5, 11, 64, 67

Cottle, J. M., Jessup, M. J., Newell, D. L., Searle, M. P., Law, R. D., and Horstwood, M. S. A. (2007). Structural insights into the early stages of exhumation along an orogen-scale detachment: The South Tibetan Detachment System, Dzakaa Chu section, Eastern Himalaya. *Journal of Structural Geology*, 29(11):1781–1797. → pages 67

Cottle, J. M., Larson, K. P., and Kellett, D. A. (2015). How does the mid-crust accommodate deformation in large, hot collisional orogens? A review of recent research in the Himalayan orogen. *Journal of Structural Geology*, 78:119–133. → pages 1, 4

Dalrymple, B. G. and Lanphere, M. A. (1971). 40Ar/39Ar technique of KAr dating: a comparison with the conventional technique. *Earth and Planetary Science Letters*, 12(3):300–308. → pages 14

Dazé, A., Lee, J. K., and Villeneuve, M. (2003). An intercalibration study of the Fish Canyon sanidine and biotite 40Ar/39Ar standards and some comments on the age of the Fish Canyon Tuff. *Chemical Geology*, 199(1-2):111–127. → pages 82

DeCelles, P. G., Robinson, D. M., Quade, J., Ojha, T. P., Garzione, C. N., Copeland, P., and Upreti, B. N. (2001). Stratigraphy, structure, and tectonic evolution of the Himalayan fold-thrust belt in Western Nepal. *Tectonics*, 20(4):487–509. → pages 1, 4

Deino, A. (2013). MassSpec Software v.8.091. → pages 18, 83

Deniel, C., Vidal, P., Fernandez, A., Le Fort, P., and Peucat, J. J. (1987). Isotopic study of the Manaslu granite (Himalaya, Nepal): inferences on the age and source of Himalayan leucogranites. *Contributions to Mineralogy and Petrology*, 96(1):78–92. → pages 6, 34

Dewane, T. J., Stockli, D. F., Hager, C., Taylor, M., Ding, L., Lee, J., and Wallis, S. (2006). Timing of Cenozoic E-W Extension in the Tangra Yum Co-Kung Co Rift, south-central Tibet. In *American Geophysical Union, Fall Meeting*, pages T34C–04. → pages 63

Dodson, M. H. (1973). Closure temperature in cooling geochronological and petrological systems. *Contributions to Mineralogy and Petrology*, 40(3):259–274. → pages 10, 11, 12, 14, 18, 19

Edwards, M. A. and Harrison, T. M. (1997). When did the roof collapse? Late Miocene north-south extension in the high Himalaya revealed by Th-Pb monazite dating of the Khula Kangri granite. *Geology*, 25(6):543–546. → pages 67

Farley, K. A. (2000). Helium diffusion from apatite: General behavior as illustrated by Durango fluorapatite. *Journal of Geophysical Research*, 105(B2):2903–2914. → pages 19, 20

Farley, K. A., Wolf, R. A., and Silver, L. T. (1996). The effects of long alpha-stopping distances on (U-Th)/He ages. *Geochimica et Cosmochimica Acta*, 60(21):4223–4229. → pages 18, 19, 20, 22

Faure, G. and Mensing, T. M. (2009). *Isotopes: Principles and Applications*. Wiley India Pvt. Ltd., New Delhi, third edit edition. → pages 10, 11, 13, 14, 19

Flowers, R. M., Ketcham, R. A., Shuster, D. L., and Farley, K. A. (2009). Apatite (U-Th)/He thermochronometry using a radiation damage accumulation and annealing model. *Geochimica et Cosmochimica Acta*, 73(8):2347–2365. → pages 18, 21, 24, 57

Fort, M., Freytet, P., and Colchen, M. (1982). Structural and Sedimentological Evolution of the Thakkhola Mustang Graben (Nepal Himalayas). *Zeitschrift fur Geomorphologic N.F.*, 42:75–98. → pages 6, 7

Garzione, C. N., DeCelles, P. G., Hodkinson, D. G., Ojha, T. P., and Upreti, B. N. (2003). East-west extension and Miocene environmental change in the southern Tibetan plateau: Thakkola graben, central Nepal. *Geological Society of America Bulletin*, 115(1):3–20. → pages 6, 7, 63

Garzione, C. N., Dettman, D. L., Quade, J., DeCelles, P. G., and Butler, R. F. (2000). High times on the Tibetan Plateau: Paleoelevation of the Thakkhola graben, Nepal. *Geology*, 28(4):339. → pages 62

Gautheron, C., Tassan-Got, L., and Ketcham, R. A. (2011). Alpha FT-ejection factor. → pages 23

Gillot, P.-Y., Hildenbrand, A., Lefevre, J.-C., and Albore-Livadie, C. (2006). The K/Ar Dating Method: Principle, Analytical Techniques, and Application to Holocene Volcanic Eruptions in Southern Italy. *Acta Vulcanologica*, 18(1-2):55–66. → pages 12

Godin, L., Gleeson, T. P., Searle, M. P., Ullrich, T. D., and Parrish, R. R. (2006). Locking of southward extrusion in favour of rapid crustal-scale buckling of the Greater Himalayan sequence, Nar valley, central Nepal. *Geological Society, London, Special Publications*, 268(1):269–292. → pages 5

Godin, L., Parrish, R. R., Brown, R. L., and Hodges, K. V. (2001). Crustal thickening leading to exhumation of the Hmalayan Metamorphic core of central Nepal: Insight from U-Pb Geochronology and 40Ar/39Ar Thermochronology. *Tectonics*, 20(5):729–747. → pages 5, 63, 67

Guenthner, W. R., Reiners, P. W., Ketcham, R. A., Nasdala, L., and Giester, G. (2013). Helium diffusion in natural zircon: radiation damage, anisotropy, and the interpretation of zircon (U-TH)/He thermochronology. *American Journal of Science*, 313(3):145–198. → pages 21, 24, 57

Hames, W. E. and Bowring, S. A. (1994). An empirical evaluation of the argon diffusion geometry in muscovite. *Earth and Planetary Science Letters*, 124(1-4):161–167. → pages 10

Harrison, M. T., Grove, M., Mckeegan, K. D., Coath, C. D., Lovera, O. M., and Fort, P. L. (1999). Origin and Episodic Emplacement of the Manaslu Intrusive Complex, Central Himalaya. *Journal of Petrology*, 40(1):3–19. → pages 6

Harrison, T. M., Duncan, I., and McDougall, I. (1985). Diffusion of 40Ar in biotite: Temperature, pressure and compositional effects. *Geochimica et Cosmochimica Acta*, 49(11):2461–2468. → pages 10

Harrison, T. M. and Zeitler, P. K. (2005). Fundamentals of Noble Gas Thermochronometry. *Reviews in Mineralogy and Geochemistry*, 58(1):123–149. → pages 10, 11, 13, 15, 16, 19

Hauck, M. L., Nelson, K. D., Brown, L. D., Zhao, W., and Ross, A. R. (1998). Crustal structure of the Himalayan orogen at -90 east longitude from Project INDEPTH deep reflection profiles. *Tectonics*, 17(4):481–500. → pages 3

Hodges, K. (2000). Tectonics of the Himalaya and southern Tibet from two perspectives. *GSA Bulletin*, 112(3):324–350. → pages 1, 4, 5, 9

Hodges, K. V., Parrish, R. R., Housh, T. B., Lux, D. R., Burchfiel, B. C., Royden, L. H., and Chen, Z. (1992). Simultaneous Miocene Extension and Shortening in the Himalayan Orogen. *Science*, 258(5087):1466–1470. → pages 5

Hurley, P. M. (1950). Distribution of Radioactivity in Granites and Possible Relation to Helium Age Measurement. *Bulletin of the Geological Society of America*, 61(January):1–8. → pages 18

Hurley, P. M. and Goodman, C. (1941). Helium Retention in Common Rock Minerals. *Bulletin of the Geological Society of America*, 52:545–560. → pages 18

Hurley, P. M. and Goodman, C. (1943). Helium age measurement. i. Preliminary Magnetite Index. *Bulletin of the Geological Society of America*, 54(March):305–324. → pages 18

Hurtado, J., Hodges, K. V., and Whipple, K. X. (2001). Neotectonics of the Thakkhola graben and implications for recent activity on the South Tibetan fault system in the Central Nepal Himalaya. *Bulletin of the Geological Society of America*, 113(2):222–240. → pages 6, 7

Hurtado, J. M. (2002). *Tectonic Evolution of the Thakkhola Graben and Dhaulagiri Himalaya, Central Nepal*. PhD thesis, Massachusetts Institute of Technology. → pages 5, 6, 7, 9, 34, 63, 68

Jamieson, R. A., Beaumont, C., Medvedev, S., and Nguyen, M. H. (2004). Crustal channel flows: 2. Numerical models with implications for metamorphism in the Himalayan-Tibetan orogen. *Journal of Geophysical Research B: Solid Earth*, 109(6):1–24. → pages 5

Kali, E., Leloup, P. H., Arnaud, N., Maheo, G., Liu, D., Boutonnet, E., Van der Woerd, J., Liu, X., Liu-Zeng, J., and Li, H. (2010). Exhumation history of the deepest central Himalayan rocks, Ama Drime range: Key pressure-temperature-deformation-time constraints on orogenic models. *Tectonics*, 29:TC2014. → pages 63

Kellett, D. A. and Grujic, D. (2012). New insight into the South Tibetan detachment system: Not a single progressive deformation. *Tectonics*, 31(2):1–18. → pages 5

Kellett, D. A., Grujic, D., and Erdmann, S. (2009). Miocene structural reorganization of the South Tibetan detachment, eastern Himalaya: Implications for continental collision. *Lithosphere*, 1(5):259–281. → pages 67

Kelley, S. (2002a). Excess argon in K-Ar and Ar-Ar geochronology. *Chemical Geology*, 188(1-2):1–22. → pages 12, 15

Kelley, S. (2002b). K-Ar and Ar-Ar Dating. *Reviews in Mineralogy and Geochemistry*, 47(1):785–818. → pages 10, 14, 15, 17

Ketcham, R. A. (2005). Forward and Inverse Modeling of Low-Temperature Thermochronometry Data. *Reviews in Mineralogy and Geochemistry*, 58(1):275–314. → pages 21, 24, 57

Ketcham, R. A., Carter, A., Donelick, R. A., Barbarand, J., and Hurford, A. J. (2007). Improved modeling of fission-track annealing in apatite. *American Mineralogist*, 92(5-6):799–810. → pages 18

Ketcham, R. A., Gautheron, C., and Tassan-Got, L. (2011). Accounting for long alpha-particle stopping distances in (U-Th-Sm)/He geochronology: Refinement of the baseline case. *Geochimica et Cosmochimica Acta*, 75(24):7779–7791. → pages 18, 24

Kirby, E., Reiners, P. W., Krol, M. A., Whipple, K. X., Hodges, K. V., Farley, K. A., Tang, W., and Chen, Z. (2002). Late Cenozoic evolution of the eastern margin of the Tibetan Plateau:

Inferences from 40 Ar/ 39 Ar and (U-Th)/He thermochronology. *Tectonics*, 21(1):1–19. → pages 67

Kohn, M. J. (2014). Himalayan Metamorphism and Its Tectonic Implications. *Annu. Rev. Earth Planet. Sci*, 42:381–419. → pages 1, 4, 5

Kuiper, K. F., Deino, A., Hilgen, F. J., Krijgsman, W., Renne, P. R., and Wijbrans, J. R. (2008). Synchronizing Rock Clocks. *Science*, 320(April):500–504. → pages 82

Lanphere, M. A. and Dalrymple, B. G. (1976). Identification of excess 40Ar by the 40Ar39Ar, age spectrum technique. *Earth and Planetary Science Letters*, 32(2):141–148. → pages 15, 45

Larson, K. P., Camacho, A., Cottle, J. M., Coutand, I., Buckingham, H. M., Ambrose, T. K., and Rai, S. M. (2017). Cooling, exhumation, and kinematics of the Kanchenjunga Himal, far east Nepal. *Tectonics*, (Figure 1):1–16. → pages 39

Larson, K. P. and Cottle, J. M. (2015). Initiation of crustal shortening in the Himalaya. *Terra Nova*, 27(3):169–174. → pages 39

Larson, K. P., Godin, L., Davis, W. J., and Davis, D. W. (2010). Out-of-sequence deformation and expansion of the Himalayan orogenic wedge: Insight from the Changgo culmination, south central Tibet. *Tectonics*, 29(4). → pages 3, 5

Larson, K. P., Kellett, D. A., Cottle, J. M., Brubacher, A. D., and Camacho, A. (In Prep.). Mid-Miocene Initiation of E-W extension and Recoupling of the Himalayan Orogen. → pages 62

Le Fort, P. (1975). Himalayas: the collided range. Present knowledge of the continental arc. → pages 1, 4

Le Fort, P., Cuney, M., Deniel, C., France-Lanord, C., Sheppard, S. M. F., Upreti, B. N., and Vidal, P. (1987). Crustal generation of the Himalayan leucogranites. *Tectonophysics*, 134(1-3):39–57. → pages 6, 34

Le Fort, P. and France-Lanord, C. (1994). Granites from Mustang and surrounding regions, central Nepal. *Nepal Geological Society Journal*, 10. → pages 6

Lederer, G. W., Cottle, J. M., Jessup, M. J., Langille, J. M., and Ahmad, T. (2013). Timescales of partial melting in the Himalayan middle crust: Insight from the Leo Pargil dome, northwest India. *Contributions to Mineralogy and Petrology*, 166(5):1415–1441. → pages 39

Lee, J., Hacker, B. R., Dinklage, W. S., Wang, Y., Gans, P., Calvert, A., Wan, J., Chen, W., Blythe, A. E., and McClelland, W. (2000). Evolution of the Kangmar Dome, Southern Tibet:

Structural, petrologic, and thermochronologic constraints. *Tectonics*, 19(5):872–895. → pages 5

Lee, J., McClelland, W., Wang, Y., Blythe, A., and McWilliams, M. (2006). Oligocene-Miocene middle crustal flow in southern Tibet: geochronology of Mabja Dome. *Geological Society, London, Special Publications*, 268(1):445–469. → pages 5

Leloup, P. H., Mahéo, G., Arnaud, N., Kali, E., Boutonnet, E., Liu, D., Xiaohan, L., and Haibing, L. (2010). The South Tibet detachment shear zone in the Dinggye area. Time constraints on extrusion models of the Himalayas. *Earth and Planetary Science Letters*, 292(1-2):1–16. → pages 64, 67

Lippolt, H. J., Leitz, M., Wernicke, R. S., and Hagedorn, B. (1994). (Uranium + thorium)/helium dating of apatite: experience with samples from different geochemical environments. *Chemical Geology*, 112(1-2):179–191. → pages 20

Liu, G. and Einsele, G. (1994). Sedimentary history of the Tethyan basin in the Tibetan Himalayas. *Geologische Rundschau*, 83(1):32–61. → pages 5

Liu, Z. C., Wu, F. Y., Qiu, Z. L., Wang, J. G., Liu, X. C., Ji, W. Q., and Liu, C. Z. (2017). Leucogranite geochronological constraints on the termination of the South Tibetan Detachment in eastern Himalaya. *Tectonophysics*, 721(October 2016):106–122. → pages 67

Ludwig, K. (2003). Isoplot 3.0 user manual. *Berkeley Geochronology Center Special Publication*, 4. → pages 18, 34

Mahéo, G., Leloup, P. H., Valli, F., Lacassin, R., Arnaud, N., Paquette, J. L., Fernandez, A., Haibing, L., Farley, K. A., and Tapponnier, P. (2007). Post 4 Ma initiation of normal faulting in southern Tibet. Constraints from the Kung Co half graben. *Earth and Planetary Science Letters*, 256(1-2):233–243. → pages 62

Martin, A. J. (2017). A review of definitions of the Himalayan Main Central Thrust. *International Journal of Earth Sciences*, 106(6):2131–2145. → pages 4

Mascle, G., Pecher, A., Guillot, S., and Gajurel, A. (2012). *The Himalaya-Tibet Collision*. Nepal Geological Society, Kathmandu. → pages 1, 4, 5

McDougall, I. and Harrison, T. M. (1999). *Geochronology and Thermochronology by the 40Ar/39Ar method*. Oxford University Press, New York, second edition. → pages 11, 12, 13, 14, 15, 18, 21

Meesters, A. and Dunai, T. (2002). Solving the production diffusion equation for finite diffusion domains of various shapes : Part II . Application to cases with alpha-ejection and nonhomogeneous distribution of the source. *Chemical Geology*, 186:347–363. → pages 20

Meigs, A. J., Burbank, D. W., and Beck, R. A. (1995). Middle-late Miocene (>10 Ma) formation of the Main Boundary Thrust in the western Himalaya. *Geology*, 23(5):423–426. → pages 67

Merrihue, C. and Turner, G. (1966). Potassium-Argon Dating by Activation with Fast Neutrons. *Journal of Geophysical Research*, 71(11):2852–2857. → pages 12, 14

Mitchell, J. G. (1968). The argon-40/argon-39 method for potassium-argon age determinations. *Geochimica et Cosmochimica Acta*, 32:781–790. → pages 12, 13

Mitsuishi, M., Wallis, S. R., Aoya, M., Lee, J., and Wang, Y. (2012). E-W extension at 19Ma in the Kung Co area, S. Tibet: Evidence for contemporaneous E-W and N-S extension in the Himalayan orogen. *Earth and Planetary Science Letters*, 325-326:10–20. → pages 62

Molnar, P. and Stock, J. M. (2009). Slowing of India's convergence with Eurasia since 20 Ma and its implications for Tibetan mantle dynamics. *Tectonics*, 28(3):1–11. → pages 5

Montomoli, C., Carosi, R., and Iaccarino, S. (2015). Tectonometamorphic discontinuities in the Greater Himalayan Sequence: a local or a regional feature? *Geological Society, London, Special Publications*, 412(July):SP412.3–. → pages 4

Montomoli, C., Iaccarino, S., Carosi, R., Langone, A., and Visonà, D. (2013). Tectonometamorphic discontinuities within the Greater Himalayan Sequence in Western Nepal (Central Himalaya): Insights on the exhumation of crystalline rocks. *Tectonophysics*, 608:1349–1370. → pages 1, 4, 5

Murphy, M. A. and Copeland, P. (2005). Transtensional deformation in the central Himalaya and its role in accomodating growth of the Himalayan orogen. *Tectonics*, 24(4):1–19. → pages 62

Myrow, P. M., Hughes, N. C., Paulsen, T. S., Williams, I. S., Parcha, S. K., Thompson, K. R., Bowring, S. A., Peng, S. C., and Ahluwalia, A. D. (2003). Integrated tectonostratigraphic analysis of the Himalaya and implications for its tectonic reconstruction. *Earth and Planetary Science Letters*, 212(3-4):433–441. → pages 1

Noble, S. R. and Searle, M. P. (1995). Age of crustal melting and leucogranite formation from U-Pb zircon and monazite dating in the western Himalaya, Zanskar, India. *Geology*, 23(12):1135–1138. → pages 6

Parrish, R. R. (1990). U-Pb dating of monazite and its application to geological problems. *Can. J. Earth Sci*, 27(Overstreet 1967):1431–1450. → pages 11

Ratschbacher, L., Krumrei, I., Blumenwitz, M., Staiger, M., Gloaguen, R., Miller, B. V., Samson, S. D., Edwards, M. A., and Appel, E. (2011). Rifting and strike-slip shear in central Tibet

and the geometry, age and kinematics of upper crustal extension in Tibet. *Geological Society, London, Special Publications*, 353(1):127–163. → pages 5, 63

Reiners, P. W., Farley, K. A., and Hickes, H. J. (2002). He diffusion and (U-Th)/He thermochronometry of zircon: Initial results from Fish Canyon Tuff and Gold Butte. *Tectonophysics*, 349(1-4):297–308. → pages 19, 21

Renne, P. R., Cassata, W. S., and Morgan, L. E. (2009). The isotopic composition of atmospheric argon and 40Ar/39Ar geochronology: Time for a change? *Quaternary Geochronology*, 4(4):288–298. → pages 14

Renne, P. R. and Norman, E. B. (2001). Determination of the half-life of 37Ar by mass spectrometry. *Physical Review C - Nuclear Physics*, 63(4):473021–473023. → pages 83

Renne, P. R., Swisher, C. C., Deino, A. L., Karner, D. B., Owens, T. L., and DePaolo, D. J. (1998). Intercalibration of standards, absolute ages and uncertainties in 40Ar/39Ar dating. *Chemical Geology*, 145:117–152. → pages 83

Roddick, J. (1983). High precision intercalibration of 40Ar-39Ar standards. *Geochimica et Cosmochimica Acta*, 47(5):887–898. → pages 83

Ross, J. (2017). Pychron software. → pages 83

Rowley, D. B. (1996). Age of initiation of collision between India and Asia: A review of stratigraphic data. *Earth and Planetary Science Letters*, 145(96):1–13. → pages 1

Royden, L. H., Burchfiel, B. C., King, R. W., Wang, E., Royden, L. H., Burchfiel, B. C., King, R. W., Wang, E., Chen, Z., Shen, F., and Liu, Y. (1997). Surface Deformation and Lower Crustal Flow in Eastern Tibet. 276(5313):788–790. → pages 67

Schärer, U. (1984). The effect of initial 230Th disequilibrium on young UPb ages: the Makalu case, Himalaya. *Earth and Planetary Science Letters*, 67(2):191–204. → pages 6, 11, 34

Schärer, U., Xu, R. H., and Allègre, C. J. (1986). U(Th)Pb systematics and ages of Himalayan leucogranites, South Tibet. *Earth and Planetary Science Letters*, 77(1):35–48. → pages 11

Searle, M. P., Cottle, J. M., Streule, M. J., and Waters, D. J. (2009). Crustal melt granites and migmatites along the Himalaya: Melt source, segregation, transport and granite emplacement mechanisms. *Earth and Environmental Science Transactions of the Royal Society of Edinburgh*, 100(1-2):219–233. → pages 6, 34

Searle, M. P., Law, R. D., Godin, L., Larson, K. P., Steule, M. J., Cottle, J. M., and Jessup, M. J. (2008). Defining the Himalayan Main Central Thrust in Nepal. *Journal of the Geological Society, London*, 165:523–534. → pages 4, 5

Searle, M. P., Law, R. D., and Jessup, M. J. (2006). Crustal structure, restoration and evolution of the Greater Himalaya in Nepal-South Tibet: implications for channel flow and ductile extrusion of the middle crust. *Geological Society, London, Special Publications*, 268(1):355–378. → pages 4, 5

Shuster, D. L., Flowers, R. M., and Farley, K. A. (2006). The influence of natural radiation damage on helium diffusion kinetics in apatite. *Earth and Planetary Science Letters*, 249:148–161. → pages 18, 21, 47, 57

Spell, T. L. and McDougall, I. (2003). Characterization and calibration of 40Ar/39Ar dating standards. *Chemical Geology*, pages 1–23. → pages 82

Steiger, R. H. and Jager, E. (1977). Subcommision on geochronology: convention on the use of decay constants in geo- and cosmochronology. *Earth and Planetary Science Letters*, 36:359–362. → pages 14, 83

Styron, R. H., Taylor, M. H., and Murphy, M. A. (2011). Oblique convergence, arc-parallel extension, and the role of strike-slip faulting in the High Himalaya. *Geosphere*, 7(2):582–596. → pages 65

Sun, X. and Wang, P. (2005). How old is the Asian monsoon system? - Palaeobotanical records from China. *Palaeogeography, Palaeoclimatology, Palaeoecology*, 222(3-4):181–222. → pages 67

Thiede, R. C., Arrowsmith, J. R., Bookhagen, B., McWilliams, M., Sobel, E. R., and Strecker, M. R. (2006). Dome formation and extension in the Tethyan Himalaya, Leo Pargil, northwest India. *Bulletin of the Geological Society of America*, 118(5-6):635–650. → pages 62

Upreti, B. N. (1999). An overview of the stratigraphy and tectonics of the Nepal Himalaya. *Journal of Asian Earth Sciences*, 17(5-6):577–606. → pages 1, 4

Vannay, J. C. and Hodges, K. V. (1996). Tectonometamorphic evolution of the Himalayan metamorphic core between the Annapurna and Dhaulagiri, central Nepal. *Journal of Metamorphic Geology*, 14(5):635–656. → pages 5, 63

Vermeesch, P. (2008). Three new ways to calculate average (U-Th)/He ages. *Chemical Geology*, 249(3-4):339–347. → pages 47, 49, 50, 51, 53, 54

Vermeesch, P. (2010). HelioPlot, and the treatment of overdispersed (U-Th-Sm)/He data. *Chemical Geology*, 271(3-4):108–111. → pages 47

Vermeesch, P., Seward, D., Latkoczy, C., and Wipf, M. (2007). α -Emitting mineral inclusions in apatite , their effect on (U Th)/ He ages , and how to reduce it. *Geochimica et Cosmochimica Acta*, 71:1737–1746. → pages 20, 22

Visonà, D. and Lombardo, B. (2002). Two-mica and tourmaline leucogranites from the Everest-Makalu region (Nepal - Tibet). Himalayan leucogranite genesis by isobaric heating? *Lithos*, 62(3-4):125–150. → pages 57

Whitney, D. L. and Evans, B. W. (2010). Abbreviations for names of rock-forming minerals. *American Mineralogist*, 95(1):185–187. → pages 8, 25

Winter, J. D. (2010). *Principles of Igneous and Metamorphic Petrology*. Prentice Hall, second edition. → pages 25

Wolf, R. A., Farley, K. A., and Silver, L. T. (1996). Helium diffusion and low-temperature thermochronometry of apatite. *Geochimica et Cosmochimica Acta*, 60(21):4231–4240. → pages 20

Wolfe, M. R. and Stockli, D. F. (2010). Zircon (U-Th)/He thermochronometry in the KTB drill hole, Germany, and its implications for bulk He diffusion kinetics in zircon. *Earth and Planetary Science Letters*, 295(1-2):69–82. → pages 21

Wu, C., Nelson, K. D., Wortman, G., and Samson, S. D. (1998). Yadong cross structure and South Tibetan Detachment in the east central Himalaya (89-90E). *Tectonics*, 17(1):28–45. → pages 1, 4, 67

Yin, A. (2006). Cenozoic tectonic evolution of the Himalayan orogen as constrained by along-strike variation of structural geometry, exhumation history, and foreland sedimentation. *Earth-Science Reviews*, 76(1-2):1–131. → pages 1, 4, 5

Yin, A., Kapp, P. A., Murphy, M. A., Manning, C. E., Harrison, T. M., Grove, M., Lin, D., Xi-Guang, D., and Cun-Ming, W. (1999). Significant late Neogene east-west extension in northern Tibet. *Geology*, 27(9):787–790. → pages 5

Zeitler, P. K., Herczeg, A. L., McDougall, I., and Honda, M. (1987). U-Th-He dating of apatite: A potential thermochronometer. *Geochimica et Cosmochimica Acta*, 51(10):2865–2868. → pages 18, 19, 20

Zhang, J. and Guo, L. (2007). Structure and geochronology of the southern Xainza-Dinggye rift and its relationship to the south Tibetan detachment system. *Journal of Asian Earth Sciences*, 29(5-6):722–736. → pages 64

Zhang, P. Z., Shen, Z., Wang, M., Gan, W., Bürgmann, R., Molnar, P., Wang, Q., Niu, Z., Sun, J., Wu, J., Hanrong, S., and Xinzhao, Y. (2004). Continuous deformation of the Tibetan Plateau from global positioning system data. *Geology*, 32(9):809–812. → pages 67

Appendix

Appendix A

I - U-Th/Pb analytical procedures and parameters

U-Th/Pb dating was conducted in collaboration with Dr. John Cottle and the University of California Santa Barbara. Procedures outlined after Cottle et al. (2009) and Braden et al. (2017). Monazite separates were obtained by standard crushing and grinding methods followed by heavy mineral separation using a gold table, heavy liquids (Methyl Iodide), and Franz™ magnetic techniques. Monazite separates and reference materials were rinsed in alcohol, 2% nitric acid and water before being mounted on double-sided tape on an epoxy resin disc. Before analysis the laser beam was rastered on the specimens using a large spot size (∼100 µm) at low fluence (∼0.6 J/cm^2), to further clean the samples and standards (Cottle et al., 2009). Dates were obtained using laser ablation multi-collector inductively coupled plasma mass spectrometry (LA-MC-ICP-MS), which collects all isotopes of interest simultaneously. Specifically, a Photon Machines 193 nm ArF Excimer laser ablation system, connected by a split stream to a multi-collector Nu Plasma. Reference monazites, 44096, FC1, and Bananeira were analysed periodically, and reproduce to within 2% (2σ) of the accepted value. Isotopic data were collected using an 8-10 µm spot, 90 shots, at a frequency of 3 Hz and laser energy of 2.5 mJ.

II - ^{40}Ar/^{39}Ar analytical procedures and parameters

^{40}Ar/^{39}Ar analyses were completed by collaborator Dr. Alfredo Camacho at the University of Manitoba (UMB). All ^{40}Ar/^{39}Ar analytical work was performed at UMB using a multi-collector Thermo Fisher Scientific ARGUSVI mass spectrometer, and a stainless steel Thermo Fisher Scientific extraction/purification line and Photon Machines (55 W) Fusions 10.6 CO_2 laser. Faraday and discrete dynode (CDD) detectors were used to measure Argon isotopes. The sensitivity for argon measurements is ∼6.312 x 10^{17} moles/fA as determined from measured aliquots of Fish Canyon Sanidine (Dazé et al., 2003; Kuiper et al., 2008).

All specimens were irradiated in the Cadmium-lined, in-core CLICIT facility of the Oregon State University TRIGA reactor. The duration of irradiation was 7 hours, using the Fish Canyon sanidine (28.2 Ma; Kuiper et al., 2008) and GA1550 biotite (98.5 Ma; Spell and McDougall, 2003) standards. Standards and unknowns were placed in 2 mm deep wells in 18 mm diameter aluminium disks, with standards strategically placed in order to evaluate the lateral neutron flux gradients across the disk. Planar regressions were fit to the standard data, and the ^{40}Ar/^{39}Ar neutron fluence parameter, J, interpolated for the unknowns. Uncertainties in J are estimated at 0.1 - 0.2% (1σ), based on Monte Carlo error analysis of the planar regressions (Best et al., 1995).

Irradiated samples were placed in a Cu sample tray with a KBr cover slip, and baked with an infrared lamp for 24 hours in a stainless steel high vacuum extraction line. Single crystals were

either fused or step-heated using the laser. Reactive gases were removed, after ∼3 minutes, by three GP-50 SAES getters (two at room temperature and one at 450 °C) prior to being admitted to an ARGUSVI mass spectrometer by expansion. Five argon isotopes were measured simultaneously over a period of 6 minutes. Measured isotope abundances were corrected for extraction-line blanks, which were determined before every sample analysis and averaged ∼2.7 fA for mass 40 and ∼0.01 fA for mass 36.

Mass discrimination was monitored by online analysis of air pipettes, which gave D = 1.0087 ± 0.0003 per amu based on 68 aliquots interspersed with the unknowns. A value of 295.5 was used for the atmospheric $^{40}Ar/^{39}Ar$ ratio (Steiger and Jager, 1977) for the purposes of routine measurement of mass spectrometer discrimination using air aliquots, and correction for atmospheric argon in the $^{40}Ar/^{39}Ar$ age calculation. Corrections are made for neutron-induced ^{40}Ar from potassium, ^{39}Ar and ^{36}Ar from calcium, and ^{36}Ar from chlorine (Roddick, 1983; Renne et al., 1998; Renne and Norman, 2001). Data collection was performed using Pychron (Ross, 2017). Data reduction, error propagation, and age calculation and plotting were performed using MassSpec software (version 8.091; Deino, 2013).

III - U-Th/He analytical procedures and parameters

U-Th/He analyses were completed at the University of Calgary with collaborator Dr. William Matthews. Helium extraction was done using an ASI Alphachron helium line connected to a Prisma-Plus quadrupole mass spectrometer. Durango apatite and Fish Canyon zircon were used as standards for apatite and zircon U-Th/He runs respectively. Uranium and Thorium concentrations were measured by isotope dilution using an Agilent 7700x quadrupole mass spectrometer. Data reduction for helium and actinide concentrations are done in a custom set of spreadsheets.

Zircon and titanite were dissolved using Parr large-capacity dissolution vessels in a multi-step acid-vapor dissolution process. Grains (including the Nb tube) were placed in Ludwig-style Savillex vials, spiked with a $^{235}U/^{230}Th$ mixture, and mixed with 200 µL of Optima grade HF. The vials were then capped, stacked in a 125 mL Teflon liner, placed in a Parr dissolution vessel, and baked at 220 °C for 72 hours. After cooling, the vials were uncapped and dried down on a 90 °C hot plate until dry. The vials then underwent a second round of acid-vapor dissolution, this time with 200 µL of Optima grade HCl in each vial, and baked at 200 °C for 24 hours. Vials were then dried down a second time on a hot plate. Once dry, 200 µL of a 7:1 HNO3:HF mixture was added to each vial, which was subsequently capped and cooked on the hot plate at 90 °C for 4 hours. Following either the apatite or zircon/titanite dissolution process, the samples were diluted with 1 to 3 mL of doubly-deionized water and analyzed by the ICP-MS at the Colorado University Institute for Arctic and Alpine Research. Sample solutions, along with standards and blanks, were analyzed for U, Th, and Sm content using a Thermo Element 2 magnetic sector mass spectrometer.

Appendix B

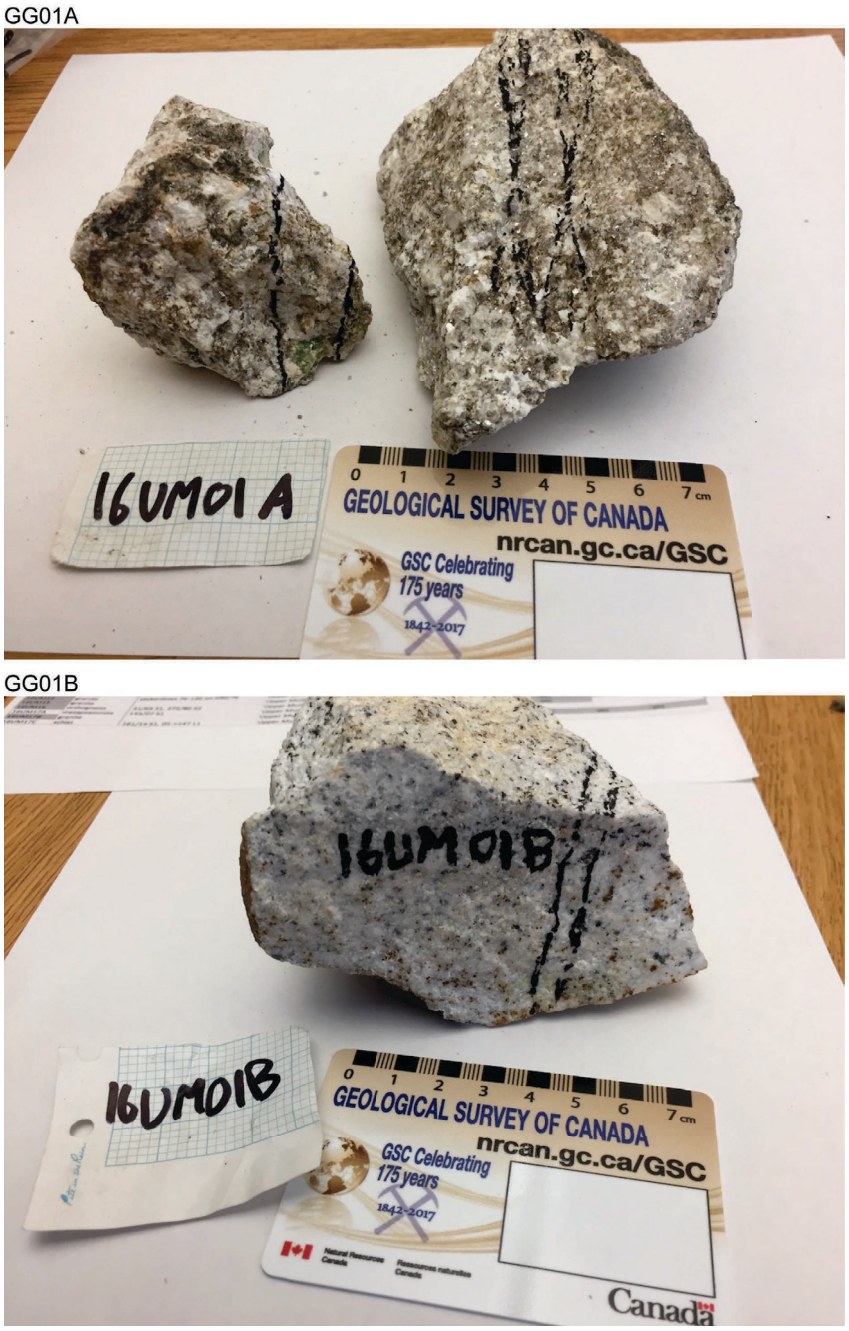

Figure B.1: Hand specimens GG01A and GG01B, from Ghar Ghompa.

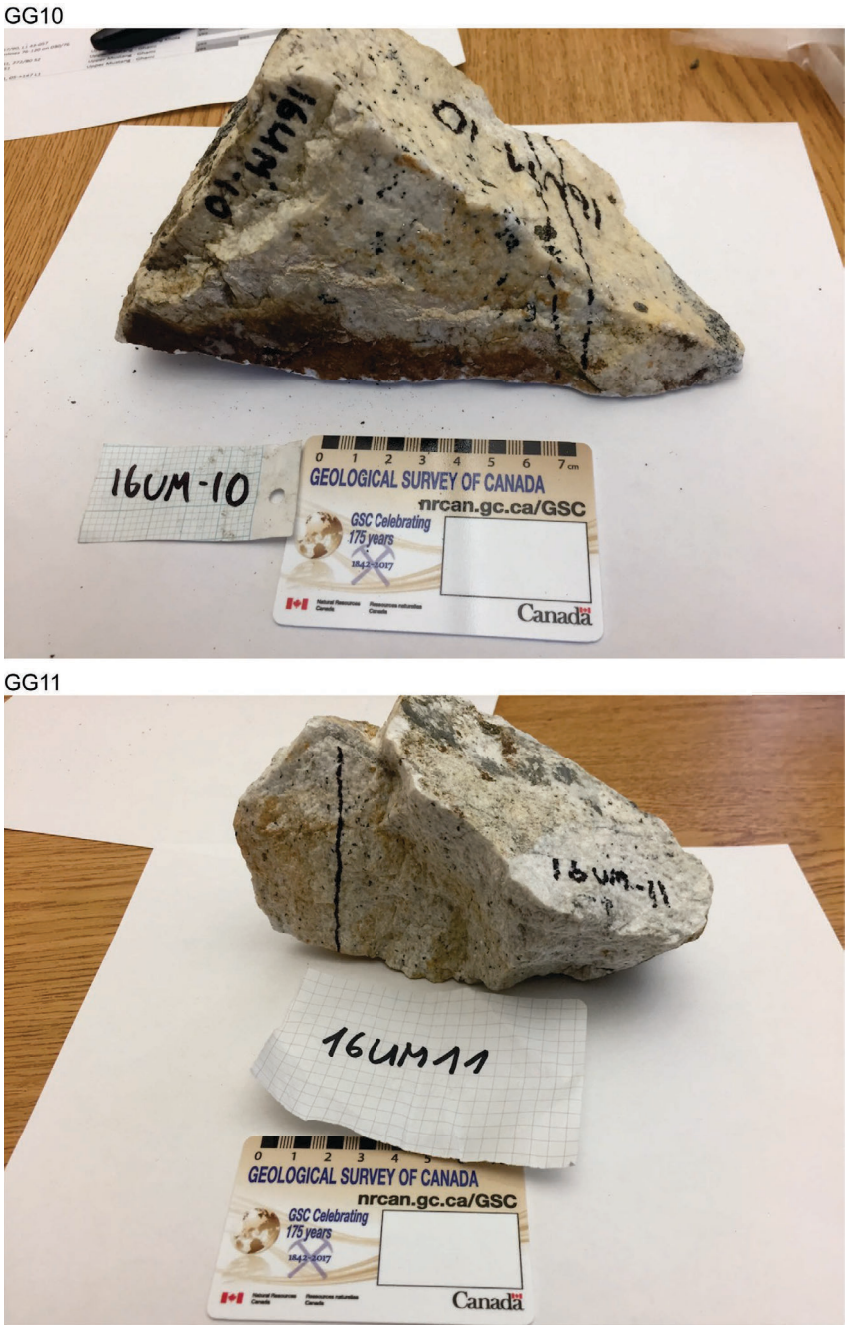

Figure B.2: Hand specimens GG10 and GG11, from Ghar Ghompa.

GG12

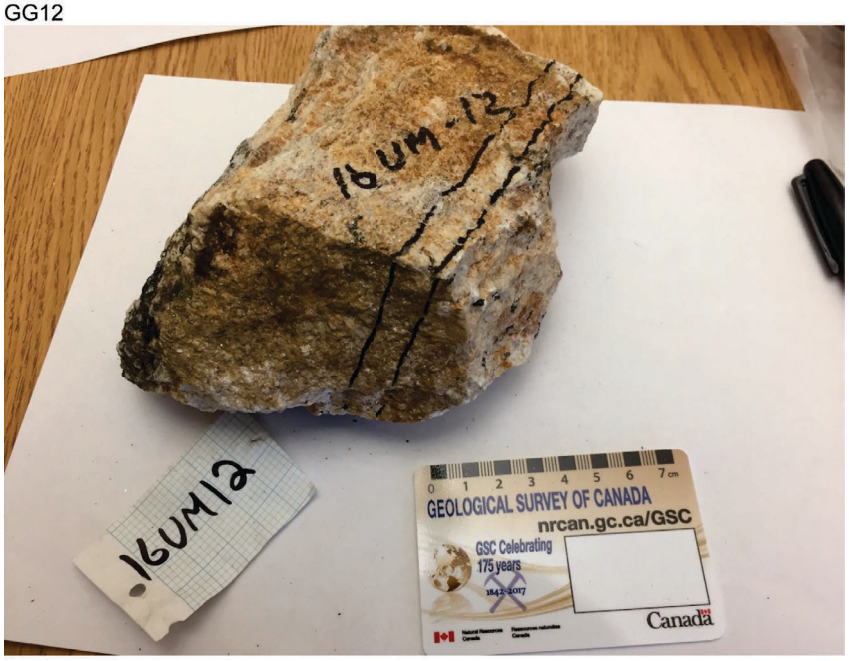

GG13

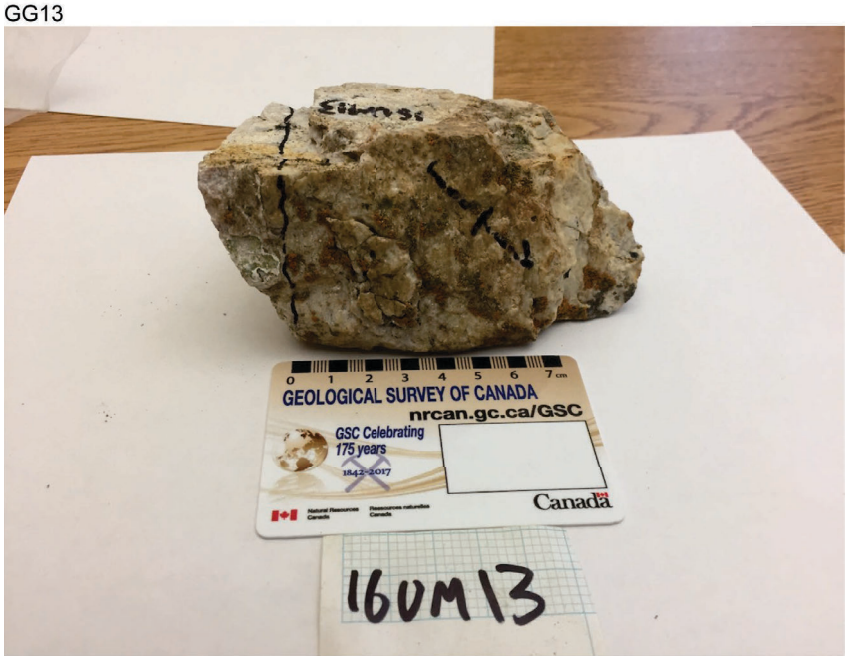

Figure B.3: Hand specimens GG12 and GG013, from Ghar Ghompa.

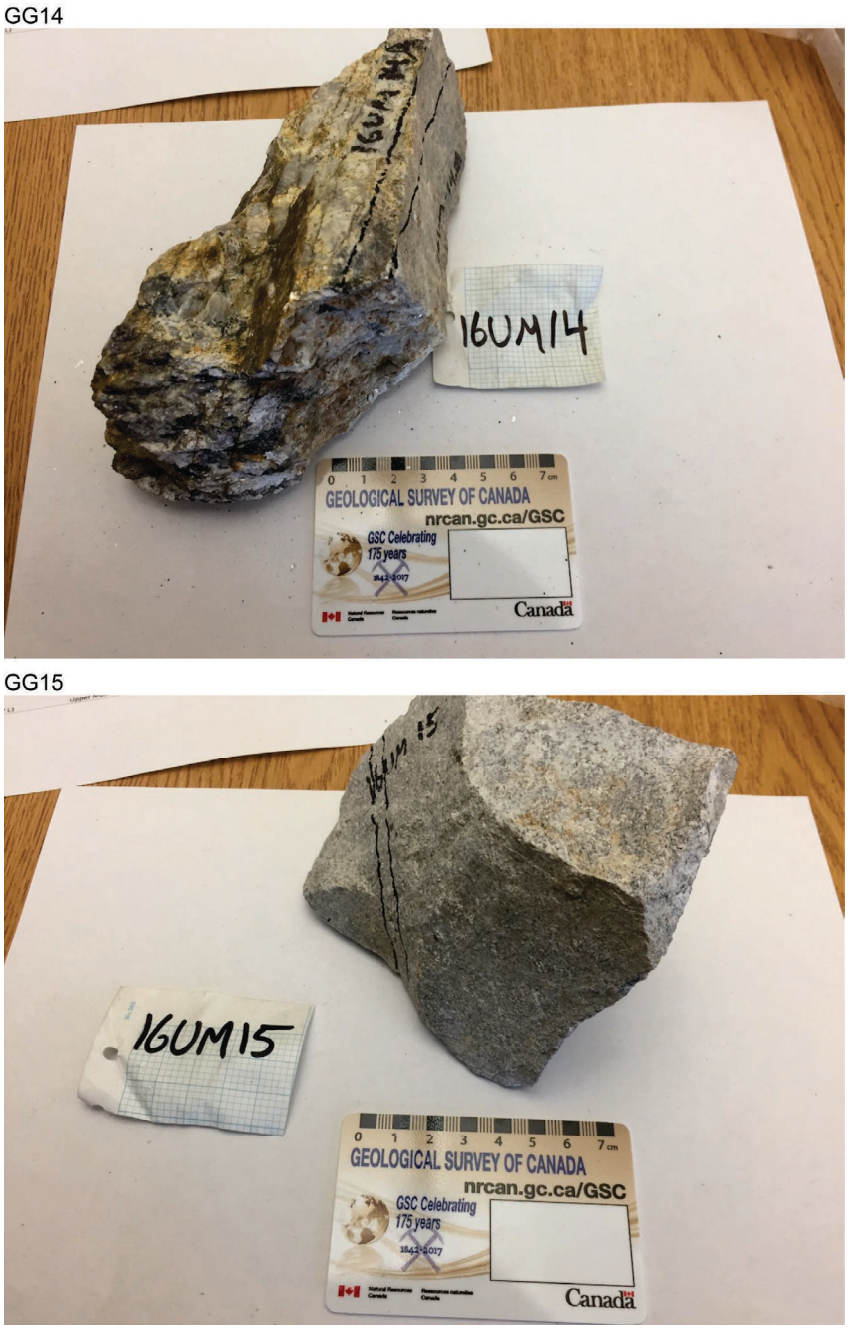

Figure B.4: Hand specimens DK14 and DK15, from Dhanggna Khola

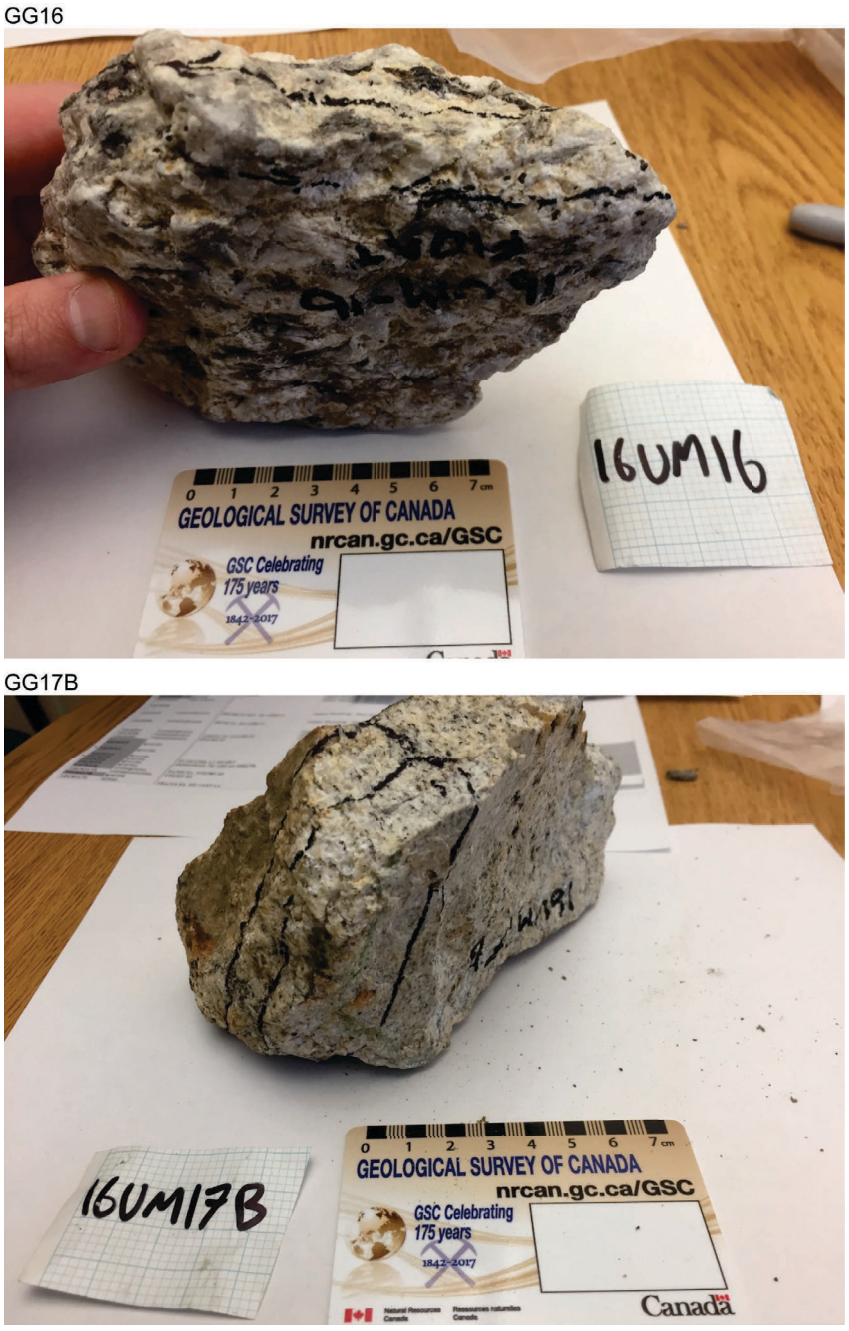

Figure B.5: Hand specimens DK16 and GH17B, from Dhanggna Khola and Ghami, respectively.

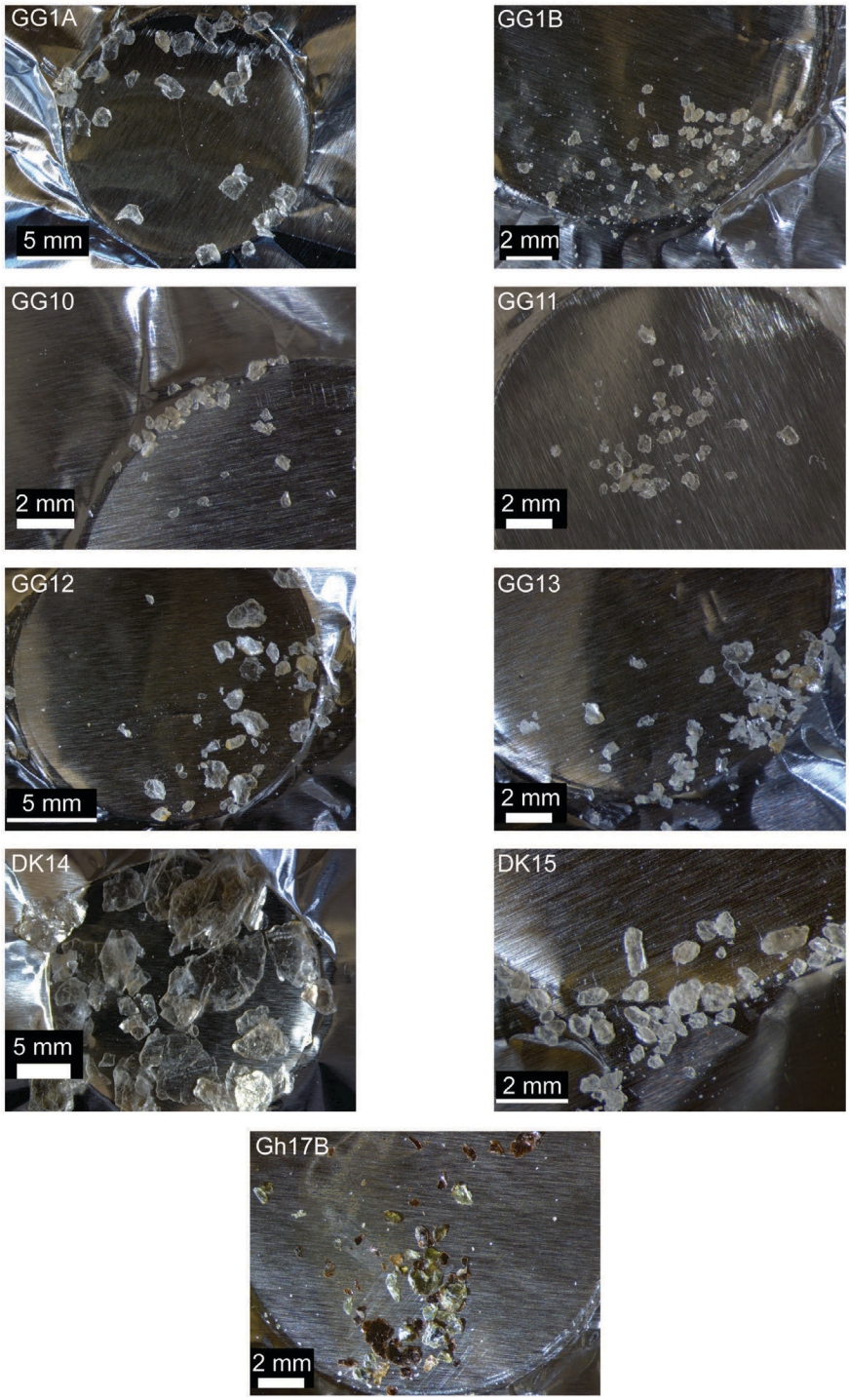

Figure B.6: Mica separates from all granite specimens. Single grain was selected from separates for analysis.

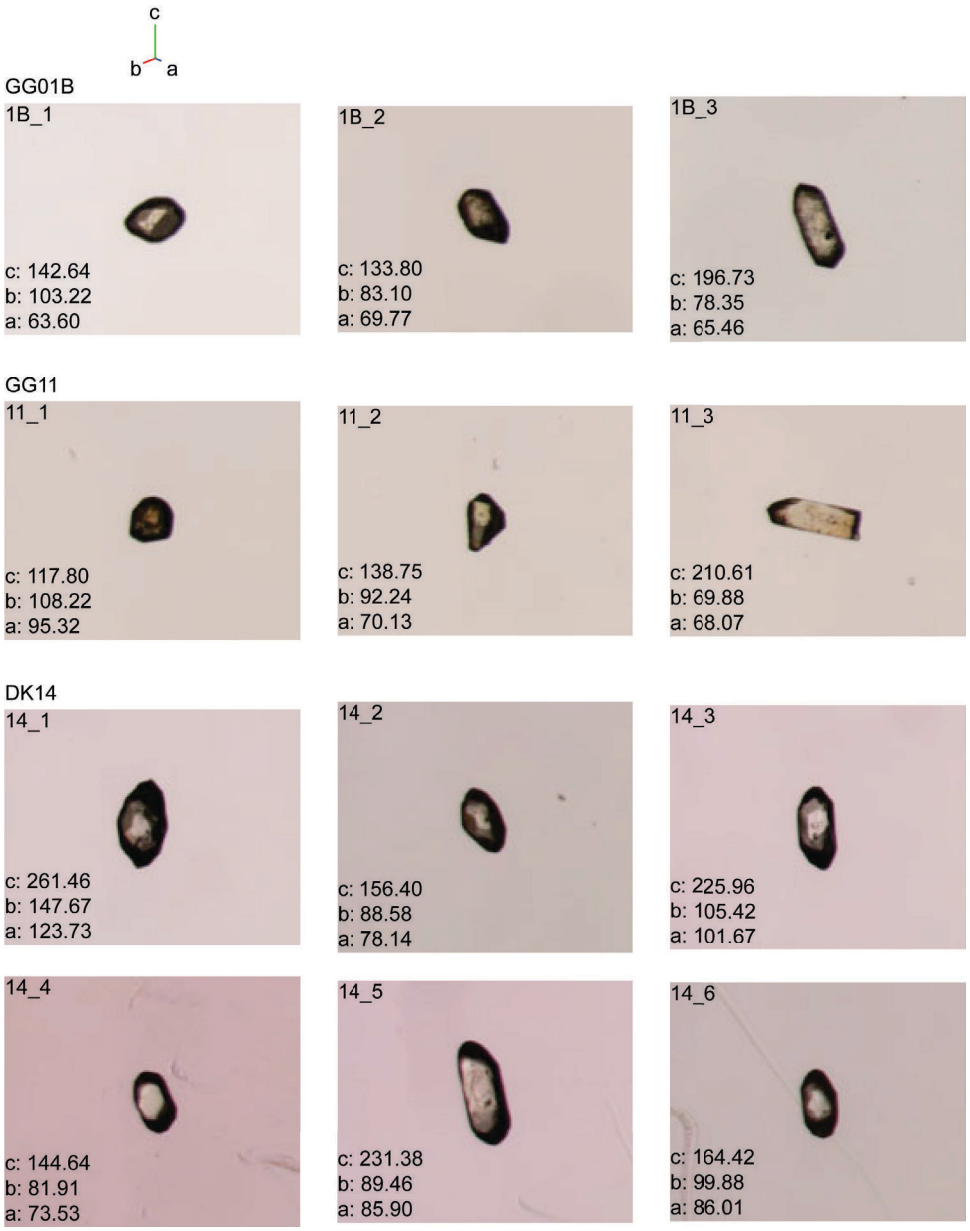

Figure B.7: Zircon crystals selected from specimens GG01B, GG11, and DK14 for U-Th/He analysis. All measurements in micrometers.

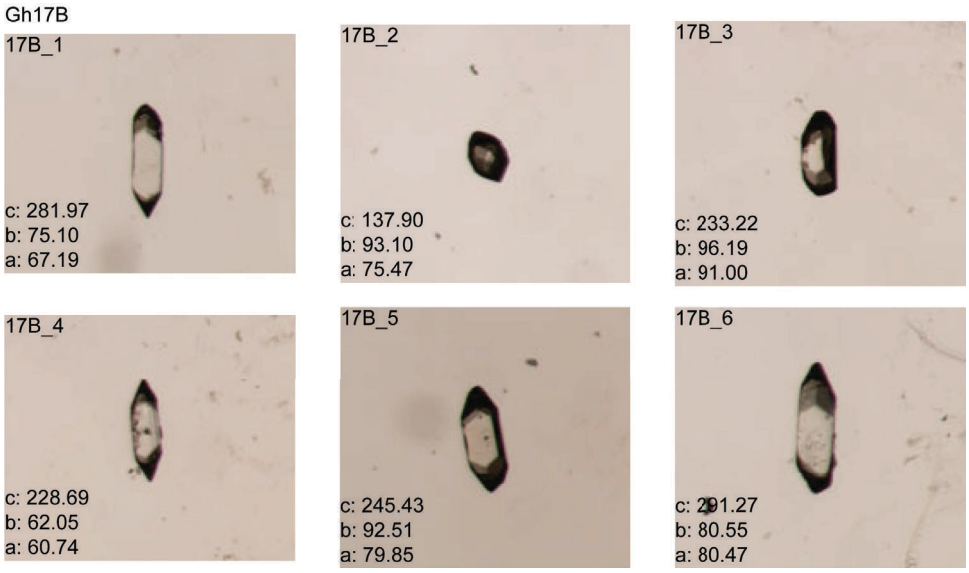

Figure B.8: Zircon crystals selected from specimen GH17B for U-Th/He analysis. All measurements in micrometers.

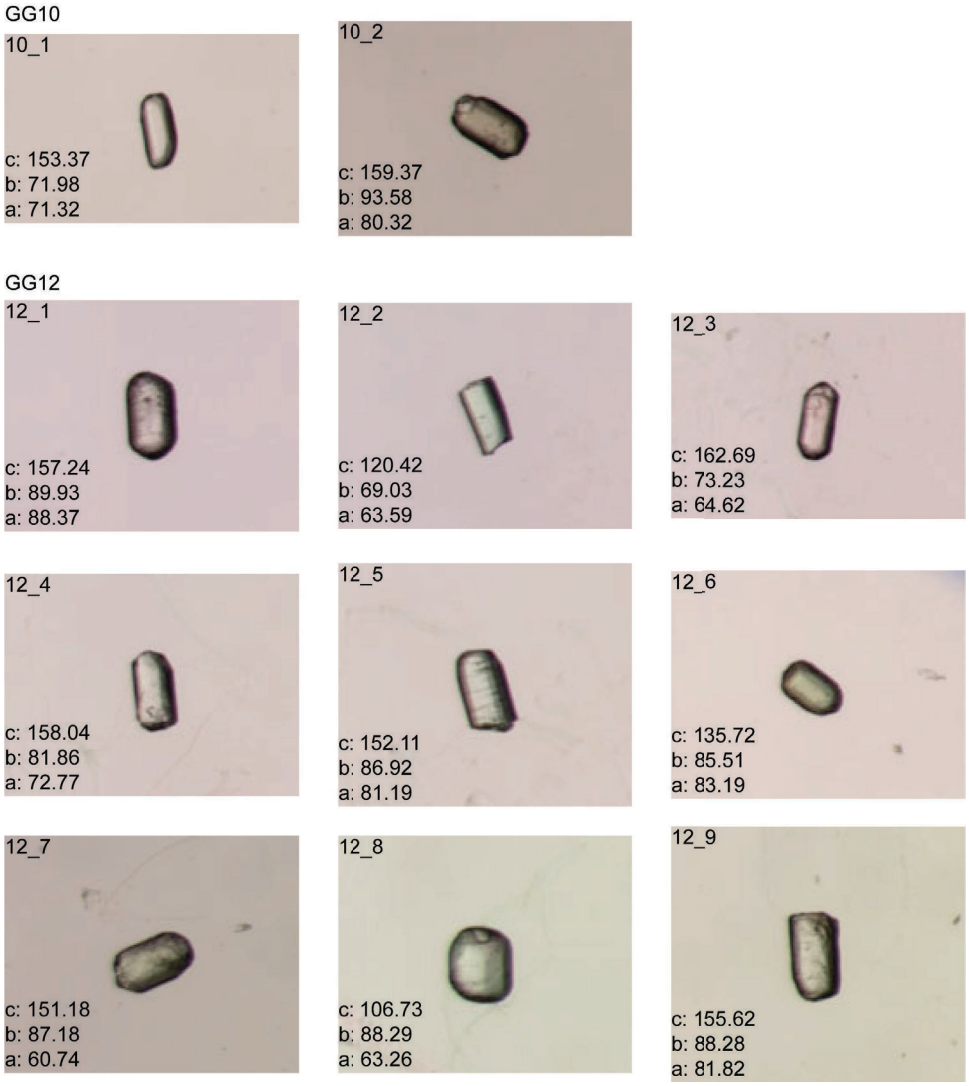

Figure B.9: Apatite crystals selected from specimens GG010 and GG12 for U-Th/He analysis. All measurements in micrometers.

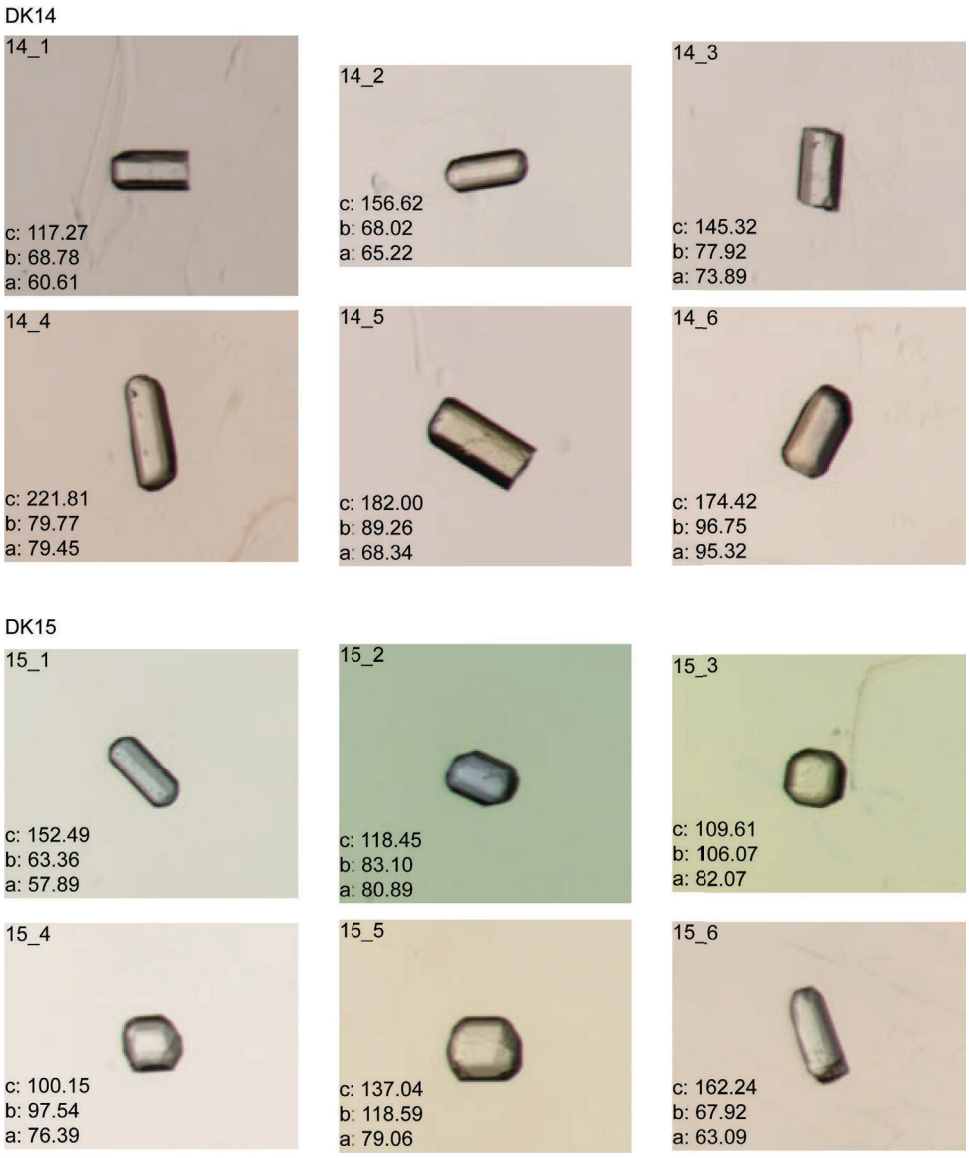

Figure B.10: Apatite crystals selected from specimen DK14 and DK15 for U-Th/He analysis. All measurements in micrometers.

Appendix C

Table C.1: $^{40}Ar/^{39}Ar$ Isotopic data I

Sample no		J	± (1σ)	* Corrected for blank, mass discrimination, and radioactive decay
16UM01A	*Muscovite*	1.86E-03	1.48E-06	Sensitivity 6.312E-17 ± 1.047E-18 (mol/fAmp)

	Relative Isotopic abundances (fAmps)*																			
Power (%)	Ar40	± (1σ)	Ar39	± (1σ)	Ar38	± (1σ)	Ar37	± (1σ)	Ar36	± (1σ)	Ca/K	± (1σ)	Cl/K	± (1σ)	$^{40}Ar^*/^{39}Ar_{(K}$	± (1σ)	$^{40}Ar^*$ (%)	Age (Ma)	± (1σ)
0.20	24.43	0.07	-0.01	0.06	0.02	0.03	-0.03	0.03	0.08	0.00	121.86	889.29	-1.39	13.69	18.61	146.21	-	-	-
0.40	33.65	0.07	0.27	0.06	0.03	0.03	0.03	0.03	0.11	0.00	4.89	4.47	0.06	0.33	5.18	2.25	4.20	17.29	7.46
0.60	22.12	0.06	1.14	0.06	0.07	0.03	-0.04	0.03	0.06	0.00	-1.49	1.03	0.11	0.08	4.78	0.47	24.76	15.97	1.57
0.80	117.99	0.08	20.36	0.07	0.20	0.03	-0.02	0.03	0.05	0.00	-0.05	0.06	-0.01	0.00	5.13	0.03	88.65	17.12	0.10
1.00	195.12	0.08	36.45	0.07	0.36	0.03	-0.05	0.02	0.03	0.00	-0.07	0.03	-0.01	0.00	5.12	0.02	95.78	17.09	0.05
1.50	668.04	0.12	126.90	0.07	1.46	0.03	-0.02	0.03	0.06	0.00	-0.01	0.01	0.00	0.00	5.12	0.01	97.40	17.09	0.02
2.00	165.40	0.08	29.86	0.07	0.38	0.03	0.08	0.03	0.05	0.00	0.11	0.04	0.00	0.00	5.06	0.02	91.41	16.88	0.07
2.50	37.68	0.07	2.30	0.06	0.03	0.03	0.01	0.03	0.09	0.00	0.22	0.55	-0.02	0.04	4.93	0.27	30.18	16.46	0.91
4.00	76.94	0.07	11.29	0.06	0.11	0.03	0.05	0.03	0.07	0.00	0.19	0.11	-0.01	0.01	5.06	0.05	74.27	16.88	0.18

		J	± (1σ)
16UM01B	*Muscovite*	1.86E-03	1.44E-06

	Relative Isotopic abundances (fAmps)*																			
Power (%)	Ar40	± (1σ)	Ar39	± (1σ)	Ar38	± (1σ)	Ar37	± (1σ)	Ar36	± (1σ)	Ca/K	± (1σ)	Cl/K	± (1σ)	$^{40}Ar^*/^{39}Ar_{(K}$	± (1σ)	$^{40}Ar^*$ (%)	Age (Ma)	± (1σ)
0.20	75.50	0.07	4.92	0.07	0.09	0.03	0.02	0.03	0.18	0.00	0.15	0.25	0.00	0.02	4.26	0.14	27.79	14.20	0.50
0.50	11.43	0.12	0.71	0.06	0.08	0.03	-0.01	0.03	0.03	0.00	-0.88	1.69	0.26	0.12	2.29	0.62	14.14	7.60	2.10
0.90	81.34	0.07	13.00	0.06	0.11	0.03	0.06	0.03	0.05	0.00	0.22	0.09	-0.01	0.01	5.03	0.04	80.53	16.80	0.10
1.10	144.66	0.07	27.70	0.06	0.32	0.03	-0.03	0.03	0.01	0.00	-0.04	0.05	0.00	0.00	5.06	0.02	97.06	16.90	0.10
1.30	189.93	0.08	36.41	0.06	0.49	0.03	0.00	0.03	0.02	0.00	0.00	0.04	0.00	0.00	5.08	0.01	97.55	17.00	0.10
1.50	166.00	0.08	32.17	0.07	0.41	0.03	0.06	0.03	0.01	0.00	0.09	0.04	0.00	0.00	5.03	0.02	97.67	16.80	0.10
2.00	82.06	0.10	15.82	0.07	0.17	0.03	-0.02	0.03	0.01	0.00	-0.06	0.08	0.00	0.01	5.03	0.03	97.07	16.80	0.10
2.50	56.83	0.07	10.99	0.06	0.11	0.03	0.02	0.03	0.00	0.00	0.09	0.11	-0.01	0.01	5.14	0.04	99.44	17.10	0.10
4.00	36.50	0.07	7.00	0.07	0.15	0.03	0.03	0.03	0.00	0.00	0.22	0.21	0.03	0.01	5.01	0.06	96.28	16.70	0.20

Table C.2: $^{40}Ar/^{39}Ar$ Isotopic data II

Sample no		J	± (1σ)	* Corrected for blank, mass discrimination, and radioactive decay
16UM10	*Muscovite*	1.86E-03	1.27E-06	Sensitivity 6.312E-17 ± 1.047E-18 (mol/fAmp)

	Relative Isotopic abundances (fAmps)*																			
Power (%)	Ar40	± (1σ)	Ar39	± (1σ)	Ar38	± (1σ)	Ar37	± (1σ)	Ar36	± (1σ)	Ca/K	± (1σ)	Cl/K	± (1σ)	$^{40}Ar^*/^{39}Ar_{(K}$	± (1σ)	$^{40}Ar^*$ (%)	Age (Ma)	± (1σ)
0.20	2.00	0.06	0.09	0.07	-0.03	0.03	-0.03	0.03	0.00	0.00	-15.71	18.82	-0.90	1.23	6.47	5.86	28.48	21.53	19.38
0.50	19.39	0.07	1.88	0.06	0.06	0.03	0.05	0.03	0.03	0.00	1.26	0.71	0.04	0.05	4.99	0.27	48.26	16.61	0.89
0.90	86.19	0.08	15.17	0.07	0.18	0.03	0.04	0.03	0.03	0.00	0.12	0.08	0.00	0.01	5.01	0.03	88.35	16.70	0.11
1.10	108.33	0.08	20.35	0.06	0.24	0.03	0.03	0.03	0.02	0.00	0.07	0.06	0.00	0.00	5.02	0.02	94.37	16.71	0.08
1.30	10.15	0.06	1.77	0.06	-0.03	0.03	0.01	0.03	0.00	0.00	0.29	0.68	-0.08	0.05	5.60	0.23	97.85	18.64	0.78
1.50	3.99	0.06	0.81	0.06	-0.10	0.03	-0.01	0.02	0.00	0.00	-0.31	1.42	-0.39	0.12	4.88	0.51	98.64	16.25	1.68
2.00	25.61	0.07	4.99	0.06	0.05	0.03	-0.01	0.03	0.00	0.00	-0.12	0.25	-0.01	0.02	5.05	0.08	98.59	16.82	0.27
2.50	4.24	0.06	0.82	0.06	0.01	0.03	0.02	0.03	0.00	0.00	1.40	1.54	-0.01	0.12	4.68	0.47	90.14	15.58	1.55
4.00	4.57	0.06	0.69	0.07	0.05	0.03	0.00	0.03	0.00	0.00	-0.33	1.83	0.15	0.15	4.55	0.56	68.94	15.17	1.87

		J	± (1σ)
16UM11	*Muscovite*	1.85E-03	1.27E-06

	Relative Isotopic abundances (fAmps)*																			
Power (%)	Ar40	± (1σ)	Ar39	± (1σ)	Ar38	± (1σ)	Ar37	± (1σ)	Ar36	± (1σ)	Ca/K	± (1σ)	Cl/K	± (1σ)	$^{40}Ar^*/^{39}Ar_{(K}$	± (1σ)	$^{40}Ar^*$ (%)	Age (Ma)	± (1σ)
0.20	-0.20	0.07	-0.01	0.06	0.01	0.03	0.05	0.03	0.00	0.00	-276.53	2264.27	-4.15	35.88	-61.07	499.76	-	-	-
0.50	42.73	0.06	0.91	0.07	0.02	0.03	-0.03	0.03	0.13	0.00	-1.35	1.50	-0.04	0.10	4.27	0.72	9.12	14.20	2.40
0.80	93.84	0.07	4.31	0.06	0.08	0.03	0.02	0.03	0.25	0.00	0.18	0.28	-0.01	0.02	4.81	0.20	22.12	16.00	0.70
1.00	93.64	0.07	13.66	0.07	0.21	0.03	-0.10	0.03	0.08	0.00	-0.33	0.10	0.01	0.01	5.04	0.04	73.56	16.80	0.10
1.20	96.00	0.07	17.76	0.07	0.24	0.03	-0.09	0.03	0.02	0.00	-0.24	0.07	0.00	0.01	5.02	0.03	93.00	16.70	0.10
1.40	111.53	0.07	20.86	0.06	0.18	0.03	-0.05	0.03	0.02	0.00	-0.10	0.06	-0.01	0.00	5.05	0.02	94.58	16.80	0.10
2.00	252.88	0.09	44.65	0.07	0.56	0.03	0.01	0.03	0.09	0.00	0.01	0.03	0.00	0.00	5.04	0.02	89.12	16.80	0.10
2.50	46.08	0.06	7.04	0.06	0.05	0.03	-0.02	0.03	0.03	0.00	-0.13	0.18	-0.02	0.01	5.11	0.07	78.14	17.00	0.20
4.00	39.75	0.07	2.84	0.06	0.08	0.03	0.04	0.03	0.09	0.00	0.62	0.47	0.03	0.03	4.16	0.20	29.77	13.90	0.70

Table C.3: $^{40}Ar/^{39}Ar$ Isotopic data III

Sample no			**J**	**± (1σ)**	* Corrected for blank, mass discrimination, and radioactive decay														
16UM12	***Muscovite***		**1.86E-03**	**1.30E-06**	Sensitivity	6.312E-17 ± 1.047E-18 (mol/fAmp)													
	Relative Isotopic abundances (fAmps)*																		
Power (%)	**Ar40**	**± (1σ)**	**Ar39**	**± (1σ)**	**Ar38**	**± (1σ)**	**Ar37**	**± (1σ)**	**Ar36**	**± (1σ)**	**Ca/K**	**± (1σ)**	**Cl/K**	**± (1σ)**	**$^{40}Ar^*/^{39}Ar_{(K}$**	**± (1σ)**	**$^{40}Ar^*$ (%)**	**Age (Ma)**	**± (1σ)**
0.20	0.15	0.06	-0.05	0.06	0.07	0.03	-0.02	0.03	0.00	0.00	22.38	42.16	-4.16	6.17	1.65	5.38	-	-	-
0.50	36.80	0.07	0.82	0.06	0.08	0.03	-0.01	0.03	0.11	0.00	-0.38	1.71	0.17	0.11	3.87	0.78	8.66	12.90	2.60
0.80	151.57	0.08	7.44	0.07	0.21	0.03	-0.06	0.03	0.39	0.00	-0.35	0.17	0.02	0.01	4.95	0.17	24.34	16.50	0.60
1.00	86.56	0.08	14.54	0.06	0.21	0.03	0.02	0.03	0.04	0.00	0.07	0.08	0.01	0.01	5.12	0.04	86.08	17.10	0.10
1.20	115.86	0.08	16.59	0.07	0.16	0.03	0.01	0.03	0.11	0.00	0.04	0.08	-0.01	0.01	5.08	0.04	72.78	16.90	0.10
1.40	189.38	0.08	20.85	0.07	0.31	0.03	0.00	0.03	0.29	0.00	0.01	0.06	0.00	0.00	4.96	0.05	54.72	16.50	0.20
2.00	211.16	0.08	37.55	0.06	0.44	0.03	0.08	0.03	0.07	0.00	0.09	0.03	0.00	0.00	5.10	0.02	90.78	17.00	0.10
2.50	303.65	0.10	54.29	0.07	0.70	0.03	-0.09	0.03	0.10	0.00	-0.07	0.02	0.00	0.00	5.06	0.02	90.57	16.90	0.10
4.00	364.56	0.10	56.83	0.07	0.79	0.03	-0.02	0.03	0.25	0.00	-0.02	0.02	0.00	0.00	5.09	0.02	79.41	17.00	0.10
			J	**± (1σ)**															
16UM13	***Muscovite***		**1.85E-03**	**1.54E-06**															
	Relative Isotopic abundances (fAmps)*																		
Power (%)	**Ar40**	**± (1σ)**	**Ar39**	**± (1σ)**	**Ar38**	**± (1σ)**	**Ar37**	**± (1σ)**	**Ar36**	**± (1σ)**	**Ca/K**	**± (1σ)**	**Cl/K**	**± (1σ)**	**$^{40}Ar^*/^{39}Ar_{(K}$**	**± (1σ)**	**$^{40}Ar^*$ (%)**	**Age (Ma)**	**± (1σ)**
0.20	29.41	0.06	-0.02	0.06	-0.02	0.03	0.00	0.03	0.10	0.00	5.76	75.62	4.48	12.32	70.34	185.93	-	-	-
0.50	43.22	0.06	1.31	0.06	0.05	0.03	0.02	0.03	0.13	0.00	1.10	1.18	0.02	0.06	3.24	0.49	9.86	10.80	1.60
0.80	42.28	0.07	6.75	0.06	0.13	0.03	0.00	0.03	0.04	0.00	0.04	0.23	0.02	0.01	4.62	0.07	73.82	15.30	0.20
1.00	60.07	0.07	12.04	0.07	0.24	0.03	0.06	0.03	0.01	0.00	0.32	0.14	0.02	0.01	4.69	0.04	94.18	15.60	0.10
1.20	83.81	0.08	17.66	0.06	0.21	0.03	0.04	0.03	0.00	0.00	0.13	0.10	0.00	0.01	4.71	0.02	99.46	15.60	0.10
1.40	103.11	0.08	21.41	0.06	0.28	0.03	0.09	0.03	0.00	0.00	0.24	0.07	0.00	0.00	4.75	0.02	98.83	15.80	0.10
2.00	56.49	0.07	11.76	0.06	0.22	0.03	0.00	0.03	0.00	0.00	-0.02	0.14	0.02	0.01	4.73	0.03	98.62	15.70	0.10
2.50	6.30	0.06	1.36	0.06	0.05	0.03	0.04	0.03	0.00	0.00	1.89	1.21	0.07	0.06	4.51	0.26	97.72	15.00	0.90
4.00	19.87	0.07	4.17	0.06	-0.02	0.03	0.05	0.03	0.00	0.00	0.68	0.40	-0.05	0.02	4.76	0.09	99.91	15.80	0.30

Table C.4: $^{40}Ar/^{39}Ar$ Isotopic data IV

Sample no		**J**	**± (1σ)**	* Corrected for blank, mass discrimination, and radioactive decay
16UM14	***Muscovite***	**1.84E-03**	**2.59E-06**	Sensitivity 6.312E-17 ± 1.047E-18 (mol/fAmp)

	Relative Isotopic abundances (fAmps)*																		
Power (%)	**Ar40**	**± (1σ)**	**Ar39**	**± (1σ)**	**Ar38**	**± (1σ)**	**Ar37**	**± (1σ)**	**Ar36**	**± (1σ)**	**Ca/K**	**± (1σ)**	**Cl/K**	**± (1σ)**	**$^{40}Ar^*/^{39}Ar_{(K}$**	**± (1σ)**	**$^{40}Ar^*$ (%)**	**Age (Ma)**	**± (1σ)**
0.20	25.66	0.07	0.17	0.06	0.06	0.03	-0.01	0.03	0.08	0.00	-51.24	224.85	0.64	0.54	1.36	9.49	0.95	4.52	31.50
0.50	27.45	0.07	1.25	0.06	0.05	0.03	0.07	0.03	0.07	0.00	79.91	31.86	0.07	0.08	9.40	1.50	41.66	31.01	4.91
0.80	120.82	0.08	17.45	0.06	0.18	0.03	0.00	0.03	0.06	0.00	-0.17	2.21	-0.01	0.01	5.82	0.10	84.21	19.25	0.32
1.00	222.40	0.09	41.16	0.07	0.42	0.03	0.06	0.03	0.01	0.00	2.01	0.98	-0.01	0.00	5.39	0.04	99.94	17.85	0.14
1.10	255.72	0.09	48.55	0.06	0.51	0.03	-0.05	0.03	0.01	0.00	-1.42	0.79	-0.01	0.00	5.14	0.03	97.93	17.03	0.11
1.20	221.53	0.08	41.45	0.06	0.45	0.03	0.00	0.03	0.01	0.00	0.02	1.03	0.00	0.00	5.23	0.04	98.14	17.32	0.15
1.30	35.00	0.07	6.52	0.06	0.09	0.03	0.00	0.03	0.00	0.00	-0.13	6.06	0.00	0.01	5.37	0.26	100.31	17.80	0.87
1.40	35.72	0.07	6.76	0.06	0.08	0.03	-0.05	0.03	0.00	0.00	-12.04	6.12	0.00	0.01	4.87	0.26	92.73	16.12	0.87
1.50	48.55	0.07	9.14	0.06	0.17	0.03	0.00	0.03	0.00	0.00	-0.64	4.55	0.02	0.01	5.34	0.20	100.73	17.67	0.65
1.60	31.38	0.06	6.22	0.06	0.05	0.03	0.01	0.03	0.00	0.00	1.93	6.82	-0.01	0.01	5.28	0.29	104.94	17.49	0.97
1.70	29.57	0.07	5.72	0.07	0.06	0.03	-0.02	0.03	0.00	0.00	-6.14	7.03	-0.01	0.02	5.00	0.30	97.09	16.54	1.00
1.80	24.92	0.07	4.84	0.07	0.07	0.03	-0.06	0.03	0.00	0.00	-18.49	8.64	0.01	0.02	4.34	0.37	85.18	14.39	1.22
1.90	9.83	0.06	1.82	0.06	0.08	0.03	0.08	0.03	0.00	0.00	68.85	22.43	0.10	0.05	9.03	1.02	163.27	29.79	3.35
2.00	29.16	0.07	5.59	0.06	0.01	0.03	0.02	0.03	0.00	0.00	5.24	7.11	-0.03	0.02	5.59	0.31	107.35	18.52	1.02
2.30	33.84	0.07	6.04	0.06	0.08	0.03	-0.04	0.03	0.00	0.00	-9.00	7.19	0.00	0.01	5.11	0.31	91.63	16.91	1.02
3.00	20.22	0.07	3.54	0.06	0.07	0.03	-0.03	0.03	0.00	0.00	-11.12	11.40	0.02	0.02	5.50	0.49	97.02	18.21	1.63
4.00	24.31	0.06	3.27	0.06	-0.02	0.03	-0.02	0.03	0.00	0.00	-10.59	13.10	-0.05	0.03	7.27	0.58	98.54	24.04	1.91

Table C.5: $^{40}Ar/^{39}Ar$ Isotopic data V

Sample no		J	± (1σ)	* Corrected for blank, mass discrimination, and radioactive decay
16UM15	*Muscovite*	1.85E-03	1.77E-06	Sensitivi 6.312E-17 ± 1.047E-18 (mol/fAmp)

	Relative Isotopic abundances (fAmps)*																			
Power (%)	Ar40	± (1σ)	Ar39	± (1σ)	Ar38	± (1σ)	Ar37	± (1σ)	Ar36	± (1σ)	Ca/K	± (1σ)	Cl/K	± (1σ)	$^{40}Ar^*/^{39}Ar_{(K}$	± (1σ)	$^{40}Ar^*$ (%)	Age (Ma)	± (1σ)
0.20	84.32	0.07	8.88	0.07	0.15	0.03	0.09	0.03	0.14	0.00	0.61	0.17	0.00	0.01	4.95	0.10	52.16	16.40	0.34
0.50	5.84	0.07	1.05	0.07	0.00	0.03	-0.01	0.03	0.00	0.00	-0.80	1.50	-0.05	0.09	4.82	0.37	86.67	15.98	1.22
0.80	37.61	0.07	6.56	0.06	0.01	0.03	0.05	0.03	0.01	0.00	0.46	0.22	-0.03	0.01	5.30	0.07	92.53	17.56	0.22
1.00	67.42	0.07	12.74	0.06	0.16	0.03	0.03	0.03	0.00	0.00	0.12	0.13	0.00	0.01	5.18	0.04	98.08	17.19	0.12
1.20	86.14	0.07	15.36	0.07	0.20	0.03	0.00	0.03	0.02	0.00	-0.01	0.11	0.00	0.01	5.21	0.04	92.98	17.26	0.12
1.40	61.17	0.06	8.10	0.06	0.14	0.03	-0.04	0.03	0.06	0.00	-0.26	0.20	0.01	0.01	5.18	0.09	68.73	17.19	0.28
2.00	49.70	0.07	8.37	0.06	0.08	0.03	-0.08	0.03	0.02	0.00	-0.58	0.18	-0.01	0.01	5.11	0.06	86.16	16.93	0.19
2.50	37.71	0.07	6.15	0.06	0.04	0.03	-0.06	0.03	0.02	0.00	-0.57	0.29	-0.02	0.01	5.20	0.08	84.99	17.25	0.26
4.00	52.23	0.06	7.35	0.07	0.09	0.03	-0.02	0.03	0.05	0.00	-0.17	0.22	-0.01	0.01	5.07	0.08	71.38	16.80	0.27

		J	± (1σ)
16UM17B	*Biotite*	1.85E-03	2.04E-06

	Relative Isotopic abundances (fAmps)*																			
Power (%)	Ar40	± (1σ)	Ar39	± (1σ)	Ar38	± (1σ)	Ar37	± (1σ)	Ar36	± (1σ)	Ca/K	± (1σ)	Cl/K	± (1σ)	$^{39}Ar_{(K}$)	± (1σ)	$^{40}Ar^*$ (%)	Age (Ma)	± (1σ)
0.20	-0.28	0.06	-0.11	0.06	-0.02	0.03	0.01	0.03	0.00	0.00	-4.79	14.66	0.51	0.83	5.00	3.37	198.49	16.60	11.10
0.50	5.65	0.06	0.46	0.06	0.03	0.03	0.02	0.03	0.01	0.00	2.40	3.58	0.13	0.18	3.97	0.80	32.50	13.20	2.60
1.00	112.57	0.07	17.42	0.07	0.22	0.03	-0.01	0.03	0.09	0.00	-0.04	0.09	0.00	0.01	4.85	0.04	75.11	16.10	0.10
1.50	63.34	0.08	12.47	0.06	0.21	0.03	0.00	0.03	0.01	0.00	-0.02	0.13	0.01	0.01	4.88	0.03	96.13	16.20	0.10
2.00	37.82	0.07	7.13	0.07	0.07	0.03	-0.03	0.03	0.01	0.00	-0.24	0.24	-0.01	0.01	4.89	0.06	92.33	16.20	0.20
2.50	47.82	0.07	9.35	0.07	0.12	0.03	-0.04	0.03	0.01	0.00	-0.26	0.17	0.00	0.01	4.83	0.05	94.58	16.00	0.20
3.00	21.52	0.06	4.39	0.06	0.03	0.03	-0.01	0.03	0.00	0.00	-0.07	0.37	-0.02	0.02	4.65	0.08	95.02	15.40	0.30
3.50	2.18	0.06	0.50	0.06	0.02	0.03	0.01	0.03	0.00	0.00	1.14	3.31	0.07	0.17	5.25	0.75	119.92	17.40	2.50
5.00	11.47	0.06	2.37	0.06	0.06	0.03	0.03	0.03	0.00	0.00	0.70	0.72	0.04	0.04	4.68	0.16	96.86	15.50	0.50

Table C.6: Zircon U-Th/He Elemental and Age Data

Sample	Total Atoms Present in Samples						Ages					Elemental data per unit mass of Zircon						
ID			Total		Total		FT Factor		FT Corr						Total		Total	
	4He ncc	+/-	U atoms	+/-	Th atoms	+/-		Age Ma	Age Ma	+/- Ma	Th/U	Mass g	4He ncc/g	+/-	U ppm	+/-	Th ppm	+/-
17B-1	2.13E+01	1.70E-02	4.96E+13	4.53E+11	1.33E+12	1.16E+11	0.77	8.94	11.65	0.72	0.03	5.50E-06	3.87E+06	3.09E+03	3591.86	32.81	93.32	8.11
17B-3	2.06E+01	1.10E-02	5.53E+13	7.82E+11	1.64E+12	1.22E+10	0.81	7.8	9.65	0.63	0.03	6.95E-06	2.97E+06	1.58E+03	3164.88	44.81	90.85	0.68
17B-4	8.30E+00	6.00E-03	2.19E+13	3.37E+11	7.74E+11	2.49E+10	0.73	7.9	10.77	0.64	0.04	3.29E-06	2.52E+06	1.82E+03	2651.62	40.74	90.58	2.92
17B-5	2.05E+01	1.50E-02	5.58E+13	5.56E+11	2.38E+12	4.53E+10	0.79	7.6	9.59	0.61	0.04	6.45E-06	3.18E+06	2.33E+03	3444.89	34.33	141.90	2.71
14-2	1.02E+00	4.00E-03	2.51E+12	4.67E+10	4.85E+11	1.40E+10	0.76	8.1	10.65	0.67	0.19	3.24E-06	3.14E+05	1.23E+03	308.07	5.74	57.72	1.66
14-3	3.43E+00	5.00E-03	8.22E+12	1.05E+11	1.19E+12	1.61E+10	0.82	8.5	10.34	0.68	0.15	7.82E-06	4.39E+05	6.39E+02	418.26	5.37	58.72	0.79
14-4	4.22E+00	5.00E-03	8.00E+12	1.13E+11	5.21E+11	1.06E+10	0.75	10.9	14.54	0.88	0.07	2.59E-06	1.63E+06	1.93E+03	1230.32	17.39	77.47	1.57
14-5	6.58E+00	9.00E-03	1.29E+13	1.15E+11	1.55E+12	1.14E+10	0.80	10.41	13.08	0.84	0.12	6.18E-06	1.06E+06	1.46E+03	829.41	7.38	96.82	0.71
14-6	3.96E+00	5.00E-03	7.22E+12	6.73E+10	7.74E+11	2.60E+10	0.78	11.22	14.33	0.90	0.11	4.08E-06	9.72E+05	1.23E+03	704.17	6.56	73.09	2.46
O1B-1	9.76E-01	4.00E-03	2.20E+12	7.70E+10	4.63E+11	9.19E+09	0.74	8.87	11.92	0.77	0.21	2.58E-06	3.78E+05	1.55E+03	339.03	11.88	69.10	1.37
11_3	1.83E+01	1.00E-02	4.52E+13	1.03E+12	8.40E+11	1.95E+10	0.77	8.43	10.97	0.70	0.02	4.15E-06	4.40E+06	2.41E+03	4336.08	98.61	77.94	1.81

Table C.7: Apatite U-Th/He Elemental and Age Data

Sample	Total Atoms Present in Samples						Ages					Elemental data per unit mass of Apatite						
ID	4He ncc	+/-	Total U atoms	+/-	Total Th atoms	+/-	FT Factor	Age Ma	FT Corr Age Ma	+/- Ma	Th/U	Mass g	4He ncc/g	+/-	Total U ppm	+/-	Total Th ppm	+/-
1A_1	2.85E-01	7.99E-04	1.21E+12	2.69E+10	4.33E+10	8.68E+08	0.80	4.89	6.10	0.10	0.04	8.36E-06	3.41E+04	95.60	57.76	1.28	1.99	0.04
1A_2	5.87E-01	1.79E-03	2.99E+12	6.60E+10	3.72E+11	6.30E+09	0.79	4.00	5.05	0.08	0.12	8.00E-06	7.34E+04	224.30	148.60	3.28	17.93	0.30
1A_3	6.99E-01	1.91E-03	2.45E+12	5.41E+10	1.16E+11	2.12E+09	0.81	5.91	7.32	0.13	0.05	9.85E-06	7.09E+04	194.07	98.99	2.19	4.55	0.08
1A_4	7.29E-01	1.97E-03	2.31E+12	5.11E+10	1.04E+11	1.91E+09	0.84	6.54	7.76	0.14	0.05	1.03E-05	7.11E+04	192.03	89.69	1.98	3.92	0.07
1A_5	2.76E-01	7.91E-04	1.29E+12	2.85E+10	9.26E+10	1.67E+09	0.79	4.41	5.59	0.09	0.07	5.26E-06	5.25E+04	150.42	97.55	2.15	6.78	0.12
1A-6	4.40E-01	1.33E-03	1.88E+12	4.14E+10	6.74E+10	1.24E+09	0.77	4.88	6.33	0.10	0.04	6.22E-06	7.08E+04	214.40	120.04	2.65	4.18	0.08
10-1	6.31E-02	9.80E-04	2.59E+11	5.99E+09	4.12E+10	7.87E+08	0.67	4.93	7.35	0.13	0.16	1.78E-06	3.55E+04	550.38	57.93	1.34	8.91	0.17
10-2	7.91E-02	7.78E-04	2.58E+11	6.48E+09	4.24E+10	2.15E+09	0.71	6.20	8.78	0.16	0.16	2.54E-06	3.12E+04	306.34	40.38	1.02	6.43	0.33
12_1	2.16E-01	7.23E-04	5.36E+11	1.19E+10	4.09E+10	7.90E+08	0.72	8.29	11.48	0.18	0.08	2.83E-06	7.62E+04	255.41	75.37	1.67	5.56	0.11
12_3	1.75E-01	6.76E-04	5.68E+11	1.26E+10	2.88E+10	5.70E+08	0.65	6.38	9.78	0.14	0.05	1.66E-06	1.05E+05	407.30	136.12	3.02	6.67	0.13
12_4	1.33E-01	5.01E-04	3.72E+11	8.23E+09	3.15E+10	6.76E+08	0.68	7.35	10.78	0.16	0.08	2.04E-06	6.51E+04	245.77	72.50	1.61	5.96	0.13
12_5	1.73E-01	1.87E-03	5.61E+11	1.25E+10	3.69E+10	6.94E+08	0.73	6.36	8.73	0.14	0.07	2.37E-06	7.30E+04	788.30	94.19	2.10	6.00	0.11
12-7	1.37E-01	8.91E-04	4.03E+11	9.26E+09	4.47E+10	7.79E+08	0.63	6.95	11.00	0.16	0.11	1.50E-06	9.15E+04	594.14	107.03	2.46	11.47	0.20
12-8	6.40E-02	1.02E-03	2.57E+11	5.95E+09	2.28E+10	5.88E+08	0.63	5.12	8.19	0.14	0.09	1.14E-06	5.61E+04	898.75	89.64	2.08	7.70	0.20
12-9	1.17E-01	9.77E-04	4.48E+11	1.04E+10	2.89E+10	6.13E+08	0.73	5.40	7.38	0.13	0.06	2.48E-06	4.73E+04	394.03	71.98	1.67	4.50	0.10
14_1	9.79E-03	1.62E-04	3.78E+10	9.10E+08	3.98E+10	1.75E+09	0.64	4.37	6.86	0.12	1.05	1.05E-06	9.32E+03	153.94	14.31	0.35	14.60	0.64
14_2	1.26E-02	2.39E-04	4.66E+10	1.05E+09	5.32E+10	1.05E+09	0.64	4.49	7.01	0.12	1.14	1.55E-06	8.14E+03	154.18	11.97	0.27	13.22	0.26
14_3	1.89E-02	1.65E-04	7.57E+10	1.75E+09	1.09E+11	1.94E+09	0.72	3.93	5.46	0.08	1.44	1.86E-06	1.02E+04	88.94	16.20	0.37	22.59	0.40
14_4	2.56E-02	2.03E-04	8.24E+10	1.86E+09	8.48E+10	2.94E+09	0.70	5.26	7.47	0.11	1.03	3.20E-06	8.00E+03	63.47	10.24	0.23	10.21	0.35
14_5	1.48E-02	1.81E-04	6.06E+10	1.40E+09	4.94E+10	9.33E+08	0.69	4.29	6.26	0.10	0.82	2.21E-06	6.67E+03	81.99	10.91	0.25	8.62	0.16
14_6	2.78E-02	1.90E-04	1.24E+11	2.74E+09	1.79E+11	3.15E+09	0.73	3.52	4.80	0.06	1.45	3.64E-06	7.63E+03	52.13	13.55	0.30	18.98	0.33
15-1	4.60E-02	6.15E-04	2.01E+11	4.77E+09	8.23E+10	1.53E+09	0.61	4.37	7.12	0.11	0.41	1.23E-06	3.74E+04	500.39	65.19	1.54	25.76	0.48
15-2	5.17E-02	9.21E-04	2.96E+11	6.84E+09	1.36E+11	2.10E+09	0.68	3.31	4.84	0.09	0.46	1.79E-06	2.89E+04	514.57	65.77	1.52	29.17	0.45
15-3	1.15E-01	1.18E-03	6.87E+11	1.58E+10	4.52E+11	6.99E+09	0.69	3.04	4.44	0.07	0.66	1.92E-06	5.99E+04	614.13	142.50	3.28	90.75	1.40
15-4	3.12E-02	9.17E-04	1.68E+11	3.89E+09	8.39E+10	1.42E+09	0.67	3.48	5.23	0.12	0.50	1.51E-06	2.06E+04	607.07	44.38	1.03	21.39	0.36
15-5	1.09E-01	1.07E-03	8.86E+11	2.05E+10	3.06E+11	4.64E+09	0.69	2.39	3.46	0.05	0.35	2.33E-06	4.68E+04	458.61	151.40	3.51	50.59	0.77